INTERFACING PHOTOSYSTEM I WITH CONDUCTIVE THREE-DIMENSIONAL FRAMEWORKS FOR SOLAR ENERGY CONVERSION

by

Dilek Dervishogullari

Dissertation

Submitted to the Faculty of the

Graduate School of Vanderbilt University

in partial fulfillment of the requirements

for the degree of

DOCTOR of PHILOSOPHY

in

Chemistry

October 31, 2020

Nashville, Tennessee

Approved:

Lauren E. Buchanan, Ph.D.

John A. McLean, Ph.D.

G. Kane Jennings, Ph.D.

David E. Cliffel, Ph.D.

For my family…

ACKNOWLEDGEMENTS

First, I would like to acknowledge the organizations that funded my graduate school research: The National Science Foundation (NSF: DMR-1507505) and the United States Department of Agriculture (2013-67021-21029). Financial support for travelling to academic conferences was provided through the Graduate Student Travel Grant. I would also like to extend special thanks to the Vanderbilt Institute of Nanoscale Science and Engineering as well as the Rosenthal and McDonald Labs at Vanderbilt University Chemistry Department for use of their facilities and instrumentation.

Second, I would like to acknowledge my research advisor Prof. David Cliffel for not only accepting me into his research group, but also for molding me into a competent scientist and an independent researcher. His guidance, patience and understanding have made my graduate school life infinitely better. I would also like to thank Prof. Kane Jennings for his valuable insight and mentorship. His mentorship has been a valuable resource when I felt lost with my research. Additionally, I would like to extend my acknowledgement to the rest of my PhD committee, Prof. John McLean and Prof. Lauren Buchanan. Their diverse ideas have shaped my research into what it is today and encouraged me to think out of the box. I am forever grateful for their encouragement and support.

Third, I would like to acknowledge all of my coworkers in the Cliffel Lab as well as the rest of my Vanderbilt family. My graduate student mentor Dr. Evan Gizzie introduced me to graduate research and served as my role model for the first few years of my graduate career. I would like to thank the people I have worked with closely. Thank you to Chris Stachurski, Kody Wolfe, Joshua Passantino and John Williams for the

insightful discussions and overall daily support. They collectively taught me how important teamwork is for success to materialize. I would like to thank my two undergraduate mentees, Alexandra Quinones Melendez and Jade Stanley. Serving as their mentor was a great pleasure and helped me become a better teacher. Finally, I would like to thank the rest of the Cliffel Lab for providing an embracing work environment and making me feel at home. Specifically, I would like to acknowledge my two best friends, Sara Melow and Ethan Mcclain. Thank you for putting a smile on my face every day. Graduate school would not be the same without you.

Last but not least, I would like to acknowledge my wonderful friends and family. My friends from all over the world have shaped me into the person that I am today and kept me grounded. I am grateful for having crossed paths with you. Most importantly, I would like to thank my incredible family to whom I dedicate this thesis: To my parents Sirin and Kamil, thank you for raising me to believe that I can achieve anything with hard work and dedication and making all of this possible. You are my biggest cheerleaders. To my brother Mehmet, thank you for being my biggest inspiration and role model. I hope I have made you proud. To my sister-in law Marina, thank you for being the sister I never had. Life would not be the same without you. Finally, to my husband and my teammate in life Kirill, thank you for supporting me in every step of the way and being on this journey with me. I appreciate your presence in my life more and more every day.

TABLE OF CONTENTS

LIST OF FIGURES

LIST OF TABLES

Chapter I

INTRODUCTION: PHOTOSYSTEM I (PSI) FOR SOLAR ENERGY CONVERSION

Utilizing the energy of the sun is not new or unique. As early as 7th century B.C., humans were concentrating the sun's light (and heat) with reflective surfaces to start fires.[1] The first proper solar cell (an electrical device that converts the energy of light directly into electricity) was developed in 1883 by an American inventor named Charles Fritts.[2] His material of choice was a semiconductor called selenium.[2] Fast forward to the 1950s, when the National Aeronautics and Space Administration (NASA) collaborated with Bell Laboratories to find a reliable energy generation method which could survive the harsh vacuum of space. Researchers at Bell Laboratories tested out different semiconductor materials and discovered that using silicon instead of selenium increased the efficiency of their cells to 6%.[3] The New York Times hailed the discovery for creating a practical way to tap into the "limitless energy of the sun". The silicon solar cell technology was then adopted by the space program.[3] By 1972, nearly every U.S. satellite was running on solar power, leading to increased efforts to reduce the cost of silicon-based solar cell production.[3] These efforts went into overdrive after the oil price crises of 1973 and 1979, when the price of oil skyrocketed from $3 a barrel to $40 a barrel.[4] To alleviate the rising economic and social impacts of using foreign oil, the development of renewable energy sources like solar and wind became a major national priority. While this urgency waned in the 1980s and 1990s, solar energy technology continued to advance alongside the microchip manufacturing industry, which also uses silicon. Then, at the beginning of the 21st century, the world finally decided to get serious about solar energy.

Although humankind has only recently become serious about serious about solar energy, a fundamental energy conversion process derived from sunlight has been making life on Earth possible for billions of years. Photosynthesis is the process by which light energy, in the form of photons, is converted into chemical energy to be used by photosynthesizing organisms to sustain their life.[5] Photosynthesis allows plants, algae and cyanobacteria to flourish on the sun's energy via carbon fixation and drives the carbon cycle between the earth, the oceans and living organisms.[6,7] Photosynthesis is also the only source of oxygen in the Earth's atmosphere.[7] The fossil fuels that we still rely on as a primary fuel source for our species are also derived from the chemical energy generated through photosynthesis. Considering the importance of photosynthesis to the continuation of life on Earth, scientific research into the fundamental understanding of photosynthesis should be a priority. Researchers around the world have been examining ways to adapt the energy harvesting secrets of photosynthetic organisms to man-made systems, to provide more efficient ways to capture and utilize solar energy. Light-harvesting protein-pigment complexes, which play a crucial role in photosynthesis, have the potential to be incorporated into these man-made systems as part of biohybrid electrodes. Biohybrid simply means combining organic (biological) materials with inorganic materials.[8,9,10] Electrodes are simply conductive substrates which allow current flow through them.

Biohybrid electrodes utilize light-to-charge converting protein-pigment complexes involved in oxygenic photosynthesis, in order to convert the sun's energy into other forms.[10] These complexes, which can be extracted from plants, algae and cyanobacteria, are interfaced with conductive substrates (electrodes) such as metals, semimetals or semiconductors, in an effort to achieve efficient electron transfer between the complex and

the electrode.[11,12] These electrodes have a wide range of applications, ranging from photo-switchable biosensors, to solar to chemical, and solar to electrical energy conversion systems.[10,13] One of the most promising light converting complexes is Photosystem I (PSI). Amongst others, the PSI complex (or PSI protein complex as it will sometimes be referred to in this work) stands out with its robustness and ability to accept electrons from a wide range of materials. These materials include native electron donors (cytochrome c and plastocyanin), organic and inorganic redox compounds, different types of electrodes, and conductive polymers.[14] Certain strains of PSI have been shown to have a thermal tolerance of up to 70 ^{o}C.[15] PSI's unusual thermal stability outside of its native environment plays a key role in its integration into solar cells, which may be subjected to high temperatures under illumination for an extended period of time. *In vivo,* the PSI protein complex is a photodiode that facilitates the photoexcitation and transport of an electron necessary for the reduction of $NADP^{+}$. It achieves a net 1.1 V charge separation with a near-unity quantum efficiency and has one of the lowest reduction potentials found in nsture.[16,17] In addition to its excellent optoelectronic properties and low-cost, utilizing PSI offers other advantages such abundance in nature, non-toxicity and ease of extraction. [17,18] For these reasons, PSI-based photoelectrochemical cells and photovoltaics have been widely researched in recent decades as sustainable solar energy conversion alternatives to traditional systems.[18,19]

As depicted in Figure 1.1, PSI is found embedded within the thylakoid membrane, which separates the thylakoid lumen from the chloroplast stroma.[20] The thylakoids themselves are located in the chloroplast, which is an organelle inside the plant cell and is generally known as the powerhouse of the cell.[21] Apart from protein subunits, lipids and

coenzymes, PSI complex also contains pigments known as chlorophylls.[21] The absorption of a photon by the peripheral antenna chlorophylls results in an electron-hole pair formation at the P_{700} reaction center located near the lumenal side of the thylakoid membrane.[22] This electron is spatially and energetically transported through a series of phylloquinone mediators until it reaches the terminal iron-sulfur cluster, F_B, located on the stromal side of the protein. [22,23] *In vivo*, the water-soluble metalloprotein plastocyanin donates an electron to the oxidized reaction center P_{700}^{+}. Similarly, the water-soluble metalloprotein ferredoxin accepts an electron from the reduced iron-sulfur cluster F_B^{-}.[22,23] This process subsequently drives the production of adenosine 5'-triphosphate (ATP) and reduced nicotinamide adenine dinucleotide phosphate (NADPH) in normal plant metabolism as the electron mediator.[19-24] While PSI has a really high internal quantum efficiency, in order to fully benefit from this in artificial solar energy conversions systems, unique electron donor/acceptor materials must be developed and implemented.

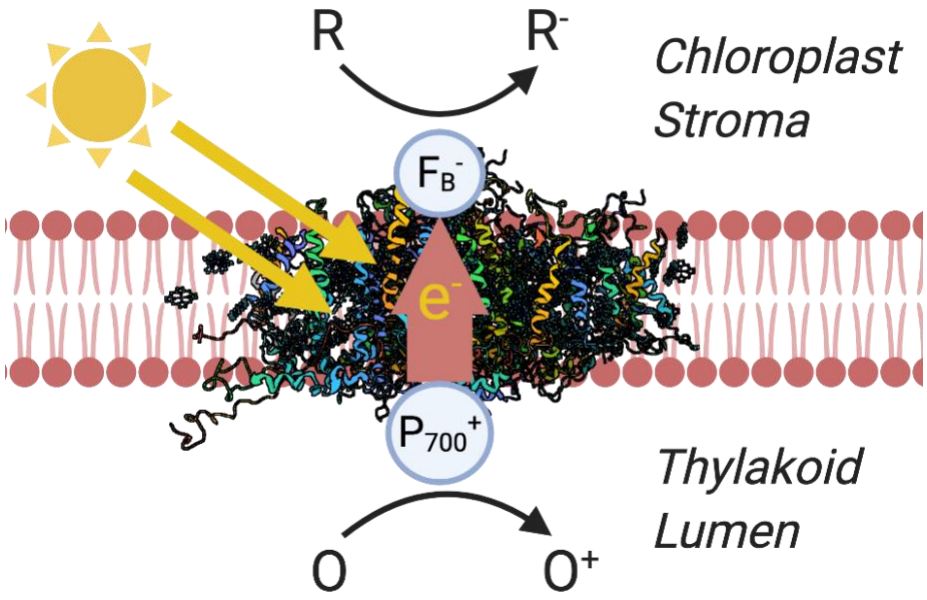

Figure 1.1. PSI protein complex structure embedded in the thylakoid membrane. The F_B side is exposed to the chloroplast stroma and the P_{700} side is exposed to the thylakoid lumen. The protein complex structure is modified from Amunts et al.[16,25] (Created with BioRender.com).

As part of novel biohybrid systems, PSI has previously been interfaced with a wide range of materials including diffusible small molecules, metals, semimetals, semiconductors, electron/hole conducting polymers, and conductive carbon nanomaterials[16,26,27,28] Earlier work coupled monolayers of PSI on functionalized gold substrates through solution-phase self-assembly processes.[29] Subsequent work achieved higher photocurrent performance by drop casting thick multilayer PSI films on gold, silicon and graphene electrodes.[19,27,30] Applying thicker films of PSI increases overall light absorption in the red (680 nm) and blue (430 nm) regions and provides a higher areal loading of the protein complex (Figure 1.2).[12,31] Although these multilayer films resulted

in photocurrent densities significantly larger than those obtained from monolayer assemblies, their performances were limited by poor charge transfer and lack of orientation specificity within the film. Three-dimensional conductive frameworks offer another avenue for increasing areal protein loading while also improving charge transfer.

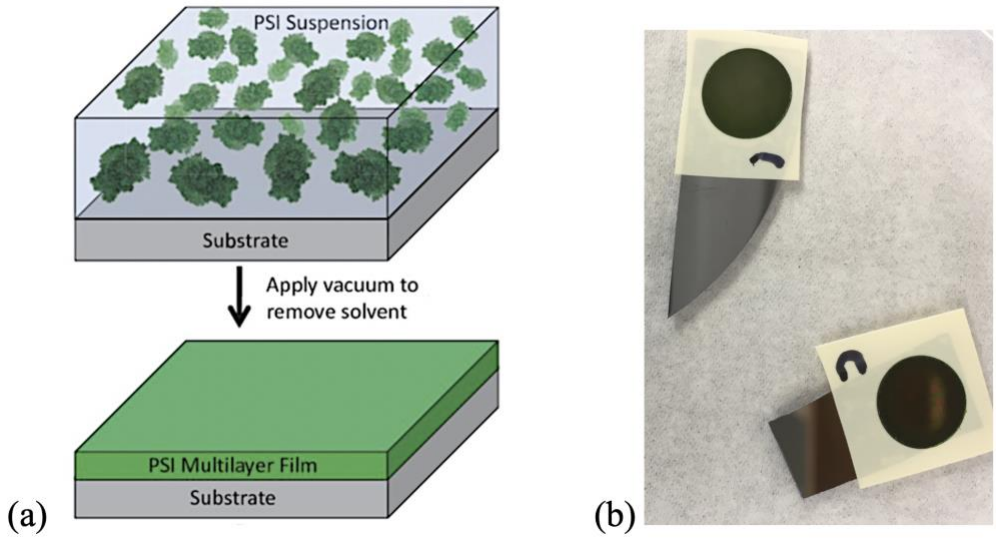

Figure 1.2. (a) Vacuum deposition of PSI multilayer film on a substrate (b) Photo of deposited PSI multilayer films on p-doped silicon substrate (Figure 1.2.a is reprinted with permission from Ciesielski et al.)[32]

In 2008, Ciesielski et al. modified nanoporous gold leaf electrodes with PSI monolayers and achieved a 300% increase in photocurrent.[29] The improvement was credited to an increase in the electrochemically active surface area, which allowed for an increase in mediated photocurrent response. Examples of other high surface area PSI bioelectrodes include a gold nanoparticle-based approach, and a nanostructured TiO_2 and ZnO device.[33] In each case, the increase in photocurrent density is primarily attributed to an increase in the active electrode surface area. Increasing this area provides a higher

interfacial area for either protein-electrode interaction or for mediated electron transfer. Recently, methods for producing three-dimensional, transparent, and conductive ITO electrodes have spurred interest in their application to biohybrid photovoltaics. Wenzel et al. showed that photocurrents generated from photosynthetic biofilms composed of either *Nostoc* punctiforme or *Synechocystis* sp. on porous ITO electrodes are two orders of magnitude larger than those on planar ITO.[34] Stieger et al. utilized porous ITO with isolated PSI by wiring T. *elongatus*-derived PSI via cytochrome c (cyt c) to the surface of 460 nm ITO pores, resulting in a 150 $\mu A/cm^2$ photocurrent density with an applied potential of 100 mV vs. Ag/AgCl.[10,35]

Interfacing PSI with conductive polymers is another way of increasing protein loading in a three-dimensional conductive framework while also improving electron-charge transfer between PSI and the electrode or between PSI and the mediator. Though conductive polymers are most commonly found in biosensors, they display similar electrical properties to conventional semiconductors and thus have a wide range of applications in solar energy conversion.[36,37] A study by Hamidi et al. demonstrated that immobilized thylakoid membranes on osmium-polymer-modified electrodes generated photoelectrochemical activity, where the osmium redox polymer acted as an electron acceptor from the thylakoid membranes.[37] In 2015, Gizzie et al. incorporated PSI into a polyaniline conductive framework grown directly on TiO_2 electrodes and interfaced this photoactive electrode with an evaporated metallic cathode in order to yield stand-alone solid-state photovoltaics.[38] Both of these studies demonstrate that the incorporation of PSI into conducting polymer frameworks allows for improved conductivity within the PSI−electrode interface.

The PSI complex serves not only as a model for inspiration but also as a complete entity that can be extracted and integrated directly into alternative energy technologies. When creating PSI-based solar energy conversion systems, researchers are seeking strategies that maximize photocurrent output while minimizing cost and use of resources. In this dissertation, efforts of incorporating the PSI protein complex into conductive three-dimensional frameworks such as conductive polymers and porous metal oxide electrodes will be discussed. Improving the interfacial electron transfer pathways within PSI multilayers serves a crucial role in achieving higher efficiencies in PSI-based solar devices. Porous electrodes allow for a larger interfacial area between electrode, electrolyte and photoactive substances while conductive polymer scaffolds offer a new route toward effective "electrical wiring" of PSI complexes.[39] In addition, all of the strategies described in this work use inexpensive fabrication methods and materials. Chapter II will give detailed descriptions of all the general experimental methods used to carry out the research. These methods are PSI extraction procedure from baby spinach leaves, PSI quantification with Baba's assay, photoelectrochemical analysis of PSI films, cyclic voltammetry, contact profilometry, UV-vis spectroscopy, scanning electron microscopy, and energy dispersive x-ray spectroscopy. Chapter III will describe the utilization of polyviologen polymer as electron transport material and nitrogen-doped carbon quantum dots as hole transport material in PSI-based biophotovoltaic cells. Chapter IV will describe efforts of incorporating PSI into porous ITO cathodes for enhanced areal photocurrent generation. Chapter V will describe the effect of dopant concentration on the conductivity of electropolymerized PEDOT-PSI composite films. Finally, chapter VI will conclude the dissertation by providing a summary and an outlook for the future of PSI research efforts.

Chapter II

EXPERIMENTAL AND ANALYTICAL TECHNIQUES

PSI Extraction from Baby Spinach Leaves:

Photosystem I (PSI) complex can be isolated from baby spinach leaves (young leaves of *Spinacia oleracea*) through hydroxyapatite chromatography, which is a commonly used separation method for proteins and DNAs.[22,40] The adsorption of proteins to hydroxyapatite column involves both anionic and cationic exchange. The Ca^{2+} functional groups interact with carboxylic acid residues at the protein surface, while the PO_4^{2+} interact with basic protein residues. Proteins are eluted from the column by switching to a higher phosphate concentration in the buffer, which in turn decreases the electrostatic attraction of positively charged species to the column.[40]

The procedure described in this section has been adapted from a previously reported method.[22] Figure 2.1 below shows a schematic of the general extraction steps. The solutions required for the extraction should be prepared in advance and chilled inside a refrigerator. For reference, the high-velocity centrifuge used in this procedure is Beckman Coulter Allegra X-30R. This procedure requires 100-150 g of raw baby spinach leaves and the expected yield of PSI extract is 50-100 ml (~3 mg/ml PSI).

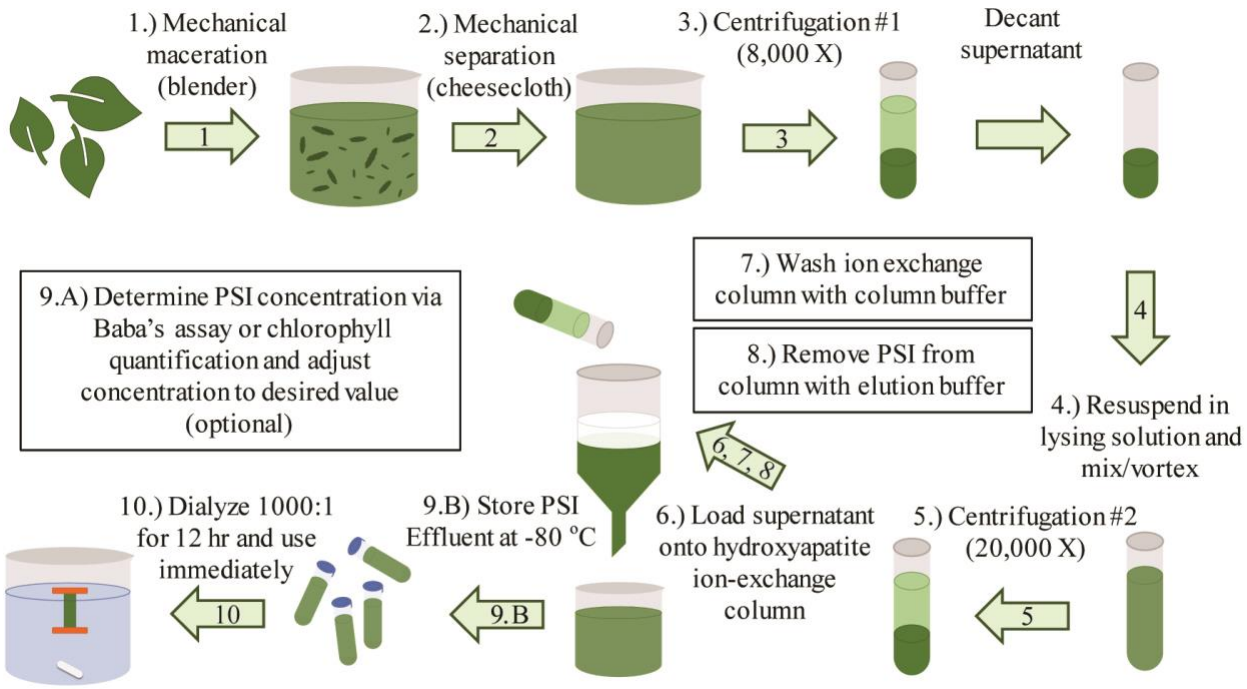

Figure 2.1. Schematic of the PSI protein complex extraction procedure from baby spinach leaves (Figure credit: Kody D. Wolfe)

Required Extraction Solutions:

The solutions whose recipes are given below need to be prepared in advance and chilled. The grinding medium can be placed in the freezer a couple of hours before the extraction and mixed well once it starts forming ice, in order to make it into a slushy consistency.

Grinding Medium (300 mL)

- Sorbitol 18.040 g
- Na-Pyrophosphate 1.340 g
- $MgCl_2 \cdot 6H_2O$ 0.240 g
- (L) Ascorbic Acid 0.110 g

*Adjust pH to 6.5 with HCl

Lysing Solution (100 mL)

- HEPES 1.192 g
- Sorbitol 6.012 g
- EDTA 0.058 g
- $MgCl_2 \cdot 6H_2O$ 0.020 g
- $MnCl_2 \cdot 4H_2O$ 0.020 g
- Triton X-100 1.000 g
  1.00% (w/v)

Column Buffer (1 L)

- Na_2HPO_4 anhydrous 0.855 g
- $NaH_2PO_4 \cdot H_20$ 0.549 g

*Adjust pH to 7.0

Elution Buffer (1 L)

- Na_2HPO_4 anhydrous 0.096 g
- $NaH_2PO_4 \cdot H_20$ 10.980 g
- Triton X-100 0.500 g
  0.05% (w/v)

*Adjust pH to 6.5 with HCl

Extraction Steps:

Mechanical Breakdown.

Organic baby spinach leaves (Dole brand) (100-150 g) must first be deveined and weighed; the stems and large veins are removed using a knife and discarded. The rest are loaded into a high-power blender along with 200 mL of the grinding medium (which needs to have the consistency of slush). The mixture is blended until the contents appear homogenous (no large pieces of baby spinach remain).

Filtration.

Fibrous leaf material must now be removed via filtration using a cheesecloth filter. Before this step, Beckman Coulter Allegra X-30R centrifuge is turned on, the temperature setting is adjusted to 4 °C, and the F-0850 rotor is loaded. Two layers of cheesecloth are placed inside a funnel and the funnel is positioned so that it empties into a 300 mL beaker. The contents of the blender are poured into the cheesecloth slowly (in order to prevent overflowing). After the first pass of the solution, the two-layer cheesecloth is discarded, and eight layers of fresh cheesecloth

are placed inside the funnel. The solution is then poured through the cheesecloth into a new 300 mL beaker.

Separation of Thylakoids.

After mechanical breakdown and filtration, the thylakoids can be separated by high-power centrifugation using Beckman Coulter Allegra X-30R. The thylakoids and thylakoid stacks are heavier than other organelles and plant cell debris in the filtered solution. This leads to the formation of a pellet when the solution is centrifuged at the appropriate angular velocity. **After this centrifugation, the pellet will be kept, and the supernatant will be discarded.** As mentioned before, the centrifuge needs to be prepared with the correct rotor (F-0850) and cooled down to 4 °C. The centrifuge settings need to be adjusted to RCF = 8,000 and time = 1 min. The centrifuge tubes (and caps) which are sized to fit the F-0850 rotor are located and placed in tube rack. The filtered solution is divided into each of the eight tubes. They should all be filled approximately halfway. Then the tubes are balanced by eyesight, using a glass or plastic pipet. After weighing of the tubes and the caps (along with the contents), **the maximum difference between any two is ensured to be less than 1 mg.** Once the tubes are balanced, they are placed in the F-0850 rotor. After the tubes are properly loaded, the rotor cap is tightened, and the centrifuge lid is closed. Once the start button is pressed, the centrifuge will start to make a loud noise (this is normal). **After the centrifugation is complete, the samples are removed, and the supernatant is discarded.** The pellets can be left in the tubes for the next step.

Lysing the Thylakoid Membrane.

A surfactant containing solution will now be used to lyse the thylakoid membranes. The surfactant acts by reacting with the hydrophobic regions of the lipid bilayer, solubilizing the lipids, and releasing the membrane bound proteins. The surfactant also solubilizes proteins by binding to

their hydrophobic equatorial regions, which are typically embedded within the thylakoid membrane.[41,42] In order for PSI to remain suspended in solution, it needs to be solubilized by some amount of Triton X-100. The centrifuge rotor needs to be changed to the F-0630 in preparation for the next step. The centrifuge settings are then adjusted to rotor = 0630, RCF = 20,000, and time = 15 min. With a pipet, 2-3 mL of lysing solution are loaded into each of the eight centrifuge tubes containing pellets. Each tube is vortexed for ~20 s and the contents are emptied into the new set of centrifuge tubes (the ones that fit into the F-0630 rotor). The F-0630 rotor can only hold six tubes, so the solution from the previous eight must be equally distributed among the six for the next step.

Cell Material Removal and Preparation of the Separation Column.

Using as little lysing solution as possible to dissolve the pellets (3-6 mL per tube) ensures the highest concentration of PSI in the end. The tubes are first balanced by eyesight and then weighed on a balance to confirm that **the largest discrepancy in mass is less than 1 mg between any two tubes.** The tubes are then loaded onto the centrifuge.

While waiting for the centrifuge to be completed, the separation column can be set up. For this, a water circulator pump with the outlet connected to a hose is placed in a large container (>20 liters) and the container is filled with ice. The void space in the container is filled with cold tap water. A jacketed extraction column is secured upright using clamps. The outlet of the pump is attached to the lower inlet of the column jacket and another piece of tubing is attached to the upper jacket opening. This tubing connected to the upper jacket opening returns the water to the container, aiding in the circulation of tap water through the jacket. Fifteen grams of hydroxyapatite powder ($Ca_5(OH)(PO_4)_3$, fast flow) is weighed and placed in a 300 mL beaker. Enough column buffer is added to this beaker to cover the hydroxyapatite with an excess of a few cm of liquid

above. The mixture is stirred with a glass stirring rod and allowed to settle for 30-60 s. Then, the column buffer is carefully decanted without losing much of the hydroxyapatite. This procedure is repeated once to ensure removal of very small hydroxyapatite particles that may slow down flow through the column and to allow the hydroxyapatite to become properly charged. The beaker is filled with column buffer again and the mixture is stirred and quickly poured into the column with the valve in closed/off position. After the hydroxyapatite completely settles (the liquid on top of the column looks clear/not cloudy), the valve is opened. The excess column buffer is allowed to drain through the column into a waste beaker, **until the meniscus is exactly level with the top of layer of the packed hydroxyapatite column. At any point during the column extraction, it is crucial to not let the column run dry or let the liquid level fall below the top layer of the hydroxyapatite.** The valve is now turned off, the column buffer waste is discarded, and the circulation pump is turned on to cool the column. As the ice in the container melts, excess water can be drained, and more ice can be added to the container to ensure that the column stays cold. After the centrifugation is done, the tubes are collected, and the supernatant is decanted into an Erlenmeyer flask (pellets can be discarded). Beckman Coulter Allegra X-30R centrifuge can now be turned off and all the plasticware and glassware can be set aside for clean up later.

Loading the Extraction Column. The loading of the packed hydroxyapatite column with PSI is achieved by collecting the positively charged, solubilized PSI complexes via hydrostatic interactions with the negatively charged hydroxyapatite particles.[43] The net positive charge of PSI is due to the collective charge of surface amino acid residues (majority are primary amines which are found in lysine residues) and carboxylic acids.[43] The main assumption is that any sufficiently positively charged species (including PSI) will adhere to the hydroxyapatite electrostatically.

Using a pipet, the supernatant from the Erlenmeyer flask is loaded into the packed column. The solution can be applied to the inner glass wall of the jacket, 1-3 cm above the hydroxyapatite top layer, and allowed to run down the wall **in order to avoid disrupting the top layer.** All of the solution is loaded while the column valve is kept in the off position. The valve is then turned on, and the solution is allowed to flow through the column (while catching the waste in a beaker) until **the meniscus is level with the top of the hydroxyapatite.** The column is now fully loaded with PSI.

Washing the Extraction Column with the Column Buffer.

Washing the extraction column with a low ionic concentration buffer (the column buffer) will remove any negatively charged species. While washing the column, **a green effluent will be collected and discarded (this is not PSI).** With the valve in the off position, the column buffer is loaded onto the column without disturbing the column bed. After the buffer is filled several centimeters above the hydroxyapatite layer, the valve can be turned on and the effluent can be caught in a waste beaker. The column buffer is continuously added to keep the level several centimeters above the hydroxyapatite, until the effluent is completely clear. The washing process may take 1-2 hours. After the effluent becomes clear, the remaining column buffer is allowed to pass through the column until the meniscus is level with the top of the hydroxyapatite, then the valve is turned off.

Collecting PSI with Elution Buffer.

By changing the buffer to a high ionic concentration, the electrostatic attraction of positively charged species to the column will be decreased due to ion shielding. Additionally, the presence of Triton X-100 surfactant in the elution buffer solubilizes PSI complexes adsorbed onto the hydroxyapatite. The elution buffer is loaded onto the column in a similar manner to before.

After an excess of buffer is loaded, the valve is turned on. A waste collection beaker is kept under the column until the effluent gradually goes from colorless to a darker green. **Once the effluent is sufficiently dark green, the collection beaker is switched to a new and clean one. The darker green PSI effluent is collected in the new beaker, until the color begins to change back toward clear. Stopping before the effluent becomes colorless ensures a higher concentration of the end product.** After a sufficient volume of darker PSI effluent is collected (typically 50-100 mL), the valve can be turned off. This is the end of the extraction and an unknown concentration of PSI has been isolated and is ready to be stored at -80 °C. A pipet is used to transfer aliquots of PSI solution into small vials (typically 2 mL). The capped vials are placed into a storage container and labeled with the date of extraction for future reference. **The box is placed in a -80 °C freezer and stored until needed.**

Preparing PSI Mono- and Multilayers and PSI Dialysis Against DI Water.

Stored aliquots of PSI extract can be thawed and used immediately. However, because the PSI solution contains a high concentration of Triton X-100, this solution cannot be used to prepare PSI multilayers. Non-dialyzed PSI solution containing high concentrations of free surfactant, has been shown to enable the preparation of PSI monolayers on some electrode materials.[44,45] Briefly, to prepare PSI monolayers, a cleaned electrode (gold, silicon etc.) is soaked in the non-dialyzed PSI solution. An alternative method is to use vacuum assisted deposition to dry non-dialyzed PSI solution onto an electrode.[45] After the soaking or vacuum deposition, the electrode is rinsed excessively with deionized water to remove unbound PSI. The electrode is then left to dry completely. After rinsing and drying, the electrode surface is left with a monolayer of PSI which is not visible by naked eye but can be observed under a microscope. Alternatively, to prepare PSI multilayers, the PSI solution need to be dialyzed against deionized water to remove excess

surfactant and salt.[32] The dilution ratio of the dialysis is at least 1000:1(water to PSI extract) and the dialysis should be given a minimum of 12 hours to complete.[16]

Desired amounts of PSI aliquots (usually 2-4 mL) are removed from the freezer and allowed to thaw. A large bucket is filled with 4000 mL of deionized water (4000 mL is needed to dialyze 4 mL of PSI). A large magnetic stir bar is placed in the bucket and the bucket is positioned securely on a magnetic stir plate. A 5-8 cm (lengthwise) portion of regenerated cellulose dialysis tubing (Spectrum Labs, 8 kDa molecular weight cut-off, 15 mm inner diameter) is cut using scissors. One end of the tubing is clamped shut using a specialized dialysis clamp or a binder clip. The opposite end is held open with one hand and the aliquot of thawed PSI solution is pipetted into it using the other hand. Once all of the PSI solution to be dialyzed is loaded into the tubing, the second end of the tubing is clamped shut. A dialysis float is placed on one of the clamps and the tubing is checked for leaks. If there are no leaks, the tubing, clamps and float are placed into the bucket, making sure that they don't sink. The stir bar is stirred on low to medium speed ensuring that the dialysis setup remains floating and spinning in the center of the bucket. The bucket is left alone for dialysis to complete for at least 12 hours. Then, dialyzed PSI solution is removed from the dialysis tubing and poured into a container for storage at 4 °C (refrigerator) until needed in experimentation.

PSI Quantification via Baba's Assay:

This procedure has been adapted from the procedure reported by Baba et al.[22] Baba's assay is based on collecting absorbance spectra from two samples containing PSI of equal concentration. One of the samples is treated with a reducing agent and the other one is treated with an oxidizing agent. The difference in the absorbance of these two samples at a wavelength of 725 nm (the isosbestic point) can be used to determine the concentration of PSI (through determining the

concentration of P_{700} reaction centers). The two main assumptions made with this procedure are that all P_{700} reaction centers are fully reduced and oxidized, and that each PSI complex contains exactly one P_{700} reaction center. The recipes for the Baba's Assay buffer, the reduction solution, and the oxidation solution are given below. **These should be prepared right before the absorbance measurements since they are light sensitive.**[22]

Baba's Assay Solutions.

Baba Assay Buffer (100 mL)

- Tricine (50 mM) 0.896 g
- Sorbitol (0.1 M) 1.822 g
- NaCl (10 mM) 0.059 g
- Triton (0.05 % w/v) 0.050 g

Oxidation Solution (10 mL)

- Ferricyanide (1 M) 3.293 g

Reduction Solution (1 mL)

- Na Ascorbate (0.5 M) 0.099 g
- Dithiothreitol (5 mM) 0.001 g

Experimental Steps.

The UV-Vis spectrometer is turned on for the lamp to warm up. The wavelength range is set to 750-650 nm. The UV-Vis scans are carried out using the double beam setting, where one of the cuvettes is the reference and the other cuvette is the sample. The reference and sample cuvettes are prepared with 2275 μL of Baba's Assay Buffer and 100 μL of PSI solution from the extraction. The cuvettes are capped and mixed well by inverting. The two cuvettes are placed in the UV-Vis spectrometer and absorbance spectrum is collected and the scan is saved. When using a double beam setup, the machine will collect the data as "sample" cuvette minus "reference" cuvette, so the data for this scan can be interpreted as the baseline scan and can be used to qualitatively determine the background noise of the experiment.[46] Then, 120 μL of deionized water and 5 μL of reduction solution are added to the reference cuvette. Next, 125 μL of the oxidation solution is

added to the sample cuvette. **The cuvettes are capped and inverted to mix well.** The reaction takes 15 minutes to complete. The absorbance spectrum from 750-650 nm is collected and the scan is saved. The reaction scan and the baseline scan are exported as text files and the text files are opened in Microsoft Excel. The baseline is subtracted from the reaction scan and the resulting data is plotted. The peak absorbance in the differential scan is located (should be near 700 nm) and recorded. Now, the absorbance value at 725 nm (isosbestic point) is recorded and the isosbestic point value is subtracted from the peak absorbance value. The difference is recorded. The PSI concentration in the sample cuvette is calculated using the extinction coefficient of P_{700} (64 mM^{-1} cm^{-1}). Equation 2.1 below shows the necessary calculation.[22]

$$C_{PSI,\ sample\ cuvette}(mM) = \frac{[A_{peak} - A_{isobestic}]}{64\ (mM^{-1}\ cm^{-1}) \times L\ (cm)} \qquad \textbf{Eq. 2.1}$$

$C_{PSI,\ sample\ cuvette}$ = PSI Concentration in the Sample Cuvette (mM)

A_{peak} = Peak absorbance from the differential spectrum (unitless)

$A_{isobestic}$ = Isosbestic point absorbance (unitless)

$L\ (cm)$ = Pathlength in the cuvette (cm), typically 1 cm

Finally, the PSI solution concentration is back calculated from the determined concentration in the sample cuvette using Equation 2.2. Additionally, the concentration can be converted to the more common units of mg PSI/mL by using the molecular weight of PSI (500 kDa). [22]

$$C_{PSI}(mM) = \frac{C_{PSI,sample\ cuvette}(mM) \times V_{cuvette}}{V_{PSI\ solution}} \qquad \textbf{Eq. 2.2}$$

C_{PSI} = PSI Concentration in the bulk PSI solution (mM)

$C_{PSI,\ sample\ cuvette}$ = PSI Concentration in the Sample Cuvette (mM)

$V_{cuvette}$ = Total volume of the sample cuvette (μL), typically 2500 μL

$V_{PSI\ solution}$ = Volume of PSI solution added to the cuvette (μL), typically, 100 μL

The obtained concentration value and the corresponding unit should be written on the box that the extracted PSI solution vials are stored in.

Photoelectrochemical Analysis of PSI Films:

This technique is used to evaluate the performance of electrochemically driven solar energy conversion systems. The photoactivity performance of PSI films in electrochemical systems can be measured by photochronoamperometry (PCA). PCA is a variation of chronoamperometry (applying constant potential to the working electrode and measuring the current over time).[47] The variation with PCA comes from illuminating the sample, using either white light or monochromatic light. If the electrochemical set-up being measured has a photoactive component (light induces a heterogeneous redox reaction), then the resulting change in current can be recorded and observed. The most common configuration for PCA experiments is a three-electrode cell where the three electrodes are universally known as the working, counter and reference electrodes (Figure 2.2.a). In this work, PSI-modified electrode is used as the working electrode, Ag/AgCl (Sat'd KCl) as the reference electrode and a platinum mesh as the counter electrode. The second configuration is a two-electrode cell where the working electrode is attached to the cathode of the device and the counter and reference electrode leads are clipped together and attached to the anode

of the device (Figure 2.2.b). This second configuration can be used to measure the short-circuit current produced by a device by setting the potential between the working and reference electrodes to zero.[6] For either configuration, the first step in measuring photocurrent is obtaining the open circuit potential (OCP) of the working electrode in dark conditions. Applying OCP to the working electrode minimizes the net current and allows the researcher to only observe the current coming from the effect of illumination. As a universal standard, the working electrode is connected to the green wire, the reference electrode is connected to the white wire, and the counter electrode is connected to the red wire.

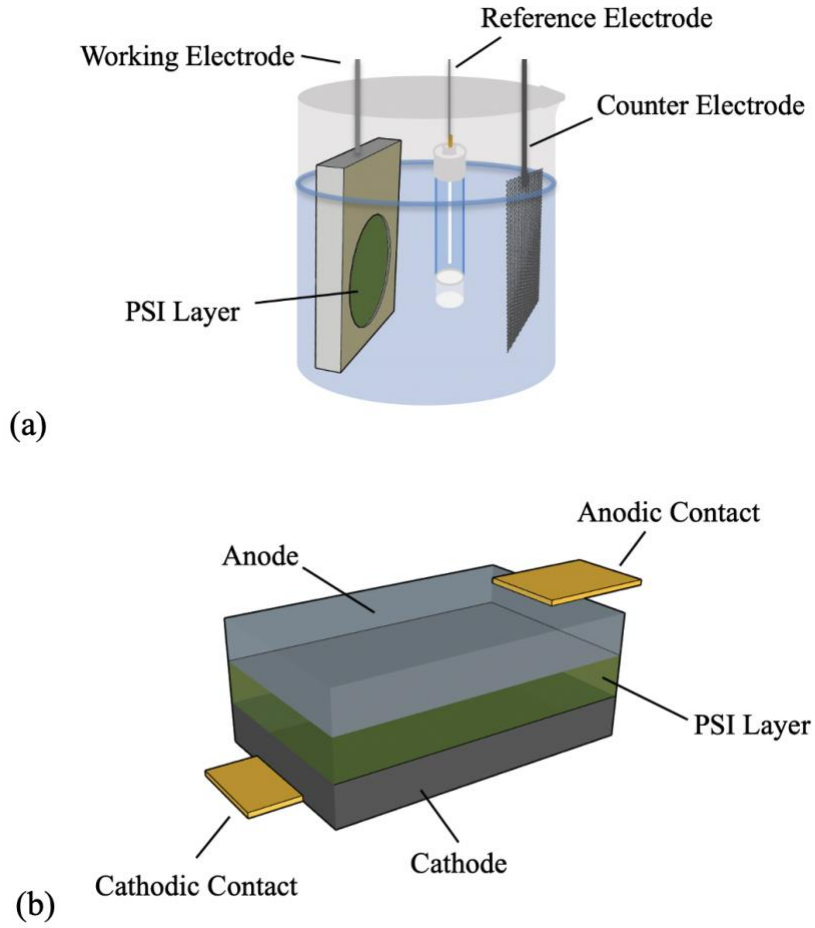

Figure 2.2. (a) Three-electrode electrochemical set-up for Photosystem I characterization (b) Solid-state Photosystem I-based solar cell prototype with two electrode leads (anode and cathode) (Figure credit: Kody. D. Wolfe)

All experiments in this work were performed using a CHI 660a electrochemical workstation with a Faraday cage. Prior to the experiment, the three wires must be ensured to be properly attached to the correct electrodes and the ambient light must be blocked off. For a one electron diffusion-controlled reversible redox couple system, the net current generated on the electrode surface at time t is shown with the following equation:[47]

$$i_{net}(t) = FA\left[k_{red}C_0(0,t) - k_{ox}C_R(0,t)\right] \qquad \textbf{Eq. 2.3}$$

F = Faraday constant

A = Area of the electrode

$C_O(0,t)$ = concentration of the oxidized form of the redox couple at the electrode surface

$C_R(0,t)$ = concentration of the reduced form of the redox couple at the electrode surface

k_{red} = heterogeneous rate constant for the reduction reaction

k_{ox}= heterogeneous rate constant for the oxidation reaction

Cyclic Voltammetry:

Cyclic voltammetry (CV) is a common electrochemical technique used to study novel systems in order to get information about redox system reversibility, electron transfer kinetics, and absorption properties onto electrodes.[47] This is a type of potential sweep method where the potential that is being applied to the working electrode is changed over time while the current is being measured (Potential vs. Current). The term "cyclic" comes from the following: The potential is swept to from the initial potential, E_i, to a final potential, E_f, and then swept back to the initial potential. If the system being analyzed has a redox couple with a formal potential (E_0) between the starting and final potentials, peaks for the corresponding oxidation and reduction reactions will be observed.[6] If E_i is smaller than E_f, the oxidation part of the redox reaction will be measured as anodic current in the forward scan, whereas the reduction part of the redox reaction will be measured as cathodic current in the reverse scan. When the working electrode potential (E_w) approaches the formal potential (E_0), there is an increase of electron transfer rate between the electrode and the redox couple since the energy barrier between them is decreasing. When $E_w > E_0$, the rate will keep increasing until the reaction becomes diffusion-limited, and a peak current

will appear due to the depletion of reactant in the region close to the electrode.[47,48] The typical voltammogram has been illustrated in Figure 2.3.

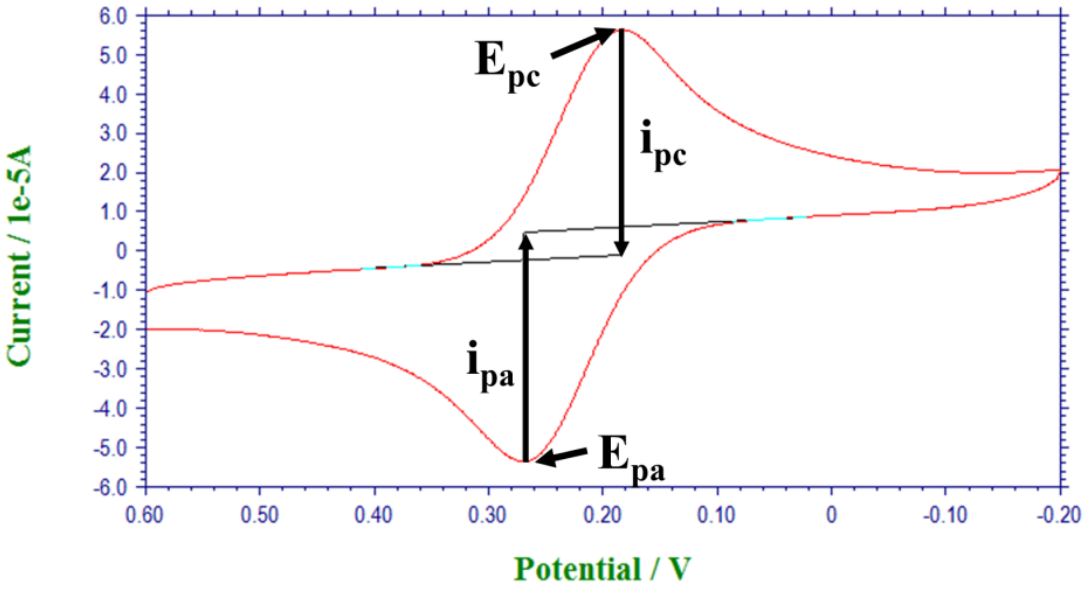

Figure 2.3. Typical cyclic voltammogram where E_{pc} and E_{pa} stand for peak cathodic and anodic potentials and i_{pc} and i_{pa} stand for peak cathodic and anodic currents.

Randles-Sevcik equation shown below correlates the scan rate to the peak current (i_p) and can be used to calculate different variables:[47,48]

$$i_p = \left(2.69\times10^5\right) n^{3/2} A D_0^{1/2} C_0^{*} \nu^{1/2} \qquad \textbf{Eq. 2.4}$$

n = number of electrons transferred (in the redox reaction)

v = scan rate (instrument setting)

D_0 = diffusion coefficient (depends on the analyte)

C^* = redox couple bulk concentration

CV can also be used to determine if a redox system is reversible if the following criteria are met: [47,48]

$$i_p \propto v^{1/2} \quad \textbf{Eq. 2.5}$$

$$\Delta E_p = E_{pa} - E_{pc} = \frac{59}{n}\, mV \ at\ 298K \quad \textbf{Eq. 2.6}$$

$$\left|\frac{i_{pa}}{i_{pc}}\right| = 1 \quad \textbf{Eq. 2.7}$$

E_{pa} = Peak anodic potential

E_{pc} = Peak cathodic potential

I_{pa} = Peak anodic current

I_{pc} = Peak cathodic current

n = number of electrons transferred (in the redox reaction)

v = scan rate (instrument setting)

All of the CV experiments in this work were done using a CHI 660a electrochemical workstation with a Faraday cage. There are several parameters which can be adjusted to achieve different objectives based on the electrochemical system being analyzed. These include initial voltage, scan window, scan polarity (positive or negative), scan rate, number of sweep segments and sensitivity.

Contact Profilometry:

Contact profilometry is a probe technique which provides surface topography information for substrates with features on the order of tens of nanometers to hundreds of microns. This technique utilizes changes in the cantilever deflection in order to identify topographical features

of a sample as the tip at the end of the cantilever is scanned across the sample surface.[49,50] Film thicknesses of Photosystem I films as well as the thicknesses of deposited or electropolymerized polymers on electrode substrates were determined using a Vecco Dektak 150 stylus profilometer. This instrument is located in the facilities of the Vanderbilt Institute of Nanoscale Science and Engineering. Profilometer step height from the top of the film to the underlying substrate surface was used to determine the average thickness of the deposited film.

UV-Vis Spectroscopy:

Photons with wavelengths in the ultraviolet (UV) and visible range, when absorbed, can promote electrons in the molecular or atomic orbitals to reach excited states. Changing the wavelength of the light illuminating a material and measuring the absorbance provides insight about the electronic transitions allowed by the material in question.[51] The following equation defines absorbance:[52]

$$A(\lambda) = -\log_{10}\left(\frac{I(\lambda)}{I_0(\lambda)}\right) \qquad \textbf{Eq. 2.8}$$

$I_0(\lambda)$ = intensity of light before passing through the sample

$I(\lambda)$ = intensity of light after passing through the sample

The Beer-Lambert law relates absorbance to the concentration of the absorbing molecules as well as the optical path length: [52]

$$A = \varepsilon bc \qquad \textbf{Eq. 2.9}$$

ε = molar extinction coefficient

c = concentration of absorbing molecules

b = optical path length

The relationship described by this equation can be used to calculate the concentration of analyte molecules in a solution or deposited film. For example, both PSI extract and PSI films have characteristic absorption peaks in the red (680 nm) and blue (440 nm) parts of the spectrum due to the presence of pigment chlorophyll *a* (Chl *a*) inside them.[12,15] Chlorophylls are light-harvesting pigments found in the mesosomes of cyanobacteria and in the chloroplasts of algae and plants (Figure 2.4).[53]

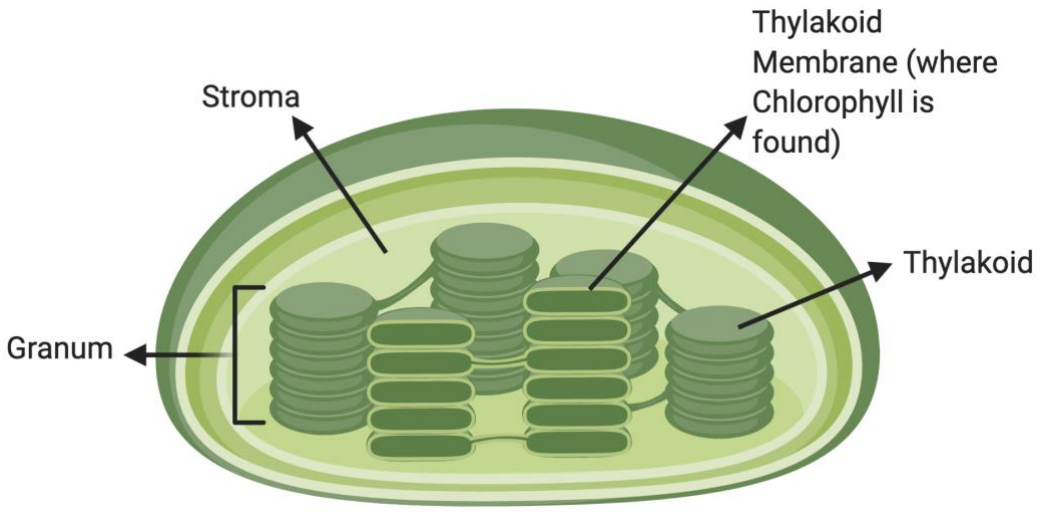

Figure 2.4. Structure of a plant cell chloroplast. Chlorophylls are light-harvesting pigments found in the thylakoid membrane of plants (component of PSI) which are located inside the chloroplast.[53] (Created with BioRender.com)

Scanning Electron Microscopy (SEM) with Energy Dispersive X-Ray Spectroscopy (EDS):

Scanning electron microscopy (SEM) is a technique where a focused beam of electrons is scanned across a surface under vacuum and an image of the surface is obtained by the detection of electrons which are scattered.[54,55] In comparison to optical microscopy, SEM can be used to resolve

much smaller features due to the wavelength of the electron beam being much smaller that of visible light. The wavelength of the electrons is adjusted by the voltage at which the electrons are accelerated, where higher voltages emit electrons of shorter wavelength and vice versa (shorter wavelengths can resolve smaller features).[54]

Primary electrons which are emitted from the source reach the sample surface and get scattered by elastic and/or inelastic collisions with electrons in atomic/molecular orbitals. Electrons which lose minimal energy during the collision escape from the sample and reach the detector.[54] Electrons which lose a large amount of their kinetic energy during collision remain in the sample. Secondary electrons (SE) are scattered electrons with energies smaller than 50 eV and are sourced from within the first few nanometers of the sample surface. These typically result from inelastic collisions. Backscattered electrons (BSE) are scattered electrons with energies larger than 50 eV and are sourced from deeper regions of the sample.[54] These typically result from elastic collisions. BSE images are highly sensitive to differences in atomic number where the material appears brighter in the presence of higher atomic number elements.[54] SE images are useful for the inspection of the topography of the sample surface. The SEM images collected in this work are SE images collected using the In-Lens detector, sourced from Zeiss Merlin SEM with the GEMINI II column, located in the facilities of the Vanderbilt Institute of Nanoscale Science and Engineering. In-Lens detector biases the pole-piece of the electron gun to collect secondary electrons.

Energy dispersive x-ray spectroscopy (EDS) is a microanalysis technique commonly used in conjunction with SEM. It uses a detector to detect x-rays emitted from the sample to obtain the elemental composition of the analyzed volume bombarded with an electron beam. The EDS x-ray detector measures the relative abundance of emitted rays versus their energy.[54]

Chapter III

POLYVIOLOGEN AS ELECTRON TRANSPORT MATERIAL IN PHOTOSYSTEM I-BASED BIOPHOTOVOLTAIC CELLS

Introduction:

Toward the production of scalable photovoltaic devices with long term operational stability, PSI-based solar energy conversion strategies have begun to focus more on the advancement of solid-state photovoltaics and less on liquid photoelectrochemical cells. In 2007, Carmeli et al. pioneered this effort by preparing PSI films on gold electrodes that retained their photoactivity under dry conditions.[56] A different study in 2014 prepared solid-state biohybrid photovoltaic cells by assembling a monolayer of cyanobacterial PSI onto a TiO_2 substrate and backing the device with a polytriarylamine hole transport layer and an air-sensitive MoO_3/Al cathode.[44] Similarly in 2015, Beam et al. used ZnO, which was deposited using a pulsed IR laser, as the electron transport layer between PSI multilayer films and indium tin oxide (ITO).[57] The resulting solid-state device exhibited significant improvement in photocurrent over a traditional PSI-based photoelectrochemical cell. All of these device architectures were limited by their cost and complicated fabrication methods.

There have been several approaches to utilize solid-state polymer electrolytes and electron/hole transfer materials for overcoming problems associated with liquid electrolytes. Redox polymer-modified electrodes (RPMEs) are increasingly used as electron-transfer catalysts in electrochemical applications.[58] Though RPMEs are most commonly found in biosensors, they display similar electrical properties to conventional semiconductors and thus have a wide range of applications in solar energy conversion when used in conjunction with semiconducting

materials.[37,59] A study by Hamidi et al. demonstrated that immobilized thylakoid membranes on osmium-polymer-modified electrodes generated photoelectrochemical activity, where the osmium redox polymer acted as an electron acceptor from the thylakoid membranes.[37] In 2015, Gizzie et al. incorporated PSI into a polyaniline conductive framework grown directly on TiO_2 electrodes and interfaced this photoactive electrode with an evaporated metallic cathode in order to yield stand-alone solid-state photovoltaics.[38] Both of these studies evidence that the incorporation of PSI into conducting polymer frameworks allows for improved conductivity within the PSI-electrode interface. Improving the interfacial electron transfer pathways within PSI multilayers serves a crucial role in achieving higher efficiencies in PSI-based solar devices. Effective electrical wiring of PSI can be achieved through incorporation of PSI in electron-conducting polymer scaffolds.[39]

Polyviologens, first reported in 1971, are a unique class of organic polycationic polymers, with alternating copolymer structure featuring a viologen (N,N-disubstituted-4,4-bipyridinium dication) and a variable linker group connecting the viologen groups.[60] Aliphatic and unsaturated hydrocarbons of various carbon chain length (e.g. 3-11), as well as aromatic linker groups have been synthesized and characterized previously.[60,61,62] A generalized polyviologen structure is presented in Figure 3.1, along with the structure of a commonly cited polyviologen derivative, poly(p-xylylviologen). Although most commonly reported redox polymers involve multistep synthetic routes, polyviologens can be easily synthesized from low-cost precursors in a single step. Polyviologens possess similar electrochemical properties as electron acceptors to their monomeric counterparts that are commonly used as diffusible electrochemical mediators for PSI.[63]

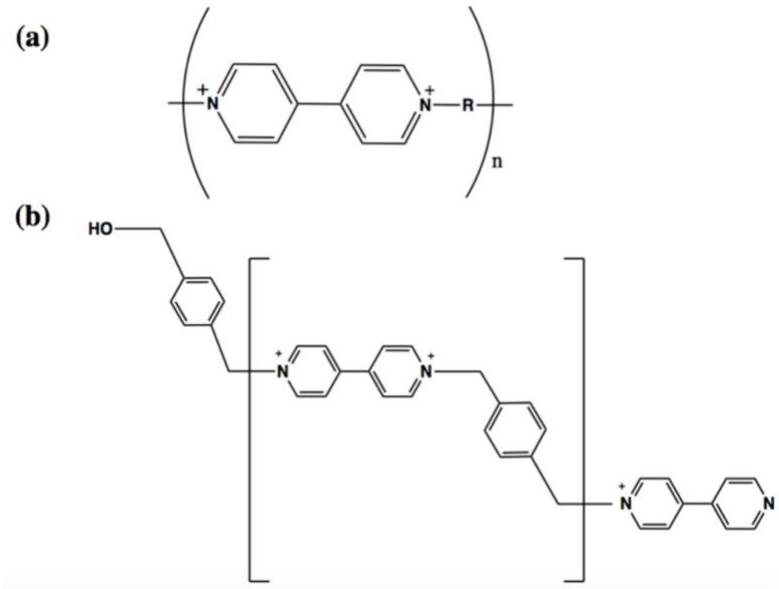

Figure 3.1. (a) General structure of the polyviologen repeating unit (b) the structure of a commonly cited polyviologen derivative, poly(p-xylylviologen) (PxV)

Similar to monomeric viologens, the redox potential of the polymeric viologens can be tuned by alteration of the N-substituted groups attached to the viologen. In polymeric form these, substituent group also serve as linkers between viologen groups in the polymer chain.[60,63] Additionally, polyviologens provide the added advantage of forming robust films due to their high molecular weights. Importantly, dry films of polyviologens have also demonstrated the ability to shuttle electrons in the solid-state.[64] The higher molecular weight contributes to the mechanical stability of the film. Polyviologens are intrinsically redox active (tied to the parent N,N'-substituted bipyridine) with more positive redox potentials than PSI's final iron-sulfur cluster (F_B). Specifically, the redox potential of poly(p-xylylviologen) is -0.196 V vs. NHE, which is energetically lower than the F_B site, making this particular polyviologen derivative ideal for accepting electrons from the reduced iron-sulfur cluster.[16,62,64,65,66] In addition, the redox potential

of the alternating copolymer can be easily tuned by switching the linker groups between the bipyridine moieties.

Polyviologens first attracted attention when Sassoon et al. reported the participation of various polyviologen derivatives in photoinitiated electron-transfer reactions through quenching photoluminescent ruthenium complexes.[62] The quenching behavior confirms that polyviologens rapidly accept excited state electrons. This was further evidenced by the later observation that photoexcited CdSe quantum dots transfer electrons to poly(p-xylylviologen) when two materials are prepared into composite solid-state films.[64,65] Not only does photoelectron transfer from photoluminescent particle to polymer occur on ultrafast time scale (<10 ps), but also the reduced poly(p-xylylviologen) is capable of subsequent electron donation to a secondary acceptor such as indium tin oxide (ITO).[64] In the context of interfacing with PSI, Yehezkeli et al. demonstrated a device architecture in which monolayers of PSI were assembled into a film with alternating layers of poly(p-xylylviologen) leading to the generation of anodic photocurrents.[67] Although a viable proof of concept, this device required an exogenous, sacrificial electron donor in a liquid electrochemical cell and the generated photocurrents were only in the nA/cm^2 range.

In the present work, poly(p-xylylviologen) (PxV) was used as the electron transport layer between PSI multilayer films and ITO electrode to construct low-cost, solid-state solar cells. An aqueous solution of PxV was deposited on PSI by vacuum-assisted drop-casting. The thin and transparent nature of the deposited polymer film allows light transmission through the film and light absorption by PSI. The device type which had the polyviologen layer situated between PSI and ITO generated a photocurrent density of 33 $\mu A/cm^2$, which is 10 times more than the PSI-only (control) devices and 30 times more than the PxV-only devices. The significant enhancement in anodic photocurrent validates the role of polyviologen in mediating electron transport from PSI to

ITO. Effective electrical wiring of PSI multilayer film to the ITO electrode was achieved through incorporation of PSI in an electron-conducting polymer scaffold.

Results and Discussion:

Depositing PSI films onto p-doped silicon (p-Si) results in significant enhancement in photocurrent when compared to metal electrodes such as gold as well as select semiconductors such as n-type silicon. The improved performance of p-Si as a photocathode interfaced with PSI is attributed to the energetic match between the Fermi level of the semiconductor (-4.65 eV vs. Vacuum) and PSI's oxidized P_{700}^{+} redox cluster (-4.93 eV vs. Vacuum).[68] The Fermi level of the p-Si wafers used in this study was calculated from the manufacturer specified resistivity. The small net difference (0.28 eV) between the two energy levels makes the electron transfer from p-Si to P_{700}^{+} highly energetically favorable. Previous work has demonstrated a dramatic increase in the measured photocurrent of PSI-based systems by using a p-Si substrate in conjunction with a liquid methyl viologen mediator.[27] However, the replacement of the liquid mediator with a solid-state electron transport material is much more appealing for large-scale practical applications as it increases operational stability in real-world settings. An electron transport material that has the proper energy alignment with PSI's final iron-sulfur cluster (F_B) is crucial in achieving a good interface between the PSI-modified p-Si and ITO. Polyviologens are intrinsically redox active with higher redox potentials than the F_B site, which makes them ideal for accepting electrons from the cluster.[63]

In this work, a commonly cited polyviologen derivative, poly(p-xylylviologen) (PxV), was synthesized by previously reported methods and characterized with ^{1}H-NMR.[60,62] Cyclic voltammetry revealed the redox potential ($E_{1/2}$) of $PxV^{2+/1+}$ couple to be -0.196 V vs. NHE (Figure 3.2). The observed potential is in good agreement with previous studies.[61,64,65] The redox potential

of PSI's final iron-sulfur cluster (F_B) sits at around -0.58 V vs. NHE.[69] This indicates that the synthesized PxV has a higher redox potential and is energetically lower than F_B and can act as an electron acceptor from PSI based on the favorable energy cascade.

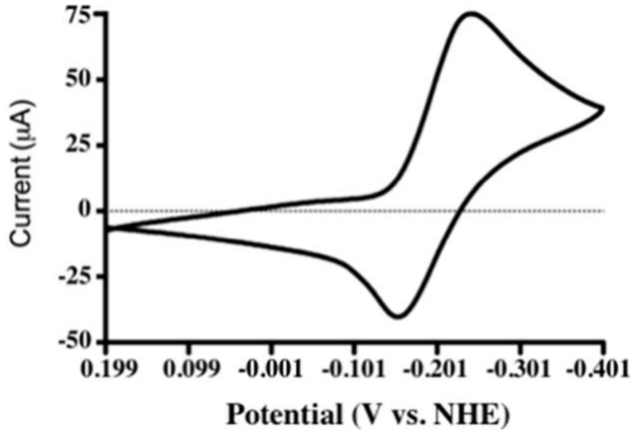

Figure 3.2. Cyclic voltammogram of poly(p-xylylviologen) polymer

A p-Si/PSI/PxV trilayer biohybrid electrode was designed and fabricated into a solid-state photovoltaic device by placing ITO-coated PET in contact with the PxV layer as an anode. Photochronoamperometric analysis revealed that the addition of PxV significantly enhances the generated photocurrent. Figure 3.3 displays the steady-state photocurrent density comparison of different types of solid-state devices. Thirty replicates of each device type were tested and the average photocurrent densities along with their corresponding standard deviations (error bars) are presented. In this two-electrode system, the underlying lightly p-doped Silicon (p-Si) was connected as the working electrode, and both the reference and counter electrode connections were attached to the ITO. When the PxV polymer is deposited on top of the PSI multilayer film as the electron transport layer, the best performing device generated a photocurrent density of 33 $\mu A/cm^2$. This is 10 times more than the PSI-only control devices and 30 times more than the PxV-only

devices. This layered device architecture also outperformed the devices with a mixed PSI /PxV polymer composite. These results indicate that the p-Si/PxV electrode is not photoactive by itself and the transparent PxV film ensures charge transfer between PSI and ITO. Overall, the thin (~0.2 μm) PxV film does not interfere with PSI's light absorption; the absorption spectra of deposited thin films of PSI and PxV on glass (Figure 3.3.b) show that PxV does not competitively absorb with PSI. PSI absorbs strongly in the red (680 nm) and blue (430 nm) regions whereas the PxV film absorbs in the green (550 nm) and orange (610 nm) regions.[15]

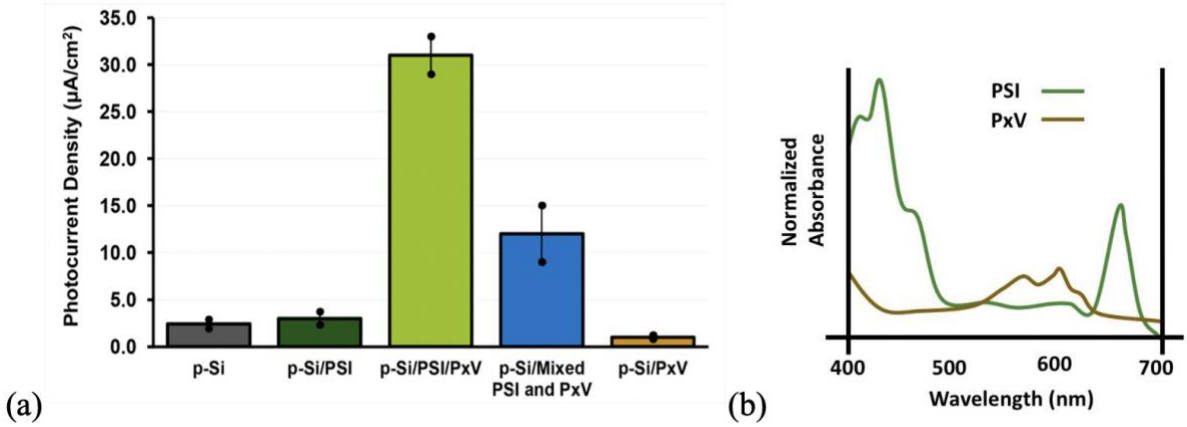

Figure 3.3. (a) Photocurrent density comparison of solid-state devices. The average photocurrent density is calculated from the steady-state current under illumination (n = 30 for each device type). The working electrode is held at the open-circuit voltage in dark. (b) Absorbance spectra of PSI and PxV deposited on glass.

In addition, p-Si/PSI/PxV devices made with hydrofluoric acid (HF) etched p-Si substrates showed around three times higher photocurrent (95 μA/cm^2) than the p-Si/PSI/ PxV devices made with unetched p-Si. Although the photocurrent density increased significantly with the removal of the insulating SiO_2 layer through HF-treatment, by lowering the internal resistance of the device,

a drop (from 250 mV to 210 mV) in the open circuit voltage (V_{OC}) was also observed. This could be because of the loss of the Schottky barrier in the device.[70] In order to make sure that the lightly p-doped silicon substrates, which are photoactive by themselves, are not contributing the observed photocurrent in the p-Si/PSI/PxV devices, the same device type was replacing the lightly p-doped silicon with heavily p-doped since the heavily p-doped silicon is not photoactive by itself. Although the photocurrents generated from the heavily doped p-Si/PSI/PxV devices were lower (by around 4 times), these devices were still photoactive due to the presence and single contribution of PSI protein complex.

To provide further evidence for PSI-based photoactivity, p-Si/PSI/PxV devices were prepared with inactivated PSI extract. Lipova et al have previously reported that heating PSI complex to above 80^{o} C leads to the complete degradation of the pigment-protein structure and hence to the loss of photochemistry.[15,71] Inactive PSI was prepared by heating of the PSI extract to 90^{o} Celsius in order to ensure complete degradation. Photochronoamperometry measurements from these devices are presented in Figure 3.4. The p-Si/PSI/PxV devices made from active PSI generated 30 times more photocurrent density than the devices made with inactive PSI. Absorbance spectra were collected from active and inactive PSI solution in phosphate buffer (pH 7). Inactive PSI does not have the characteristic 680 nm absorption peak that active PSI possesses which indicates the degradation of the pigment-protein structure and loss of photochemistry.[15]

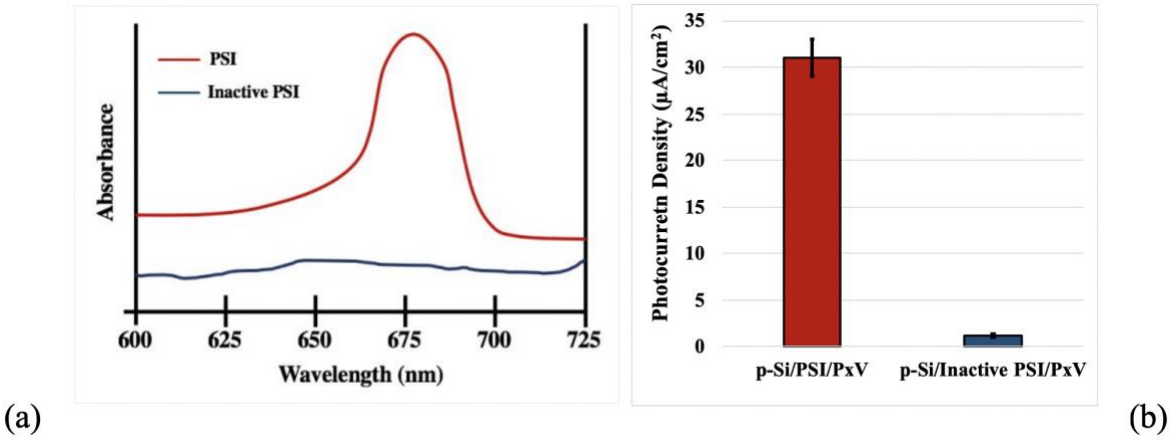

(a) (b)

Figure 3.4. (a) Absorbance spectra of solutions of active and inactive PSI in phosphate butte (pH=7). (b) Photocurrent density comparison of p-Si/PSI/PxV devices made with active and inactive PSI solution.

Since biological materials are also prone to environmental damage and degradation, performance stability in biohybrid devices is critical. To analyze the robustness of this novel device type, 30 replicates of the best performing device type (p-Si/PSI/PxV) and the control device type p-Si/PSI were tested over a period of 30 days and the change in photocurrent density over time was monitored (Figure 3.5). The error bars represent the deviation from the average photocurrent density for the 30 replicates. The devices were stored in air-tight containers in ambient conditions. For the p-Si/PSI/PxV device, there was no significant reduction in performance; the photocurrent density was retained by 97% at the end of the 30-day period, indicating that these devices are suitable for practical applications. The polymer film not only improves the photocurrent generation by aiding the electron transfer, but also helps preserve the protein film underneath. PSI-only devices experienced a 20% loss in performance after 30 days.

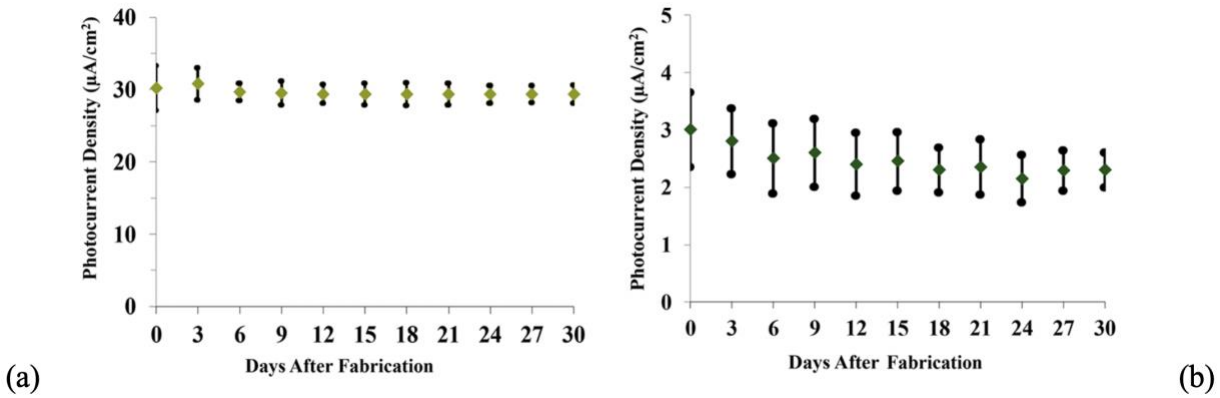

Figure 3.5. Performance stability of the p-Si/PSI/PxV (a) and p-Si/PSI (b) device types (30 replicates for each type) over 30 days. The underlying p-Si is connected as the working electrode, and both the reference and the counter electrode connections were attached to the ITO. The average photocurrent density is calculated from the steady-state current under illumination.

Current-voltage (I-V) analysis was used to further evaluate the solid-state solar devices. I-V analysis under both dark and calibrated solar illumination for p-Si/PxV control device and p-Si/PSI/PxV device are given in Figure 3.6. The short circuit current density (J_{SC}) of the p-Si/PSI/PxV device is 27 μA/cm^2, the open-circuit voltage (V_{OC}) is 250 mV and the external efficiency is calculated to be 0.0020%. Although the efficiency for the solar cell is low, the simple and inexpensive fabrication method allows for the rapid preparation of a mass number of devices in a low-resource environment. The same device type was made with HF-treated lightly p-doped silicon substrates: In the etched p-Si/PSI/PxV device, while the open-circuit voltage (V_{OC}) dropped from 250 mV to 210 mV and the short circuit current density (J_{SC}) increased from 27 μA/cm^2 to 80 μA/cm^2. Although the photocurrent density increased significantly with the removal of the insulating SiO_2 layer by lowering the internal resistance of the device, a drop (in the open circuit

voltage (V_{OC}) was also observed. As previously stated, this could be because of the loss of the Schottky barrier in the etched p-Si device.[70]

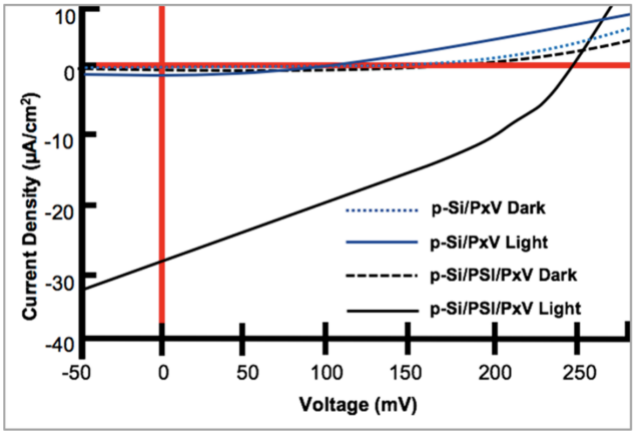

Figure 3.6. Current Density−voltage (j−V) analysis of solid-state p-Si/ PSI/PxV (black) and p-Si/PxV (blue) devices. Samples were tested under 1 sun illumination and in the dark.

The calculated external efficiency of the p-Si/PSI/PxV device is higher than the given efficiency (0.0015%) of the previously reported p-Si based PSI device that has a ZnO electron transport layer deposited using confined-plumed chemical deposition.[57] The highest reported external efficiency for a solid-state PSI device (0.0092%) was reported by Gizzie et al. in 2015, who incorporated PSI into a polyaniline conductive framework grown directly on TiO_2 electrodes and interfaced this photoactive electrode with an evaporated metallic cathode.[38] Our design uses different cathode and anode materials as well as a different conductive polymer network and deposition methods. In addition, our device fabrication methods are simple and low-cost.

In addition to enhancing the photocurrent generation, the incorporation of PxV in solid-state devices changed the shape of the photochronoamperometric curve when compared to a wet-electrochemical cell with a p-Si/PSI electrode and a liquid methyl viologen mediator. Figure 3.7

displays the photochronoamperometry scans from a liquid photoelectrochemical cell and a solid-state p-Si/PSI/PxV device. The liquid cell uses 2 mM methyl viologen mixed with 100 mM KCl as the supporting electrolyte. The cell is connected in a three-electrode system where the p-Si/PSI is wired as the working electrode, Ag/AgCl (Sat. KCl) as the reference and platinum mesh as the counter electrode.

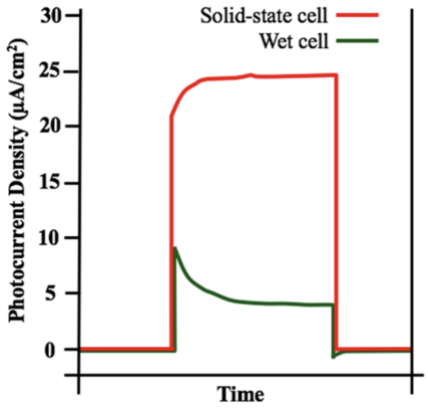

Figure 3.7. Photochronoamperometric analysis of a solid-state p-Si/ PSI/PxV device compared to a liquid photoelectrochemical cell with p-Si/PSI as the working electrode.

The electrochemical characterization revealed that the solid-state device not only improved the photocurrent density but also changed the shape of the photo-amperometric curve. The use of a liquid electrochemical mediator introduced diffusional mass-transfer limitations as indicated by the time decay, while the solid-state device did not have this decay. This pattern follows the Cottrell equation where diffusion-controlled current decays with time.[46,72] The solid-state devices reach a steady-state photocurrent faster than the wet cells. They also show higher performance stability over time. The improved photocurrent generation in the solid-state device can be attributed to the increased conductivity; the integration of PSI within a conductive PxV polymer framework helps to enhance electron shuttling processes from individual complexes within the

multilayer assembly, greatly reducing charge transfer resistances. As a result, with a smaller number of viologen charge carriers, there is an improved overall charge transfer within the solid-state conductive framework.

In an attempt to advance the performance efficiency even further, electrochemically tuned nitrogen-doped carbon dots were layered between the photoactive PSI film and the silicon cathode as a potential hole transport later. Carbon dots (CDs) are a novel class of carbon nanomaterial with tunable optical and electrochemical properties.[73] Within solar energy conversion devices, CDs have often been utilized as photocatalytic particles and charge transport materials. Specifically, nitrogen-doped CDs (NCDs) demonstrate tunable band gap and oxidation/reduction potentials based on the parameters of their synthesis procedure. [73,74] This property makes them ideal for use in systems where a material needs to energetically match another one. Peng et al. reported change in redox potential of NCDs as a result of changing the identity of the carbon and dopant source, as well as the pH of the electrolyte solution used.[75] As part of this work, in-house synthesized NCDs were drop-casted on top of the silicon substrates (drying was sped up using a hot plate at 70^{o} C), prior to the deposition of PSI and PxV through vacuum assisted drop casting. The oxidation potential of the synthesized NCDs were tuned to energetically match the reduction potential of PSI and the result was confirmed with CV experiment.[73] After photoelectrochemical characterization of devices modified with NCDs, it was found that the presence of NCD film between the silicon substrate and the photoactive PSI-polymer composite film did not significantly improve the photocurrent beyond the improvement obtained from the conductive polymer film. In addition, Si/NCD/PxV devices made without the photoactive PSI film gave similar photocurrents to Si/PSI/PxV control devices.

Conclusions:

Polyviologens can be easily synthesized from low-cost precursors and are intrinsically redox active with redox potentials slightly more positive than PSI's final iron-sulfur cluster (F_B), which makes them ideal for accepting electrons from the cluster.[62] Integration of PSI within a conductive polymer framework helps to enhance electron shuttling processes from individual complexes within the multilayer protein film.[14] When the PxV polymer is deposited on top of the PSI multilayer film as the electron transport layer, the device generated 10 times more photocurrent than the PSI-only control devices and 30 times more photocurrent than the PxV-only devices. The resulting solid-state solar devices showed significant photocurrent enhancement and increased performance stability over a traditional liquid photoelectrochemical cell. The polymer film not only improved the photocurrent generation by aiding the electron transfer, but also helped preserve the protein film underneath; PSI-only devices experienced a 20% loss in photocurrent performance after 30 days. This work presents a novel PSI-based solid-state platform for solar energy conversion.

Experimental Methods:

Extraction of Photosystem I Complex.

Full procedure for extracting PSI from baby spinach is given in Chapter II and has been adapted from Baba et al.[22] Briefly, PSI protein was isolated from commercially available organic baby spinach. Thylakoid membranes were extracted from spinach via maceration, filtration, and centrifugation. The protein was then removed from the membrane and solubilized using a high concentration of surfactant (Triton X-100) rich media. The protein was purified by hydroxyapatite column and eluted with 0.2 M sodium phosphate buffer at pH 7. The extracted PSI solution was

aliquoted into smaller volumes and stored at -80 °C. The concentration of the PSI extract was 0.9 x 10^{-6} M as characterized by the methods of Baba et al.[22] Prior to film deposition, excess surfactant and buffer salts in the PSI extract were removed via dialysis against deionized water using regenerated cellulose membrane tubing (MWCO 10 kDa).

Synthesis and Characterization of Poly(p-xylylviologen).

Commercially available reagent grade chemicals were used without further purification. Poly(p-xylylviologen) (PxV) was synthesized by previously reported methods.[60,62] Briefly, equimolar amounts of 4,4'-bypyridine and N,N′-dibromo-p-xylene were dissolved in dry acetonitrile in a round bottom flask capped with an oil-filled bubbler under N_2 atmosphere. The mixture was stirred and heated under reflux at 80^o C for 48 h. The insoluble reaction product was separated from the reaction mixture on a sintered glass vacuum filter (coarse porosity) and washed with copious amounts of acetonitrile, followed by dichloromethane. The purified yellow solid was dried under low vacuum for 2 h. The product was characterized by voltammetry and ^{1}H-NMR. Voltammetry was performed using a CH Instruments 660A workstation. An aqueous 1 mg/mL solution of poly(p-xylylviologen) was prepared, supplemented with 100 mM KCl, and then argon purged for 30 minutes to remove any residual oxygen. A 2-mm glassy carbon disk was used as the working electrode, along with a platinum mesh counter electrode and a Ag/AgCl (Sat. KCl) reference electrode. Cyclic voltammogram was collected by scanning from 0 to -0.6 V at a scan rate of 0.01 V/s. The ^{1}H-NMR spectrum of the synthesized product is given in Figure 3.8. From the integrated ^{1}H-NMR peaks, the number average molecular weight (M_n) of poly(p-xylylviologen) was estimated to be around 3200 Da, indicating an average of 12 repeating units. Both cyclic voltammetry and ^{1}H-NMR data match with previously reported values for poly(p-xylylviologen). [60,62,65]

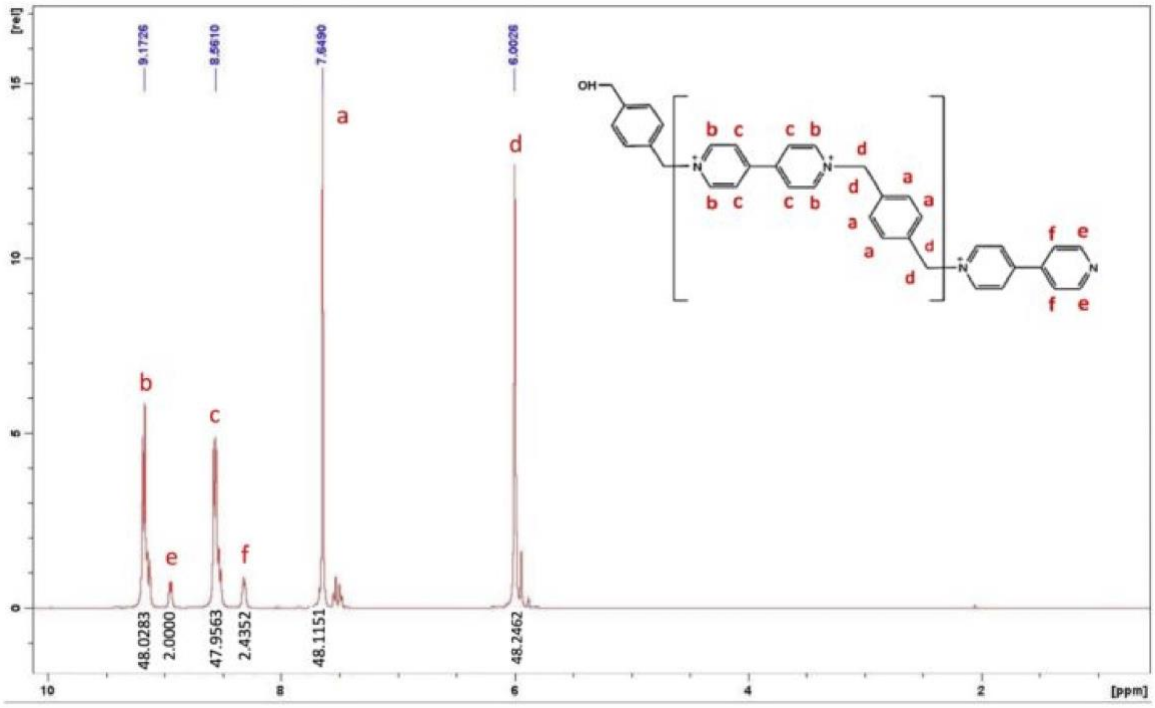

Figure 3.8. H^1-NMR spectrum of poly(p-xylylviologen) polymer

Modification of Substrates with Photosystem I and Poly(p-xylylviologen).

Lightly and heavily (boron) p-doped silicon (p-Si) substrates (1-10 Ohm-cm and 0.001-0.005 Ohm-cm respectively) were purchased from University Wafer (Boston, MA). Each substrate was masked with electrochemical masking tape (Gamry) to yield an exposed area of 1 cm^2. Multilayer films of PSI were deposited onto the unmasked area of the silicon substrates using previously described methods.[9] Briefly, 80 µL of dialyzed PSI solution was pipetted onto the exposed substrate, and a vacuum was applied to remove the solvent. This process yielded multilayer PSI films of approximately 0.4 µm thick. An aqueous 80 µL solution of 10 mg/mL PxV was pipetted onto the dry PSI film, followed by vacuum evaporation. The resulting PSI/PxV film was approximately 0.6 µm thick, indicating that the thickness of the polymer layer was around 0.2

μm. The PSI and polymer film thicknesses were optimized to yield the highest photocurrent. Film thicknesses were determined using a Vecco Dektak 150 stylus profilometer. Profilometer step height from the top of the film to the underlying p-Si was used to determine the average film thickness.

Synthesis and Characterization of Nitrogen-Doped Carbon Dots (NCDs).

The procedure for the synthesis of NCDs used in this work have been reported in a previous publication by a fellow lab member.[73]

Solid-State Device Fabrication.

Solid-state p-Si/PSI/PxV/ITO devices were completed with the addition of an ITO-coated PET anode layer (resistivity: 60 Ω/square, Sigma-Aldrich) on the p-Si/PSI/PxV electrode. In order to control the exact surface area of the contact, a small piece of transparent PET (0.283 mm^2) was pressed onto the ITO/PET layer, forcing the ITO to contact the PxV surface. For control devices, ITO was contacted on the PSI or bare p-Si surface using the same method. Structural support was provided by sandwiching the entire device stack between two pieces of borosilicate glass (1 mm thickness) and binding the system together with clamps.

Electrochemical Measurements. Devices were tested using CH Instruments (Austin, TX) CHI 660a electrochemical workstation. The reference and counter electrode lead wires from the potentiostat were connected to each other and attached to the ITO anode to form a two-electrode system. The underlying p-Si substrate was connected as the working electrode. Following the determination of the dark open circuit potential (OCP) for each device, this potential was set as the applied voltage during photochronoamperometry experiments. During photochronoamperometry experiments, a 10-s period of dark baseline current was first recorded before samples were illuminated through the transparent glass/ITO layer. Illumination was

provided by a 250 W cold light source (Leica KL 2500 LCD) generating a light intensity of 0.19 W cm^{-2}. For each chronoamperometry trial, the steady state photocurrent upon illumination was reported. For liquid photoelectrochemical cells, the PSI-modified silicon substrate was set as the working electrode, Ag/AgCl (Sat. KCl) was used as the reference, and platinum mesh wire was used as the counter electrode. The electrolyte solution consisted of 100 mM potassium chloride with 2 mM methyl viologen dichloride hydrate (MV) (Sigma Aldrich) as the electrochemical mediator.

Absorbance Spectra.

UV−vis spectra of PSI and PxV films were collected using a Varian Cary 5000 UV−vis−NIR spectrophotometer. A background of silicon and borosilicate glass was used to identify only the absorbance contributions of PSI and PxV.

Current−Voltage (i−V) Measurements.

Current-Voltage (i-V) curves for solid-state solar devices were obtained using a SolarTech xenon solar simulator with an AM1.5G filter (class A spectral match, less than 25% mismatch) connected to a Keithley 2400 source meter controlled by a custom Labview program. The lamp was calibrated to 1-sun with a NREL certified photovoltaic standard.

Chapter IV

MULTILAYER PHOTOSYSTEM I FILMS ON POROUS ITO CATHODES FOR ENHANCED AREAL PHOTOCURRENT GENERATION

Introduction:

One limiting factor within PSI-based bioelectrodes is the slow electron transfer from PSI's reaction centers to the electrode materials, which ultimately limits the produced photocurrent.[69,76,77] Electron transfer in PSI bioelectrodes can be categorized into two broad groups: direct electron transfer (DET) and mediated electron transfer (MET).[76] DET is achieved through transfer of electrons or holes from the electrode into the protein via electron tunneling.[78] MET involves the use of an electrochemical mediator to shuttle charge between either of the two active sites, P_{700}^{+} or F_B^{-}, of PSI and an electrode through a diffusion-reaction pathway.[69,78] While DET is favorable in regards to its elimination of intermediate species and associated mass transfer steps, it requires close proximity of the protein complex's active site to the electrode.[76,78,79] Many strategies have been explored with aims of maximizing electron transfer between PSI and its host electrode.[10,19] To enable DET, monolayers of PSI protein complexes have been coupled with various linking molecules and proteins, which help minimize the electrode-protein complex separation distance and also provide an energetically favorable pathway for electron transfer. Most notably, the cytochrome complex (cyt c) has been used to incorporate PSI onto a variety of electrode materials.[80,77,81,82]Alternatively, significant improvements in mediated photocurrent generation have been achieved by drop-casting thick multilayer films of PSI onto silicon, gold, and graphene electrodes.[19,27,30] Applying thicker films of PSI increases overall light absorption by providing a higher areal protein loading and increases the total amount of converted mediator.[69]

However, multilayer PSI assemblies are limited by both the diffusion rate of the mediator and the distance from individual PSI protein complexes to the electrode surface.[83,84]

Three-dimensional electrodes offer another avenue for increasing the areal protein loading.[80,81] Ciesielski et al. modified nanoporous gold leaf electrodes with PSI monolayers and achieved a 300% increase in photocurrent.[29] The improvement was credited to an increase in the electrochemically active surface area, which allowed for an increase in mediated photocurrent response. Examples of other high surface area PSI bioelectrodes include a gold nanoparticle-based approach, and a nanostructured TiO_2 and ZnO device.[33,85] In each case, the increase in photocurrent density is primarily attributed to an increase in the active electrode surface area, regardless of the prescribed electron transfer pathway. Increasing the active surface area will impact both the DET and MET response of the bioelectrode because it provides a higher surface area for either protein complex-electrode interaction or for mediator electron transfer.

Recently, methods for producing three-dimensional, transparent, and conductive ITO electrodes have spurred interest in their application to biohybrid photovoltaics. Wenzel et al. showed that photocurrents generated from photosynthetic biofilms composed of either *Nostoc punctiforme* or *Synechocystis sp*. on porous ITO electrodes are two orders of magnitude larger than those on planar ITO.[80] Stieger et al. utilized porous ITO with isolated PSI by wiring *T. elongatus*-derived PSI via cyt c to the surface of 460 nm ITO pores, resulting in a 150 $\mu A\ cm^{-2}$ photocurrent density with an applied potential of 100 mV vs. Ag/AgCl.[10] Additionally, Ciornii et al. found that porous ITO electrodes incorporating cyt c as a linking agent show a maximum performance of 270 $\mu A\ cm^{-2}$ at the 460 nm pore size in comparison to macropores up to 3 μm with an applied potential of 200 mV vs. Ag/AgCl.[86] The maximum is attributed to a maximum areal loading of cyt c and PSI on the ITO surface due to a higher protein binding capacity within smaller pores. These

reports have shown that porous ITO is an effective cathode material for PSI-based bioelectrodes in conjunction with cyt c and an applied potential to drive DET. In contrast to our work, PSI was confined to the surface through the use of cyt c as a post-deposition linking agent and is therefore limited by the surface area of the porous electrode and the capacity for areal loading of PSI and cyt c.[10,86]

Multilayers of PSI within pores can be expected to undergo mediated photocurrent production, and, therefore, may surpass the pore size limitation of previous monolayer studies. Many electrochemical mediators have been studied within PSI bioelectrodes to achieve high rates of MET.[9,32,77,87] One particularly high-performing mediator pair is 2,6-dichlorophenolindophenol (DCPIP) and ascorbate (AscH). Upon dissolution of sodium ascorbate salt into deionized water, AscH is protonated, forming ascorbic acid ($AscH_2$). $AscH_2$ then undergoes a heterogenous reaction (Rxn 1) in which two electrons and two protons are transferred to DCPIP, forming $DCPIPH_2$ and dehydroascorbate (DHA).[88] $DCPIPH_2$ is a fast electron donor to P_{700}^+, making it an ideal mediator species for shuttling charge between the P_{700}^+ reaction center and the cathode material.[32] Herein, $DCPIPH_2$ is used to ensure fast electron transfer from ITO to PSI multilayers in order to study the effect of the porous ITO morphology on MET. [88]

$$DCPIP + AscH_2 \rightarrow DCPIPH_2 + DHA \qquad \textbf{Eq. 4.1}$$

ITO nanoparticles were utilized to produce two different three-dimensional electrode morphologies, mesoporous and macroporous ITO (meso-ITO and macro-ITO). The meso-ITO electrodes bear cavities of approximately 20-100 nm, which is slightly larger than the crystallographic dimensions of the PSI complex and is hypothesized to increase the PSI-ITO

contact area.[19] Macro-ITO prepared via an ITO-coated polystyrene templating procedure provided much larger pore sizes (~5 μm). The electrochemically active surface area of both electrode morphologies was determined via capacitance cyclic voltammetry (CV). These electrodes were then modified with PSI multilayer films of various mass loadings and tested in a photoelectrochemical cell.

Our findings show that by entrapping PSI complexes in larger pores, an increase in mediated photocurrent is observed. Macro-ITO produced 42 μA cm^{-2}, approximately 3 times more photocurrent the meso-ITO and 40 times more than the planar ITO at a PSI loading of 132 mol cm^{-2}. Macropores increase photocurrent by allowing multilayers of PSI to deposit along pore walls, which increases mediator conversion within a single pore and results in an increase in MET. We discuss the effects of electrode conductivity, electrode translucency, protein loading, and electrochemical surface area in multilayer PSI-modified meso- and macro-ITO cathodes to draw conclusions about both charge transfer pathways and routes for optimizing porous bioelectrode interfaces by incorporating mediated electron transfer. Finally, this work highlights the ability of porous ITO-PSI biocathodes to improve MET at the dark open circuit potential (OCP), achieving appreciable photocurrent in the absence of surface linking agents and an applied overpotential.

Results and Discussion:

DCPIP & AscH Mediator.

The mediated electron transfer between PSI, $DCPIPH_2$, and ITO was investigated using photochronoamperometry (Figure 4.1). A multilayer film of PSI on an ITO-coated glass slide was illuminated under a 100 mW cm^{-2} white light source in the presence of 1 mM DCPIP and 5 mM AscH (green), 5 mM AscH (red), and 1 mM DCPIP (blue), while the ITO was held at the dark OCP (0.021 V vs. Ag/AgCl). The 1:5 ratio of DCPIP to AscH produced a much greater

photocurrent in comparison to the AscH only or DCPIP only solutions, and in the absence of an electrochemical mediator, the achieved photocurrent is negligible (Figure 4.1). At the P_{700}^{+} reaction site, $DCPIPH_2$ is electrochemically oxidized via Reaction 2 shown below. The final oxidized product (DCPIP) may then react at the cathode or be chemically reduced to $DCPIPH_2$ (Rxn 1).[88]

$$DCPIPH_2 \leftrightarrow DCPIP + 2e^- + 2H^+ \qquad \textbf{Eq. 4.2}$$

Excess AscH is necessary to increase the concentration of $AscH_2$, which regenerates the local concentration of $DCPIPH_2$. A steady state rate is reached and is limited by the diffusion of $AscH_2$ into the multilayer film to replenish $DCPIPH_2$.[11,12] In either the DCPIP only or AscH only solutions, the photocurrent is much lower and is limited by a reaction at one of the PSI active sites, evidenced by the flat photocurrent responses. In conclusion, $DCPIPH_2$ is capable of rapidly reducing the P_{700}^{+} site, and PSI multilayers in the presence of $DCPIPH_2$ and excess AscH on an ITO electrode produce cathodic photocurrent.[89]

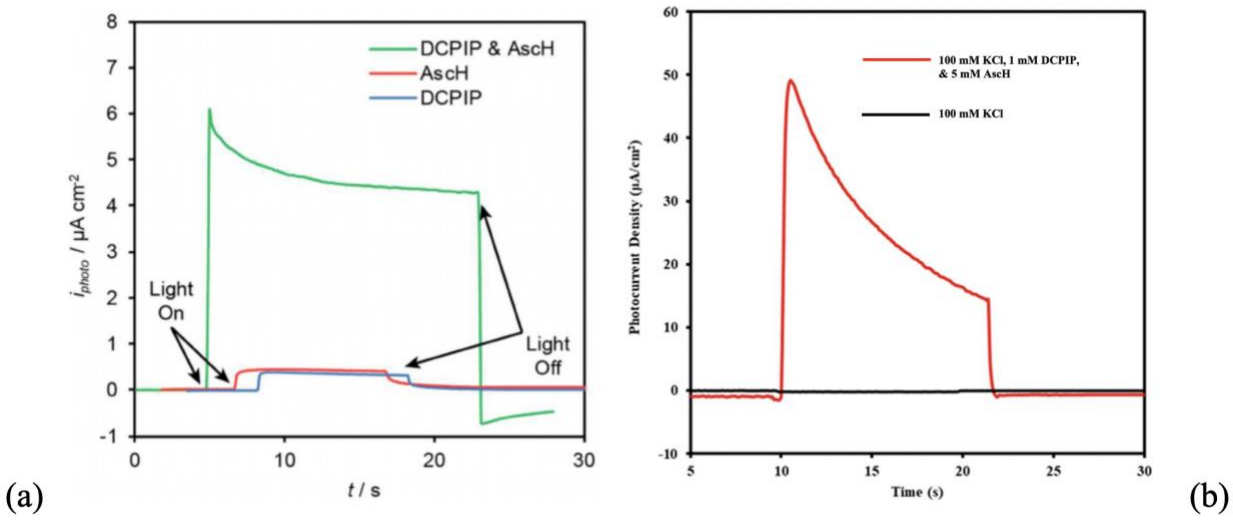

Figure 4.1. (a) Photoelectrochemical studies of DCPIP and AscH. Photochronoamperometry scans taken on a planar ITO electrode with a PSI multilayer in the presence of 1 mM DCPIP and 5 mM AscH (green) 5 mM AscH (red), and 1 mM DCPIP (blue). Photochronoamperometry studies were performed in a 100 mM KCl supporting electrolyte containing the mediator species (b) Photoelectrochemical studies with and without mediator.

Meso- & Macroporous ITO Electrode Characterization.

Mesoporous ITO electrodes were prepared by tape-casting an aliquot of suspended ITO nanoparticles (~0.1 mL) onto a cleaned ITO-coated glass slide.[90,91] The nanoparticles were then sintered under an argon environment to produce porous, translucent, and conductive mesoporous electrodes. Similarly, macroporous ITO electrodes were prepared by tape-casting ITO nanoparticles (~0.1 mL) onto a polystyrene template and simultaneously sintering the ITO nanoparticles and removing the polystyrene spheres. The polystyrene template was prepared by drop-casting polystyrene spheres onto a cleaned ITO-coated electrode and sintering the spheres at 85 °C. Due to the presence of the polystyrene spheres, the same volume of ITO nanoparticle

dispersion spreads over a larger surface area, making the resulting macro-ITO electrodes ~2 times thicker than the meso-ITO. After the porous electrode fabrication, both meso- and macro-ITO electrodes were imaged for successful ITO nanoparticle sintering and electrode quality using scanning electron microscopy (SEM). SEM also verified the absence of polystyrene spheres, which were removed during the sintering process of the macro-ITO samples. Figure 4.2 shows top down and cross-sectional SEM micrographs of the meso- and macro-ITO electrodes. Within the meso-ITO, the ITO nanoparticles pack randomly and densely, forming pore sizes between 20 and 100 nm (Figures 4.2.a and 4.2.b). These mesopores are on the scale of the crystallographic PSI complex unit cell dimensions, approximately 12 x 13 x 19 nm.[10,16] The meso-ITO electrodes have a thickness of 4.6 ± 1.3 μm via profilometry (Figure 4.10.a), and the dense porous structure extends uniformly to the substrate surface, as shown in the cross-sectional SEM (Figure 4.2). The macro-ITO electrodes yield hierarchical nanostructured pores, with larger macropores created by the polystyrene template and smaller mesopores created by the sintered ITO nanoparticles that make up the macropore walls. The intrapore connections formed by sintering the polystyrene spheres prior to the deposition of ITO nanoparticles can be clearly observed in both Figure 4.2.e and the cross-sectional SEM in Figure 4.2.f.[92] The macro-ITO electrodes have a thickness of 9.4 ± 2.0 μm via profilometry (Figure 4.10.b).

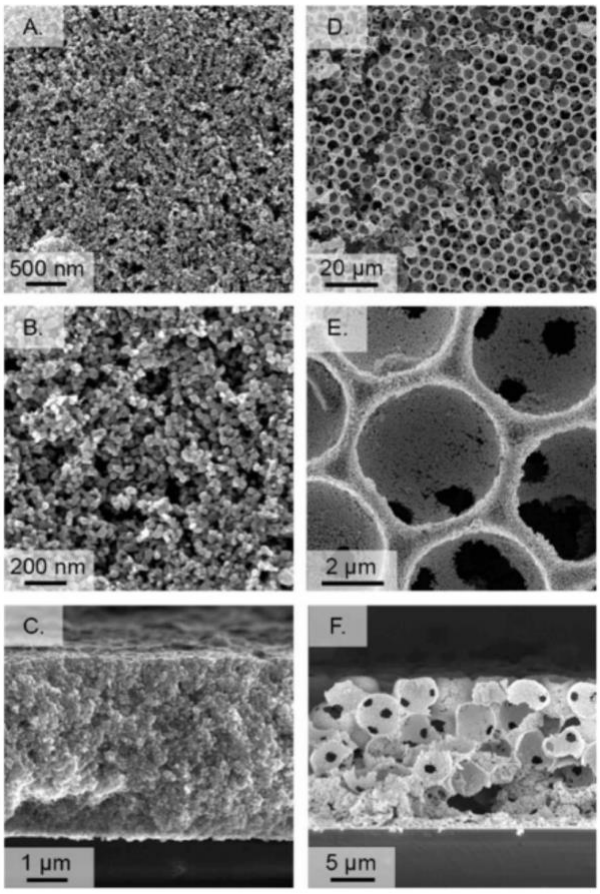

Figure 4.2. Scanning electron micrographs of: (a) Meso-ITO electrode surface, (b) Meso-ITO electrode pores on the order of 20–100 nm, (c) Cross-section of the meso-ITO, (d) Macro-ITO electrode surface showing the inverse opal structure, (e) Individual macropores with intrapore connections, and (f) Cross-section of the macro-ITO.

The crystal structure of the ITO recovered from sintered meso- and macro-ITO electrodes was analyzed using powder x-ray diffraction (XRD) (Figure 4.3). Both the conductivity and optical band gap of ITO is dependent on the crystal structure and the tin dopant concentration.[93,94] Therefore, to ensure the quality and performance of the electrodes, the ITO must remain in its body-centered cubic structure (space group = Ia-3(No. 206)) after sintering.[93] The XRD spectra for ITO recovered from both porous electrode morphologies indicate that the crystal structure is

unaffected by the sintering process and the polystyrene templating procedure. The observed peaks correspond to the desired cubic ITO phase and a table of peak assignments is given in Table 4.1.[93,94] The electrical conductivity, or, inversely, resistivity, of the electrodes is critical to the electrode performance and was measured via a four-point probe sheet resistance test. Sintering the ITO nanoparticles under an argon atmosphere resulted in highly conductive electrodes. Table 4.2 highlights the exceptional decrease in sheet resistance upon sintering for both electrode morphologies.

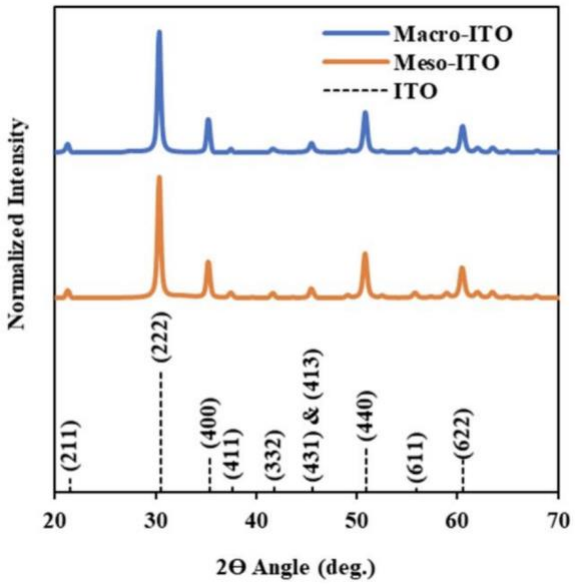

Figure 4.3 Powder X-ray diffraction (XRD) spectra for macro- (blue) and meso-ITO (orange) recovered from fabricated electrodes. The characteristic spectra for the body-centered cubic phase of ITO is given by the dashed lines (with relative intensity and crystallographic plane assignments). The characteristic spectral data is also tabulated below in Table 4.1.[93]

Table.4.1 XRD peak assignments of ITO nanoparticles recovered from porous electrodes. These peaks correspond to the body-centered cubic phase, space group Ia-3(No. 206).[93]

Crystal Plane (hkl)	2Θ Angle (deg.)	Relative Intensity (%)
211	21.46	11.0
222	30.54	100.0
400	35.41	30.4
411	37.63	5.2
332	41.78	4.5
431 & 413	45.61	3.9 & 4.5
440	50.94	36.6
611	55.89	3.3
622	60.56	26.5

In electrochemical reactions, the active surface area can be directly related to the reaction rate.[69] Therefore, to better understand the MET achieved within porous electrodes, the electrochemically active surface area should be considered. Following the procedure reported by Voiry et al., we have determined the electrochemical surface area factor (ECSAF) of the macro- and meso-ITO electrodes and used these values to approximate the active surface area.[95] By measuring the ECSAF of electrodes, the area in which a species in solution can react at the electrode surface can be studied.[42]The ECSAF can be determined by plotting the relationship of the capacitive current vs. the scan rate in a linear potential sweep test, such as CV.[95] The capacitive current, i_c (A), is known to vary linearly with respect to scan rate, v (V s^{-1}) (Eq. 4).[46,95]

$$|i_c| = AC_d v$$

Eq. 4.3

To measure the non-faradaic current, the test is conducted in a supporting electrolyte solution in the absence of any electrochemically active species. The produced current is a result of the formation of the electric double layer at the electrode surface. Figures 4.4.a-c show the large increase in non-faradaic current with respect to the scan rate for A) a planar ITO electrode, B) a

meso-ITO electrode, and C) a macro-ITO electrode. A dramatic increase is shown in the magnitude of current for the porous electrodes in Figures 4.4.b and 4.4.c. The current at various scan rates was then plotted, and the slope was used to determine the ECSAF. In Figure 4.4.d, the ECSAF was determined for the meso- and macro-ITO electrodes by normalizing their slopes to the slope found for the planar electrode, which was taken to be approximately equivalent to the geometric surface area and was thus assigned an ECSAF of one. After multiplying the respective ECSAF by the known surface area of the planar electrode (0.708 cm^2), we approximated that the meso-ITO electrodes had an active surface area of 139 ± 5 cm^2, while the macro-ITO electrodes had a much greater active surface area of 285 ± 5 cm^2. The increased active surface area in the macro-ITO electrodes is due to the decrease in nanoparticle packing efficiency on the polystyrene template, which resulted in a hierarchical porous structure and an increase in electrode thickness.

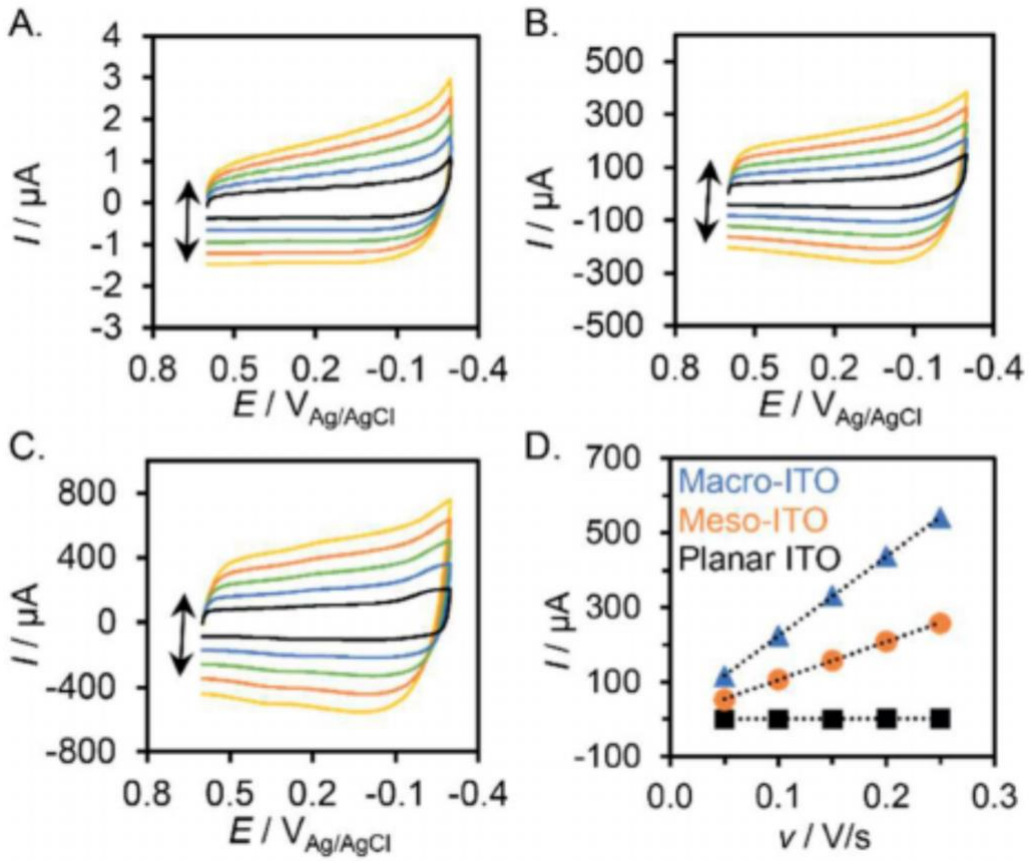

Figure 4.4. CV scans of (a) planar ITO, (b) meso-ITO, and (c) macro-ITO electrodes in an aqueous solution of 0.5 M KCl at increasing scan rates (black to yellow). (d) Scan rate plotted against the current response at 0.0 V vs Ag/AgCl (Square= planar ITO, circle= meso-ITO, and triangle= macro-ITO).

Multilayer PSI-Porous ITO Cathode Performance.

PSI was introduced into the porous electrodes via sequential drop-casting of 26 mol cm^{-2} PSI under low pressure until the desired loading was obtained. Transmission-absorbance spectroscopy was used to characterize the ability of the prepared electrodes to transmit light within the absorption region of PSI. PSI absorbs strongly at wavelengths of 680 and 450 nm.[15,22,96] Figures 4.5.a and 4.5.b show transmission spectra for planar ITO-coated glass, meso-ITO, and macro-ITO,

without and with PSI, respectively. The presence of the characteristic PSI absorption at 680 nm in each spectrum shows that deposited PSI is capable of absorbing light. The location of deposited PSI complexes was also investigated. Energy dispersive spectroscopy (EDS) mapping revealed a concentrated layer of carbonaceous material, which penetrates approximately 1 μm into the mesoporous electrode (Figure 4.8). The presence of this carbon-rich layer indicates that agglomeration or pore blockage prevents PSI from fully penetrating the meso-ITO electrodes. The EDS mapping of macro-ITO electrodes with PSI did not reveal a carbon-rich area near the surface (Figure 4.9). These results suggest that, within the macro-ITO electrodes, PSI multilayers assemble along the macropore surface, allowing for a greater PSI loading without blocking intrapore connections.

The photoelectrochemical performance of the cathodes was studied using photochronoamperometry in the 1:5 DCPIP: AscH mediator (Figure 4.5.c and 4.5.d). Both meso- and macro-ITO cathodes improve the produced photocurrent measured at the dark OCP (0.023 and 0.027 V vs. Ag/AgCl, respectively). The cathodes were tested at the dark OCP to eliminate any current driven by external forces such as an applied overpotential. The macro-ITO cathodes achieve a peak cathodic photocurrent of 42.4 ± 5.2 μA cm-2, the meso-ITO yield 10.7 ± 0.9 μA cm-2, and the planar ITO gives 1.1 ± 0.6 μA cm-2 at a PSI loading of 132 mol cm-2. We also tested porous PSI-ITO cathodes with pore sizes of 500 nm because similar pore sizes have been shown to be optimal for photocurrent generation by PSI and cyt c.[81] However, the 500 nm pore cathodes produced photocurrent values comparable to the meso-ITO (Figure 4.5.d). The achieved photocurrent for macro-ITO is high in comparison to other PSI multilayer studies on metal and metal-like substrates and shows that MET within translucent and porous ITO electrodes can improve PSI-based photoelectrochemical cell performance.[32]

The dashed photochronoamperometry curves in Figure 4.5.c, taken with a stirred electrolyte, demonstrate that a steady-state photocurrent can be achieved when the mass transport limitations within the bulk solution are eliminated.[46] This result shows that intrapore diffusion is not the cause of the large diffusional loss.

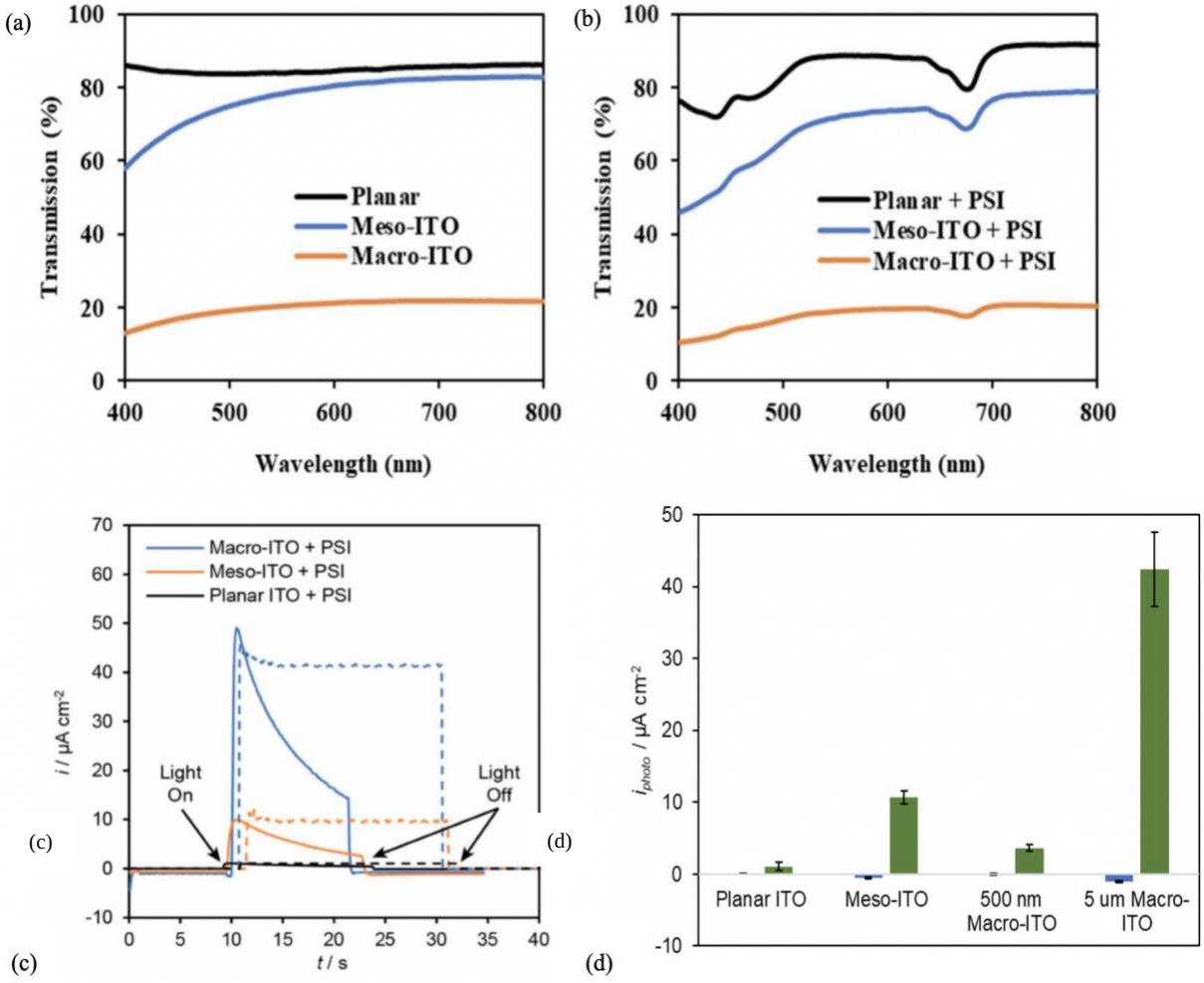

Figure 4.5. Absorbance scans of planar ITO, meso-ITO and macro-ITO (a) without PSI and (b) with PSI. (c) Photochronoamperometry scans showing the effect of stirring on PSI-modified ITO electrodes with different morphologies. (d) Data from photochronoamperometry scans of meso-

ITO, 500 nm pore size macro-ITO, and 5 μm macro-ITO with 0 mg cm-2 PSI (blue) and with 132 mol cm-2 PSI (green).

Geometric surface area is crucial to the practicality of photovoltaics because it is used to determine the footprint area needed to produce a specific amount of power. The areal loading of PSI per geometric surface area is also known to greatly influence PSI biohybrid electrode performance. By incorporating a greater quantity of PSI complexes, the concentration of the reacted mediator is increased locally, resulting in a greater photocurrent.[69,83,84] Figure 4.6 shows that increasing the PSI loading in the fabricated cathodes increases the produced photocurrent until a saturation point is reached, denoted by asterisks. The macro-ITO cathodes yield the highest saturation point between 106 and 158 mol cm^{-2} of PSI. The meso-ITO cathodes become saturated between 79 and 132 mol cm^{-2} and the planar ITO cathodes show the lowest saturation point between 52 and 106 mol cm^{-2}. At the saturation loading of the macro-ITO cathodes, the macro-ITO produces 3 times more photocurrent than the meso-ITO and 40 times more than the planar ITO. The cause of the saturation point can be attributed to both the absorption of usable radiation and the total pore volume available for PSI complexes.

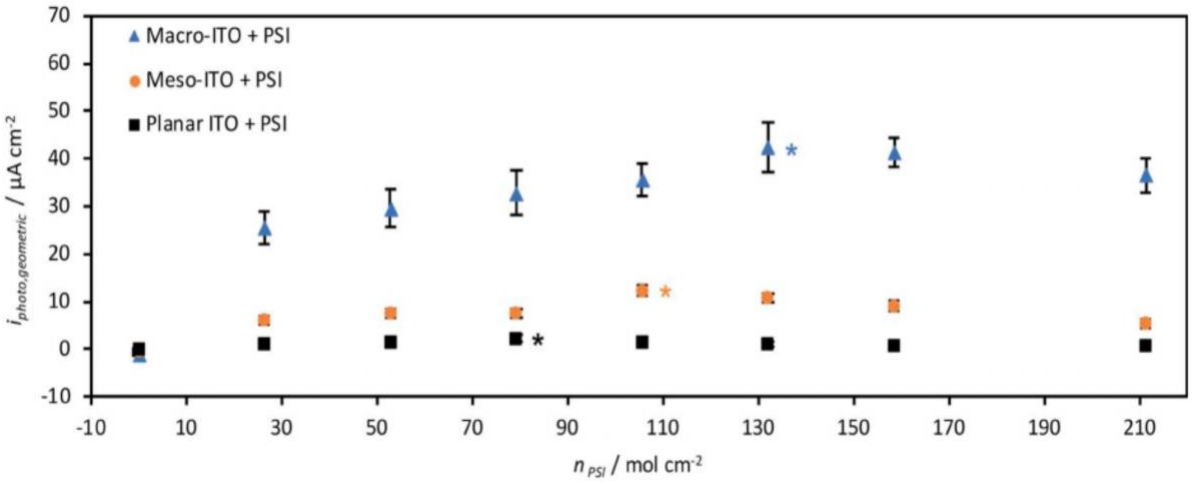

Figure 4.6. A summary of photocurrent production as a function of PSI loading on ITO electrodes in the presence of a 1 mM DCPIP, 5 mM AscH, and 100 mM KCl electrolyte. Asterisks denote the maximum photocurrent achieved for an electrode morphology.

The rate of faradaic reactions, involving charge transfer between electrochemically active species and the electrode, increases linearly with respect to active surface area.[84] Therefore, by increasing the active surface area, an increase in photocurrent should follow. To analyze how well the meso- and macro-ITO cathodes utilize their respective increase in active surface area, we defined a photocurrent factor (PCF) to be compared to the ECSAF. The PCF is simply the photocurrent produced by either the meso- or macro-ITO cathodes divided by the photocurrent produced by the planar ITO cathode at the same PSI mass loading. By comparing the PCF to the ECSAF (calculation in SI), it was found that the meso-ITO cathodes utilized 3.8 ± 1.3 % of the total active surface area while the macro-ITO utilized 7.9 ± 3.3 %. The active surface area utilized during photocurrent production by the macro-ITO cathodes remains over double that that of the meso-ITO cathodes for all PSI loadings. This result conveys that the increase in active surface area is not the only factor involved in the increase in mediated photocurrent achieved with the macro-

ITO cathodes. We conclude that the geometry of the hierarchical pore structure and the location of the PSI complexes allow for higher loadings of PSI to further increase the photocurrent in macro-ITO. PSI multilayers adhered to the inner walls of the macropores produce converted mediator, which can then react at both the pore wall under the multilayer and also diffuse through the pore to all other areas of the pore wall. Within meso-ITO, the PSI multilayers are concentrated near the electrode – bulk electrolyte interface, and therefore, reacted mediator can escape into the bulk solution more easily than in macro-ITO pores, decreasing the maximum achievable photocurrent through MET and resulting in less efficient use of the active electrode surface area. Our findings show that hierarchical pore structures on the micrometer scale are advantageous in comparison to smaller pore sizes for MET within PSI multilayers, due to an increase in PSI loading and higher concentration of converted mediator reaching the active electrode surface.

Conclusions:

The macro-ITO electrodes fabricated in this study increase the photocurrent produced by PSI multilayers via MET using a DCPIP and AscH mediator from 11± 1 μA cm-2 in meso-ITO to 42.4 ± 5.2 μA cm^{-2} in macro-ITO. We determined that the increase in active surface area was not the sole contributor to the increase in photocurrent between the meso- and macro-ITO morphologies. PSI-modified macro-ITO cathodes were capable of utilizing double the available active surface area, when compared to meso-ITO cathodes with the same PSI mass loading. Our findings show that if MET alone is considered, 5 μm pores outperformed their mesoporous ITO equivalent, while other studies that report a DET-based mechanism find that pores on the scale of hundreds of nanometers are optimal.[81] We conclude that this difference in findings is due to the difference between the electron transfer pathways. An MET approach could be incorporated in conjunction with DET strategies to further improve photocurrent within porous ITO architectures.

Future studies also will explore incorporating porous ITO-PSI biocathodes into a fully solid-state architecture in order to eliminate the need for the electrochemical mediator and provide technological viability.

Experimental Section:

Extraction of Photosystem I (PSI) Complex.

Refer to Chapter III experimental section.

Fabrication of Mesoporous Indium Tin Oxide (Meso-ITO) Electrodes.

The procedure for the porous ITO electrode fabrication was adapted from previously reported methods.[80] Conductive ITO-coated glass (Sigma-Aldrich) was cut into 2 x 1 cm pieces and sonicated (for 5 min each) in acetone, nitric acid (30%), ethanol (99%), and DI water, respectively. The ITO-coated sides of the dried glass pieces were then masked with electrochemical masking tape (Gamry) to yield an exposed area of 0.708 cm^2 (geometric surface area). The isopropanol from the original dispersion was evaporated off in a rotary evaporator at 60 ˚C, and the ITO-nanoparticles (Sigma-Aldrich, ~100 nm particle size, 30 wt. % in isopropanol) (2.5 g equivalent of nanoparticle mass only) were dispersed in 10.7 mL terpineol (Sigma-Aldrich, 90% technical grade). The resulting mixture (0.1 ml) was tape-casted onto the exposed area of the masked ITO electrodes. The nanoparticle film was first dried under ambient conditions for 48 h and then sintered in a tube furnace at 550 ˚C for 15 min under argon flow. The tube furnace was ramped up to the final temperature through a stepwise ramping procedure, never exceeding 5 ˚C min^{-1}.

Fabrication of Macroporous ITO (Macro-ITO) Electrodes.

Diluted (1:13) aqueous polystyrene (PS) dispersion (Sigma-Aldrich, Size: 5 µm, 10 w.t. %) was drop-casted onto the exposed area of the masked ITO-coated glass and allowed to dry in ambient conditions (5-6 h). The slides were then placed on an electric hotplate set to 85 ˚C for 18 h to sinter the PS spheres. 0.1 ml of the ITO nanoparticle-terpineol mixture used in the fabrication of meso-ITO electrodes was drop-casted onto the dried and sintered PS-template. The mixture was allowed to dry under ambient conditions again for 48 h, then sintered in a tube furnace at 550 ˚C for 30 min under argon flow. The tube furnace was ramped up to the final temperature through a stepwise ramping procedure, never exceeding 5 ˚C min^{-1}. A schematic of the macroporous ITO preparation is given in Figure 4.7.

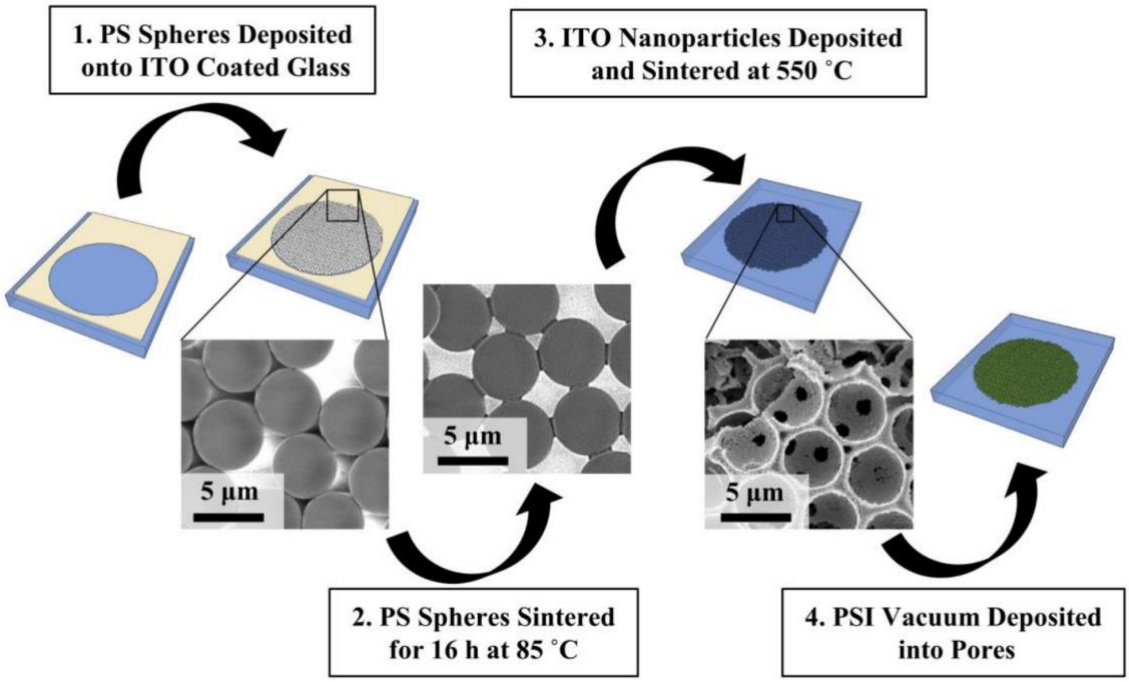

Figure 4.7. Fabrication scheme of macro-ITO electrodes adapted from Wenzel et al.[92] Polystyrene spheres (PS) (5 µm in diameter) are first deposited onto cleaned ITO-coated glass substrates. After PS are sintered on a hotplate for 16 h at 85 ˚C, ITO nanoparticles are deposited onto the PS and transferred to a tube furnace at 550 ˚C under argon to decompose the PS

template and sinter the ITO nanoparticles. Finally, the macro-ITO electrodes are modified with Photosystem I (PSI) via vacuum-assisted drop-casting. Note that meso-ITO electrodes are made in a similar manner with the PS template steps omitted.

Modification of ITO electrodes with Photosystem I Multilayers.

Prior to deposition, PSI extract was dialyzed (1:1000) against deionized water using a regenerated cellulose membrane (Spectrum Labs, MWCO: 8-10 kDa) in order to minimize the concentrations of excess surfactant and buffer salts. For deposition, a controlled amount of dialyzed PSI extract was pipetted onto the exposed area of the ITO substrate, and vacuum was applied to evaporate the solvent and leave behind a dry PSI multilayer film.[16] Due to the low surfactant concentration in the protein suspension, the resulting protein film was no longer soluble in water and could withstand electrochemical characterizations in aqueous electrolyte solutions.

Electrochemical Characterization.

Electrochemical data was collected using the CH Instruments (Austin, TX) CHI 660a electrochemical workstation. Cyclic voltammograms of planar, meso- and macro-ITO electrodes for active surface area determination was conducted in an aqueous solution of 0.5 M KCl at varying scan rates (50, 100, 150, 200, 250 mV s^{-1}). Photochronoamperometry studies were conducted in a three-electrode system with a Ag/AgCl (sat'd KCl) reference electrode, a platinum mesh counter electrode, and a PSI-modified planar or porous ITO working electrode. The dark open circuit potential (OCP) was measured and set as the applied voltage during photochronoamperometry scans. A 10 s period of dark baseline current was first recorded before samples were illuminated. Illumination was provided by a 250 W cold light source (Leica KL 2500 LCD) generating a light

intensity of 100 $mWcm^{-2}$. Stirred photochronoamperometry scans were taken by placing the sample in a 10 mL beaker containing the electrolyte and a small stir bar. Note that the stir plate introduces electromagnetic noise to the chronoamperometry data.

For the photochronoamperometry data in Figure 4.6, the cathodic photocurrent density values reported were determined by taking the difference between the initial peak current under illumination and the average dark current, divided by either the geometric surface area of the electrode (0.708 cm^2) or the electrochemically determined active surface area. Reported photocurrent density values are the average from the replicates of the same device type, with error bars representing the standard deviation from the average (n = 10). The electrochemical mediator solution used in all photochronoamperometry studies (unless otherwise stated) consisted of a mixture of 1 mM 2,6-dichlorophenolindophenol (DCPIP) and 5 mM sodium ascorbate (NaAscH) dissolved in an aqueous solution of 100 mM potassium chloride (KCl).

Electrode Characterization.

Scanning electron microscopy (SEM) images were taken with a Zeiss Merlin Scanning Electron Microscope using an accelerating voltage of either 0.5 or 5.0 keV, a working distance of 5 mm, and the InLens secondary electron detector. The low accelerating voltage of 0.5 keV was necessary for imaging the bare polystyrene beads. At higher accelerating voltages, the non-conductive beads charge and the resulting image is distorted. Energy dispersive spectroscopy (EDS) was performed using a Zeiss Merlin Scanning Electron Microscope equipped with an EDS detector (Figures 4.8 and 4.9).

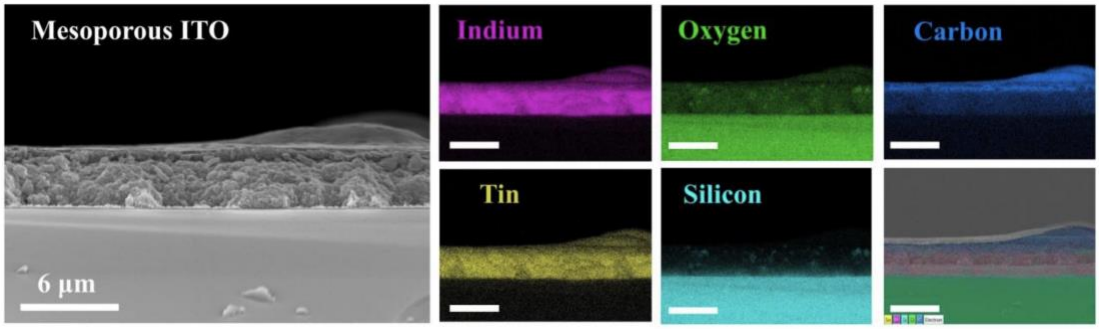

Figure 4.8. EDS mapping of a meso-ITO electrode with 106 mol cm^{-2} of PSI protein complexes deposited. Left: SEM. Right: EDS maps for indium (In), tin (Sn), oxygen (O), silicon (Si), carbon (C), and a composite map.

EDS samples were sputter coated with gold, and EDS spectra were taken at an accelerating voltage of 20 keV and approximately 3 nA probe current. Powder x-ray diffraction (XRD) was performed using a Rigaku Smart Lab X-Ray Diffractometer with a scan time of 10 min from 20 to 70 degrees using a Cu-Kα x-ray source. The sample material for XRD was recovered from prepared ITO cathodes by scraping material from the cathode onto the XRD well plate.

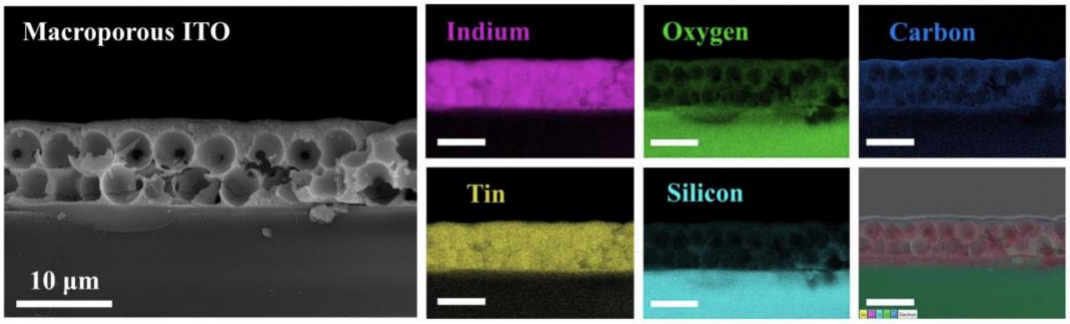

Figure 4.9. EDS mapping of a macro-ITO electrode with 106 molcm^{-2} of PSI protein complexes deposited. Left: SEM. Right: EDS maps for indium (In), tin (Sn), oxygen (O), silicon (Si), carbon (C), and a composite map.

Stylus profilometry was utilized to determine the cathode thickness using a Veeco Dektak 150 Stylus Profilometer (Figure 4.10).

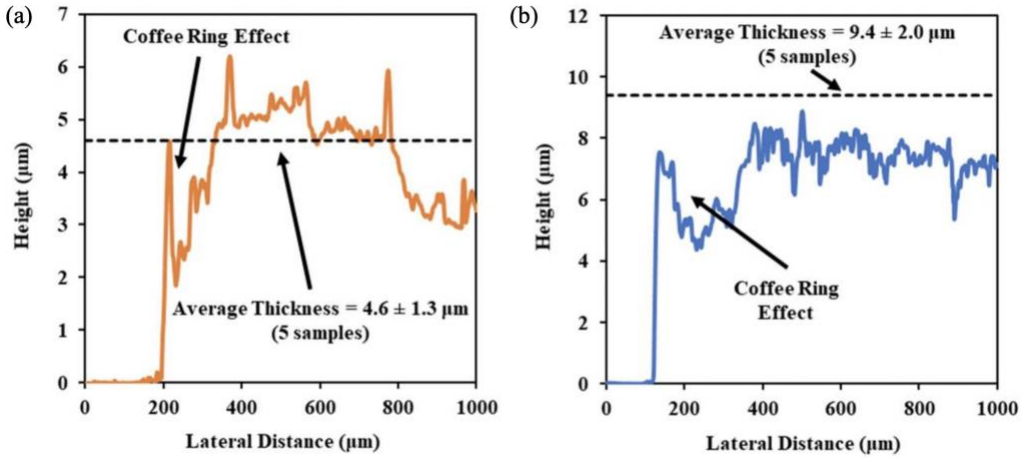

Figure 4.10. Stylus profilometry scans for unmodified (a) meso- and (b) macro-ITO electrodes.

Scans were taken over 1000 µm with the stylus beginning on the bare ITO-coated glass substrate and ending after scanning across approximately 800 µm of the electrode. The average step height was calculated and taken to be representative of the cathode thickness. The coffee-ring effect was observed and was mitigated by scanning over a larger portion of the cathode and taking the average step height. Sheet resistance was determined using an Ossila Four-Point Probe at ambient conditions on electrodes cast onto non-conductive glass substrates (Table 4.2). Each sample was tested at three locations or orientations of the four-point probe. In the event that the probe contacts mechanically damaged the cathode, the data point was discarded and recollected. Transmittance-absorbance spectroscopy was performed using a Varian Cary 5000 UV-VIS-NIR Spectrophotometer. Scans were performed from 800 to 400 nm at a rate of 600 nm min^{-1} and a sampling frequency of 1 nm. Samples were mounted to a transmittance absorbance holder and a 100% transmittance blank sample (air) was used for baseline subtraction.

Table 4.2 Sheet resistance measurements pre and post sintering for meso- and macro-ITO electrodes.

Electrode Morphology	Unannealed Sheet Resistance (kOhm/sq)	Post Annealed Sheet Resistance (kOhm/sq)
Meso-ITO	2400 ± 1300	1.4 ± 0.2
Macro-ITO	900 ± 600	3.5 ± 1.9

Chapter V

EFFECT OF DOPANT CONCENTRATION ON ELECTROPOLYMERIZED PEDOT-PHOTOSYSTEM I COMPOSITE FILMS

Introduction:

Providing an energetically favorable pathway for electron transfer and minimizing the protein-electrode separation distance plays a crucial role in achieving higher efficiencies in PSI-based biohybrid solar cells.[77] The PSI complex has previously been coupled to electrode surfaces through strategies such as covalent attachment and encapsulation within conductive three-dimensional frameworks.[16,97] These strategies have also been targeted as an avenue for maintaining stability of the electrode and improving performance in the long-term since they minimize desorption and dissolution of the complex into the electrolyte. Studies by Stieger and Ciornii et al both found that wiring monolayers of PSI onto porous ITO via cytochrome c (cyt c) complex showed increased direct electron transfer between the protein and the electrode in the absence of an electrochemical mediator in the electrolyte solution.[10,35] Another study by Wang et al constructed a hybrid photoanode that integrated Photosystem II (PSII) with a Fe_2O_3 nanorod film through self-assembly.[98] PSII was bound within the pores and channels of the hematite and the electrons generated from the oxidation of water by PSII were directly injected into the valence band of the hematite. The authors claimed that the effective attachment and orientation of PSII led to a decrease in charge transfer resistance. In a different approach, redox-active hydrogels were used for the immobilization of PSI and PSII.[99] The hydrogels were loaded with osmium, ruthenium and cobalt complexes in order to increase the diffusion coefficient of electrons through the material. These studies showed that hydrogel immobilized PSI and PSII produced photocurrent densities that surpassed the values obtained from multilayer films of PSI and PSII on metal

substrates. A study from 2011 showed that incorporating PSI within an osmium-based hydrogel results in PSI turnover rates that are seven times that of natural photosynthesis.[100]

The most recent direction that researchers have taken in order to optimize charge transfer efficiency in biohybrid systems is utilizing conductive polymer scaffolds.[16,39] Organic conductive polymers such as polyaniline, polypyrrole, polyviologens, polythiophene and their derivatives have important uses in energy storage systems, energy conversion devices and sensors.[101,102] Amongst different types, the polythiophene derivative, poly(3,4-ethylenedioxythiophene) (PEDOT), is well known for its high conductivity, stability, flexibility and processability.[103] Another advantage of PEDOT is that it can be electrochemically synthesized directly on the conductive surface it needs to be deposited on, forming films of desired thicknesses and properties. This synthesis method is also known as electropolymerization.[104] PEDOT electropolymerization can be carried out using either organic or aqueous electrolytes; for example, acetonitrile is a commonly used aprotic electrolyte solvent that is known to produce high-quality PEDOT films.[105] However, acetonitrile is not ideal to work with since it can be extremely harmful to humans and the environment if not handled properly. Not only is it toxic by skin absorption and inhaling, but it also attacks different types of plastic, setting requirements for the types of equipment that can be used with it.[106,107] Hence, electropolymerizing PEDOT from water is considered to be more advantageous even though it has its own limitations. One of the main limitations of aqueous PEDOT electropolymerization is that the EDOT monomer has low solubility in water (2.1 g/L), which means that the rate of the polymerization reaction is slow.[108] Another limitation is that the conductivity of the films produced with aqueous electrolytes tends to be lower than their organic counterparts.[105,109] Regardless of these limitations, using an aqueous electrolyte solution to synthesize PEDOT films on conductive substrates provides immense advantages when working

with biohybrid systems such as PSI-modified electrodes. Although the stability of PSI in organic solvents has not been studied very well, its stability in aqueous electrolytes has been well established in the field.[18]

PEDOT can also be distinguished from other conductive polymers with its ability to store a large amount of charge and to work as a capacitor and battery at the same time.[110] Doping of anions into the polymer backbone while the polymer is oxidized facilitates charge storage. The oxidation results in positively charged sulfur centers, which are then compensated by the dopant anions (Figure 5.1).[110,111] In order to transport mobile electrical charge through, PEDOT should be in a positively charged state and possess unpaired π electrons along its backbone. In a solution and/or during electropolymerization, PEDOT electrostatically binds to the negatively charged molecules and atoms around it via coulombic interactions.[111,112] This binding is also called doping. These negatively charged molecules or atoms must to be small enough to physically access the positive charge within the PEDOT structure. Since the polymer backbone is the conductive component of PEDOT polymer, the ratio of PEDOT to dopant anion is important in determining overall electrical properties.[103] The identity of the dopant anion can also give the PEDOT film different physical, optical and electrochemical features. A study by Rudd et al. has reported that the identity of the doping anion can affect the charge carrier mobility of PEDOT by an order of magnitude influencing the way PEDOT chains stack together.[113] Their samples were prepared via vapor-phase-polymerization (VPP) in an aqueous mixture of butanol and ethanol and in the presence of different anion dopants such as NO_3^-, Cl^-, and ClO_4^-. In addition to the changes in electrical properties, changes in optical properties were also observed both in polymeric chains in solution and in thin-film coatings.

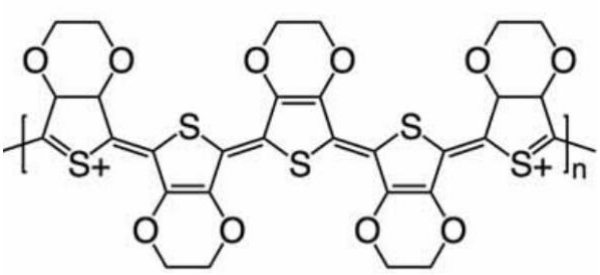

Figure 5.1. Poly(3,4-ethylenedioxythiophene) (PEDOT) structure

This work reports the electrochemical synthesis of PEDOT in different aqueous salt solutions and in the presence of PSI complex, thereby creating composite PEDOT-PSI films on top of transparent ITO-coated glass substrates. Electropolymerization in the presence of PSI creates a matrix where the protein complex is enveloped in a three-dimensional conductive polymer framework. The films were prepared potentiostatically (under applied constant potential), from an aqueous solution of EDOT precursor and desired salt (to provide the dopant anion). The electrochemical, physical and optical properties of the films were dependent on the identity of the counter ion incorporated as dopant. Incorporating PSI into the polymer film resulted in an improvement in photocurrent density obtained in the presence of methyl viologen mediator in three out of the five types of PEDOT films tested. We assume that the reason the other two films did not show an improvement is because PSI was not able to penetrate into the films, hence the photoactive component was not present.

Results and Discussion:

The films were synthesized in a three-electrode configuration where the working electrode (WE) is the ITO-coated glass, the counter electrode (CE) is platinum mesh, and the reference electrode is Ag/AgCl (sat'd KCl) (Figure 5.2). The properties of the synthesized PEDOT and

PEDOT-PSI films were investigated by absorbance spectroscopy, scanning electron microscopy (SEM), four-point probe, cyclic voltammetry, and photochronoamperometry with 0.2 M methyl viologen redox mediator. PEDOT and PEDOT-PSI films were electropolymerized onto transparent ITO-coated glass electrodes from a precursor solution of 0.01 M EDOT and 0.1 M salt (four different salts were tested as anion dopant: KBr, KCl, KNO_2, KNO_3, NaPSS).

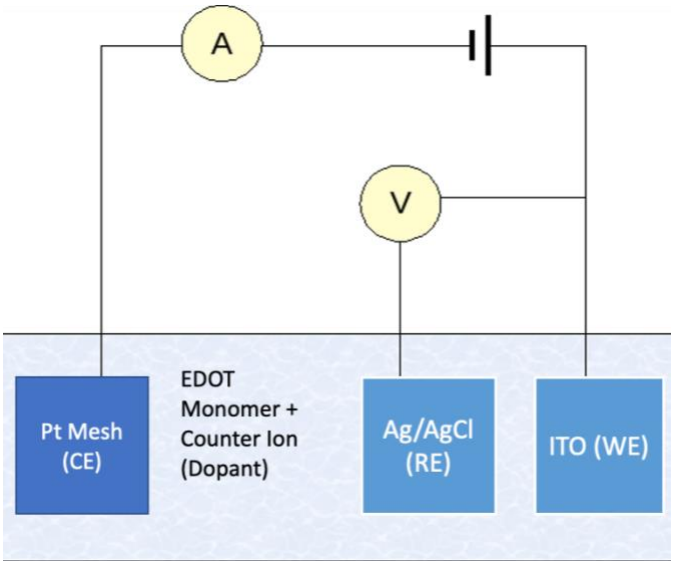

Figure 5.2. Three-electrode PEDOT electropolymerization setup.

The visible absorbance spectra (Figure 5.3a-c) showed that only three out of the five dopants resulted in a film with observable amount of PSI. These three dopants were KBr, KCl and KNO_2 and their films all had PSI's characteristic 430 nm peak (but not the 680 nm peak). PSI extract and PSI films typically strongly absorb at 430 nm and 680 nm due to the presence of pigment chlorophyll *a* (Chl *a*) inside them. As seen below, none of the PEDOT-only films had peaks around 430 nm (or 680 nm). Another interesting observation came from the SEM images which were all taken at an accelerating voltage of 2.00 keV, working distance of around 4.5 mm and magnification of 50 kX (Figure 5.3.d-f). These images showed that the PEDOT films made from different dopant anions formed different patterns as they electropolymerized and looked

significantly different from each other at the same magnification. Specifically, they were distinguished by the size of the features and the porosity. Using different dopant anions also resulted in slightly different colored films: PEDOT-Br was light blue, PEDOT-Cl was dark blue, PEDOT-NO_2 was orange/brown, PEDOT-NO_3 was brown, and PEDOT-PSS was dark blue. These differences in physical appearance might hint at differences in electrochemical properties.

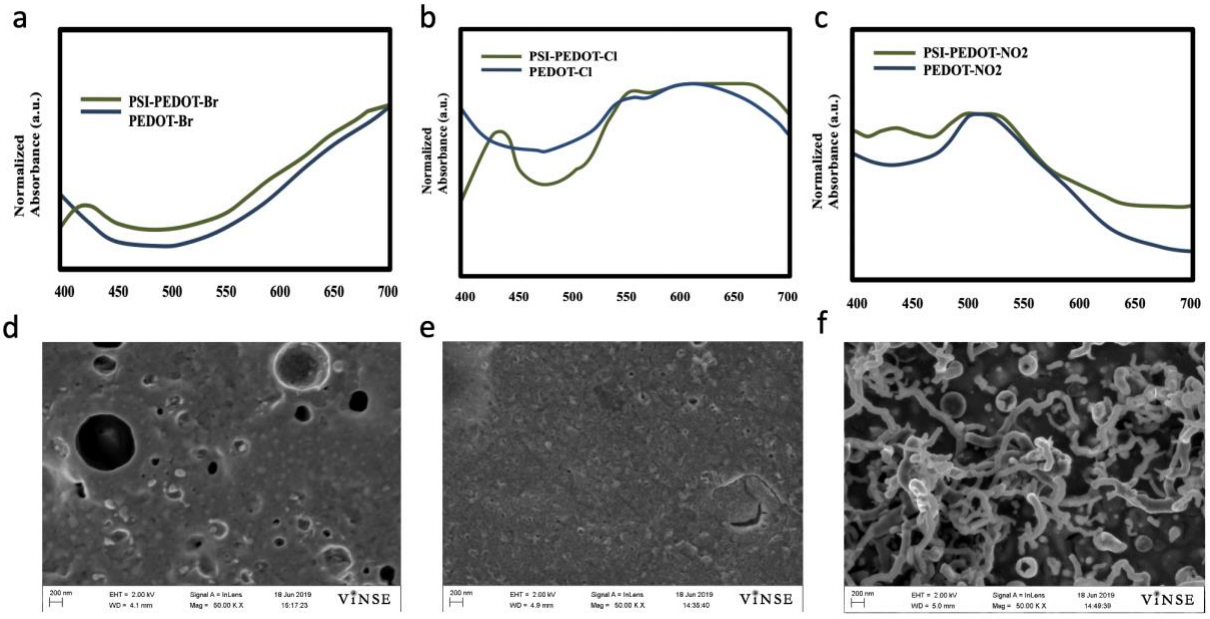

Figure 5.3. (a) Absorbance spectra of PEDOT and PEDOT-PSI made with (a) Br^- dopant, (b) Cl^- dopant and, (c) NO_2^- dopant. SEM images of PEDOT films made with (d) Br^- dopant, (e) Cl^- dopant and, (f) NO_2^- dopant.

The four-point probe technique was used to measure the sheet resistance of a thin film or a substrate. While current is forced through the two outer probes, the voltage across the two inner probes is monitored, which allows the measurement of the resistivity. In Figure 5.4, the sheet resistance of electropolymerized PEDOT films with different anion dopants is shown and compared to the sheet resistance of planar ITO electrode. As expected, the sheet resistance

increases when ITO electrodes are coated with PEDOT films regardless of the type of anion dopant. While PEDOT-NO_2 has the lowest resistance, PEDOT-Cl has the highest resistance. The resistance of PEDOT-Cl is three orders of magnitude higher than the resistance of planar ITO electrodes.

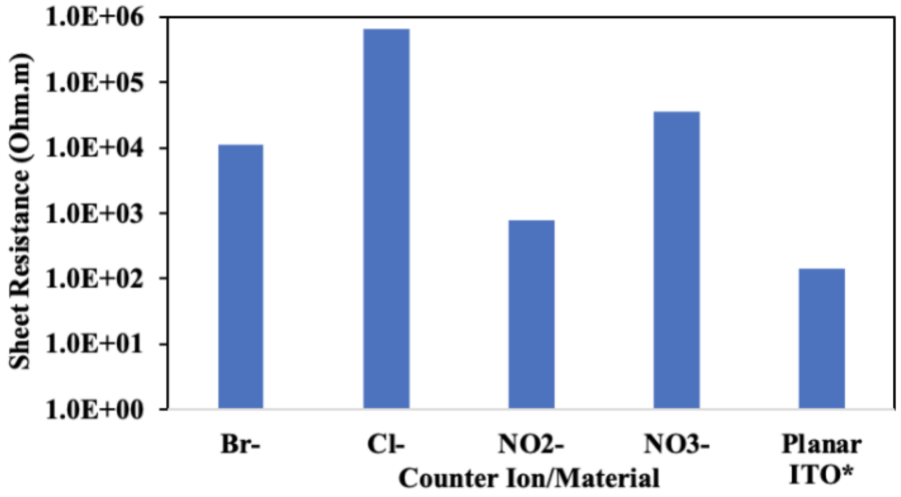

Figure. 5.4. Four-point probe measurements of different PEDOT films compared to planar ITO. * ITO-coated glass was purchased from Sigma-Aldrich and sheet resistance was calculated from the resistivity value given on the Sigma-Aldrich website.

Cylic voltammetry scans of PEDOT films in 500 mM KCl (aq.) electrolyte solution allow the observation of capacitive behavior. Capacitance is the ratio of the change in charge to the change in applied potential. So, a higher difference between anodic and cathodic currents at a specific potential means higher capacitance. Figure 5.5.a shows that the capacitive behavior is the most prominent in PEDOT-Br film, the second most prominent in the PEDOT-NO_2 film, the third most prominent in the PEDOT-Cl film, the fourth most prominent in the PEDOT-NO_3 film, and the least prominent in the PEDOT-PSS film. Interestingly, the top three capacitive film types were also the ones that showed the presence of PSI in them, in the absorbance spectra. Although this

does not necessarily mean that higher capacitive behavior corresponds to better ability to retain PSI in the film, this correlation can be further explored in a future study. Figure 5.5.b demonstrates a photochronoamperometry scan comparison of PEDOT-Br versus PEDOT-Br-PSI. The presence of PSI in the film significantly boosts the photocurrent generated (~$4.0x10^{-6}$ A). Similar photocurrent improvements were also observed with PEDOT-NO_2-PSI and PEDOT-Cl-PSI films when compared to their non-PSI controls.

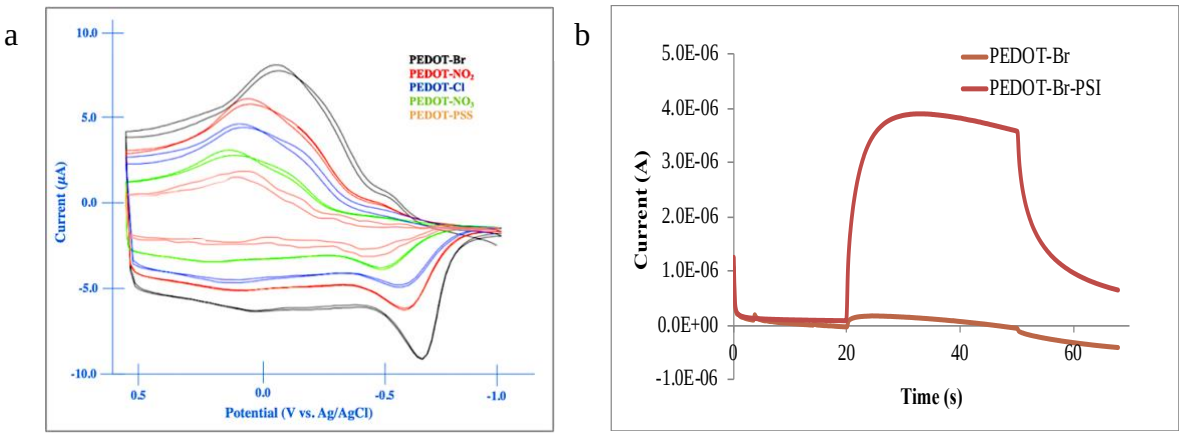

Figure 5.5. (a) Cyclic voltammetry scans of PEDOT films with different dopant anions (b) Photochronoamperometry scans of PEDOT-Br films vs. PEDOT-Br-PSI film

Figure 5.6 shows a summary of the average photocurrent densities obtained with different types of electropolymerized PEDOT films. In each of the three types (PEDOT-Br, PEDOT-Cl and PEDOT-NO_2), there is at least 4-times increase in photocurrent density in the presence of PSI. This improvement was not observed for PEDOT-NO_3 or PEDOT-PSS in any of the replicates and the photocurrent density generated was similar between the films with and without PSI. The photocurrent performance was not significantly different across the three film types, even though they all had different sheet resistances and varied greatly in physical appearance. Another important observation was that the replicability of the improved performance with the addition of

PSI into the films was less than 50% for all of the three dopants shown below. This indicates that the electropolymerization procedure produces inconsistent results and needs to be improved in a way that improves consistency and replicability.

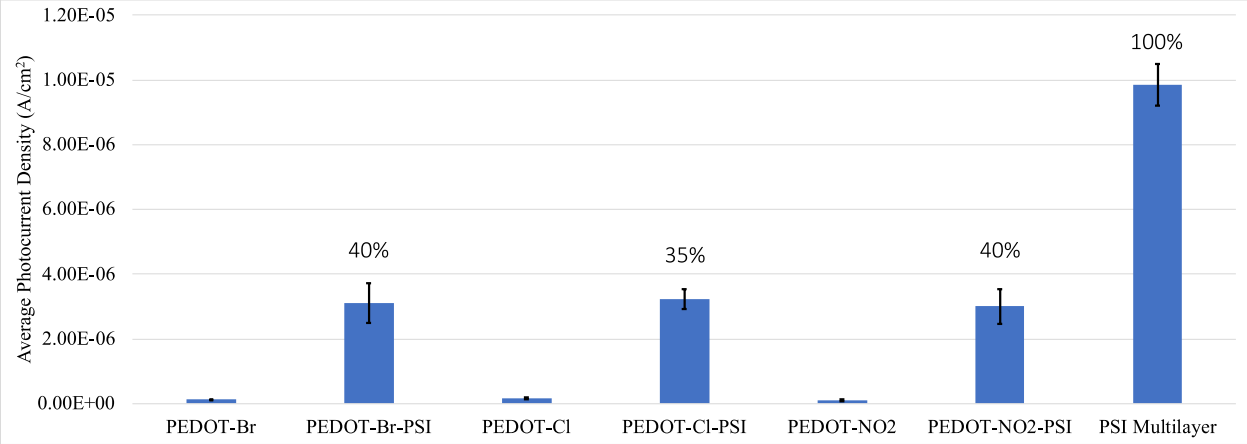

Figure 5.6. Average photocurrent densities for PEDOT and PEDOT-PSI films with different dopant anions (n=3 for each film type). Presence of PSI significantly boosts the performance.

Although there is an improvement in the presence of PSI in some of the replicates, it is important to note that multilayer films of PSI which are drop casted on planar ITO electrodes generate much higher photocurrent densities when tested in 0.2 M methyl viologen mediator. Hence, the performance limiting factor in polymer-PSI composite is most likely the amount of PSI which can be entrapped inside the film. Going forward, it is important to design experiments which can quantitatively study the amount of PSI that is in electropolymerized PEDOT films in order to come up with an estimate on how much photocurrent is produced per PSI molecule. The quantity s important in order to further the understanding on whether the presence of the conductive polymer improves charge transfer to and from a single PSI molecule. Following PCA experiments, the sheet resistances of different film types did not correlate with their photocurrent performance,

suggesting that the interconnectedness of protein and polymer might not be playing a crucial role in achieving effective charge transfer.

Conclusions:

In summary, the incorporation of PSI into electropolymerized PEDOT films resulted in an improvement in photocurrent densities in three of the five dopant anions tested. The replicability of this improvement was less than 50% for all of the three dopants, meaning that less than 50% of the samples tested resulted in an improved performance. Similarly, the films made from the same three dopants demonstrated the presence of PSI in their structures in the visible absorbance spectroscopy scans, while the fourth dopant did not. Overall, the identity of the dopant directly affected some of the properties of the resulting film. For example, different film types had significantly different sheet resistances, capacitive behaviors and physical features. However, the photocurrent performances did not vary significantly. Even though the boost in performance was impressive, multilayer films of PSI which are drop casted on planar ITO electrodes generate slightly higher photocurrent densities than PEDOT-PSI films when tested in the same mediator. Exploring strategies to incorporate more PSI into the polymer films remains crucial in achieving better performances. This can be done by changing the parameters of the potentiometric deposition experiment, varying the concentrations of precursors and exploring other negatively charged ions as dopants. A completely different avenue which also can also be explored in order to produce high-performance devices is building solid-state solar cells by sandwiching PEDOT-PSI films between the electrode and a semiconducting material such as TiO_2 (Figure 5.7). So far, almost all PSI-based solid-state architectures have included a type of conductive polymer as either an electron or hole transport layer.[18] Finding a suitable semiconducting material which is

energetically aligned with the composite film might also help to boost the performance and to maintain stability of the electrode over time.

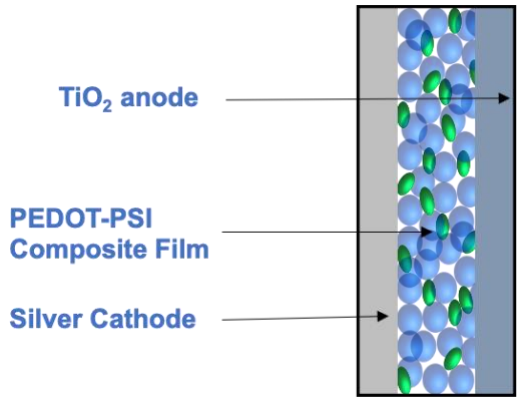

Figure 5.7. Proposed solid-state solar cell with PEDOT-PSI composite film. TiO_2 anode can be replaced with different semiconductor materials.

Experimental Section:

Extraction of Photosystem I (PSI) Complex.

Refer to Chapter III experimental section.

PEDOT electropolymerization on ITO-coated glass electrodes.

Conductive ITO-coated glass (Sigma-Aldrich) was cut into 2 x 1 cm pieces and sonicated (for 5 min each) in acetone, nitric acid (30%), ethanol (99%), and DI water, respectively. The ITO-coated sides of the dried glass pieces were then masked with electrochemical masking tape (Gamry) to yield an exposed area of 0.708 cm^2 (geometric surface area). The electrochemical synthesis was carried out on a CHI 660a electrochemical workstation. All solutions were prepared in DI water and the potentials are refenced to Ag/AgCl (aq.) electrode. The electrolyte solution

consisted of 0.1 M salt (KBr, KCl, KNO_2 KNO_3) and 0.01 M EDOT. A three-electrode cell was used for the electrochemical process where the counter was Pt mesh.

Electropolymerization of PEDOT-PSI composite films on ITO-coated glass electrodes.

The same procedure as the previous section. The additional step was 1/5 of the DI water used to make the precursor solution with undialyzed PSI extract.

Four-point probe measurements.

Sheet resistance were carried out on an Ossila Four-Point Probe. Each sample was tested at two locations or orientations and if the probe contacts mechanically damaged the cathode, the data point was discarded and recollected.

Electrochemical Characterization.

Electrochemical data was collected using the CH Instruments (Austin, TX) CHI 660a electrochemical workstation. Photochronoamperometry (PCA) studies were conducted in a three-electrode configuration with a Ag/AgCl (sat'd KCl) reference electrode, a platinum mesh counter electrode, and a modified ITO working electrode. The dark open circuit potential (OCP) was measured and set as the applied voltage during the PCA scans. A 20 s period of dark baseline current was first recorded before samples were illuminated for 30 s10. Illumination was provided by a 250 W cold light source (Leica KL 2500 LCD) generating a light intensity of 100 $mWcm^{-2}$. The photocurrent density values reported were determined by taking the difference between the peak current under illumination and the average dark current, divided by the geometric surface area of the ITO electrode (0.708 cm^2). The working electrode area was controlled by masking the electrode with Gamry electrochemical masking tape. Reported photocurrent density values (in the

bar chart) are the average from the replicates of the same device type, with error bars representing the standard deviation from the average (n = 3). The electrochemical mediator solution used in PCA scans consisted of 0.2 M methyl viologen dissolved in an aqueous solution of 100 mM potassium chloride (KCl). Similar to PCA scans, cyclic voltammetry scans were also taken using the same three-electrode configuration. This time, however, the electrolyte solution only consisted of 500 mM KCl and no electrochemical mediator. The initial scan polarity was set to positive and the potential window was set between -1.0 and 0.5 V.

Scanning Electron Microscopy.

Scanning electron microscopy (SEM) images were taken with a Zeiss Merlin Scanning Electron Microscope using an accelerating voltage of 2.0 keV, a working distance of 4-5 mm, and the InLens secondary electron detector. The images presented in this work were all taken at a magnification of 50 kX.

Absorbance Spectroscopy.

Absorbance scans of PEDOT-PSI composite films were collected using a Varian Cary 5000 UV−vis−NIR spectrophotometer. ITO-coated glass slide was used as reference to subtract the background absorption. The scan range was from 400 nm to 700 nm.

Chapter VI

SUMMARY AND OUTLOOK

Summary:

Light-harvesting pigment-protein complexes can be incorporated into biohybrid systems as the macromolecular photosensitizer. These biohybrid electrodes have a wide range of applications from photo-switchable biosensors (e.g. detection of herbicides) to solar to chemical (H_2 production through water splitting) and solar to electrical (solar cells) energy conversion. Photosystem I (PSI) is one of the most promising light converting complexes due to its ease of extraction (from plants, algae and cyanobacteria), abundance in nature, lack of toxicity and excellent optoelectronic properties. PSI has an internal quantum efficiency near 100%, one of the lowest reduction potentials observed in nature, and a higher thermal stability than most other protein complexes. In this dissertation, efforts of interfacing PSI with conductive three-dimensional frameworks are described: These frameworks include conductive polymer scaffolds, nanocarbon materials and porous transparent metal oxide electrodes. In an effort to achieve better performance, PSI complex has been functionalized in both solid-state and liquid-state solar energy conversion architectures (Figure 6.1). Although the photocurrent performance of PSI-based biohybrid devices have steadily improved over the recent years, the efficiency of the energy conversion remains low compared to traditional solar cells. Hence this dissertation also discusses several strategies and methods for improving the efficiency and long-term stability of PSI-based solar cells. It specifically focuses on optimizing electron transport to and from the complex and on maintaining the structural and functional stability of the complex while it is incorporated into the electrode.

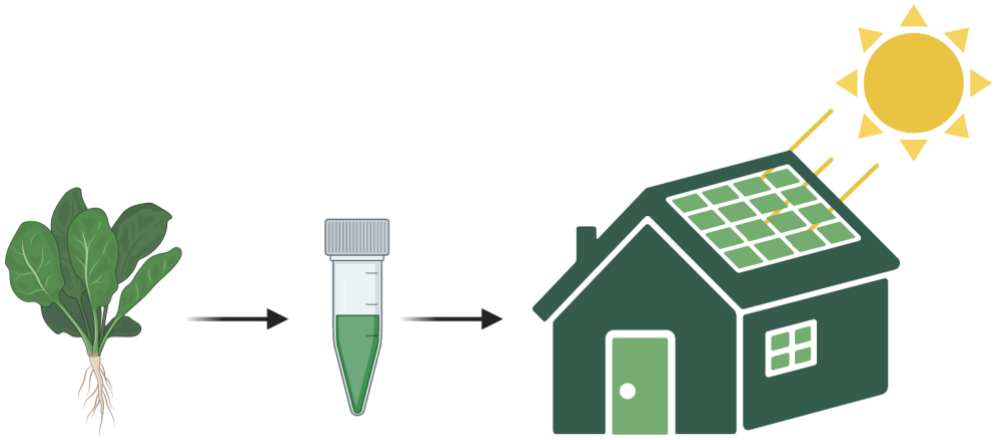

Figure 6.1. PSI complex extracted from spinach leaves can be used to make solar energy conversion devices (i.e. solar cells) (Created with BioRender.com).

Chapter II gave detailed descriptions of all the general experimental methods used to carry out the research. These methods included PSI extraction procedure from baby spinach leaves, PSI quantification with Baba's assay, photoelectrochemical analysis of PSI-modified electrodes, cyclic voltammetry, contact profilometry, UV-vis spectroscopy, scanning electron microscopy, and energy dispersive x-ray spectroscopy. Chapter III described the utilization of polyviologen polymer derivative as electron transport material and nitrogen-doped carbon quantum dots as hole transport material in PSI-based biophotovoltaic cells. Integration of PSI within this conductive polymer framework helped to enhance electron shuttling process from individual PSI complexes within the multilayer film. When the polyviologen derivative was deposited on top of the PSI as the electron transport layer, the device generated 10 times more photocurrent than the PSI-only control devices and 30 times more photocurrent than the polymer-only devices. The resulting solid-state solar devices showed significant photocurrent enhancement and increased performance stability over a traditional liquid photoelectrochemical cell. Incorporation of energetically tuned nitrogen doped carbon dots as the hole transport material in the same device architecture did not

result in an improvement in photocurrent performance. Chapter IV described efforts of incorporating PSI into porous ITO cathodes for enhanced areal photocurrent generation. For this, meso- and macroporous ITO electrodes were prepared by sintering ITO nanoparticles under high heat onto a conductive surface. Then PSI complex was drop casted on top as a multilayer film. The macro-ITO electrodes increased the photocurrent produced by PSI multilayers via mediated electron transfer using a DCPIP and AscH mediator from 11 μAcm^{-2} in meso-ITO to 42.4 μA/cm^2 in macro-ITO. The increase in active surface area was not the sole contributor to the increase in photocurrent between the meso- and macro-ITO morphologies. PSI-modified macro-ITO cathodes were capable of utilizing double the available active surface area, when compared to meso-ITO cathodes with the same PSI mass loading. Chapter V described the effect of dopant concentration on the conductivity of electropolymerized PEDOT-PSI composite films. Based on the identity of the anion used in the precursor solution, the resulting polymer film had different physical, optical and electronic properties. The effects of PSI loading on the electropolymerized polymer films were assessed and the resulting film properties and photoactive response were characterized. Certain types of composite PSI-PEDOT films generated cathodic photocurrent when in contact with an aqueous mediator which confirmed the retention of photoactivity of the polymer-entrapped PSI complex.

In summary, conductive polymer scaffolds and porous transparent metal oxide electrodes are great avenues for incorporating PSI into three-dimensional architectures. PSI multilayer films, specifically, are limited by the amount of contact they have with the electrode surface and/or the electrochemical mediator, which in turn limits the efficiency of electron transfer to and from the complex. Incorporation of PSI into conducting polymer frameworks allows for improved conductivity within the PSI−electrode interface. Improving the interfacial electron transfer

pathways within PSI multilayer films serves a crucial role in achieving higher efficiencies in PSI-based solar devices. In addition, incorporation of PSI into solid-state architectures results in improved performance stability over time through protecting PSI complex from the harmful effects of reactive oxygen species (ROS) and the corrosive effects of the mediator-electrolyte mixture.

Outlook:

Going forward with biohybrid solar energy conversion technologies, the long-term stability and performance efficiency are two main avenues that researchers need to focus more on. While the light to electrical energy conversion efficiency of these biohybrid devices has been increasing steadily over the past two decades, the long-term stability of the complex is still one of the biggest limiting factors in achieving a practical device. The stability of PSI complex is affected by the conditions of its immediate environment. The extraction procedure and the environment surrounding the complex during its use are all important considerations. Incorporating the entire thylakoid membrane into biohybrid devices rather than the extracted complex can be an avenue for improving stability.

Aerobic electrolytes are commonly used in PSI-based electrochemical systems due to the advantages of dissolved oxygen as a good electron acceptor from PSI. However, the presence of oxygen also allows the production of reactive oxygen species (ROS) and the consequential degradation of the PSI complex structure and function. *In vivo*, ROS are known to stimulate photoinhibition by damaging the active sites of the complex. Protective enzymes such as superoxide dismutase and ascorbate peroxidase are known to mitigate the effects of ROS by reacting with superoxide (O_2^-) and singlet oxygen ($^1O_2$). However, PSI-based electrodes do not have these protective enzymes which means long-term stability of the complex is compromised.

The use of anaerobic electrolytes with PSI serves as a great avenue for limiting ROS production and damage to the electrode stability. Immobilizing PSI onto the electrode surface through covalent attachment and entrapment has also been targeted as an avenue for maintaining stability at the PSI-electrode interface. These methods help to minimize desorption and dissolution of the complex into the electrolyte. Entrapment of PSI into conductive polymer scaffolds protects it from harmful species in solution or from flow in the bulk electrolyte. PSI-based solid-state solar cells are another avenue for maintaining structural and functional stability of the complex. Elimination of the liquid electrolyte protects the complex from soluble species, such as ROS, and immobilizes the complex between electrodes and protects it from the effects of bulk electrolyte flow. Liquid electrolytes can cause corrosion of metal components over time and the liquid flow can increase the desorption of the complex from the electrode surface.

Solar energy is considered to be the cleanest and most abundant renewable energy source available to humanity. Nature acts as an excellent model for efficient solar energy conversion: Photosynthetic complexes such as PSI provide inspiration for researchers on how to leverage the energy of the sun. Although PSI is highly evolved in its *in-vivo* role to sustain plant growth and proliferation, integrating it into biohybrid solar cells while maintaining its performance remains a challenge. The electrical currents and light conversion efficiencies obtained from these systems fall short of commercial viability. While PSI can independently function with high internal quantum efficiency, photosynthesis occurs through a series of biomolecular structures which act in tandem. Hence, when integrating PSI into biohybrid systems, finding the right electrode materials, electron accepting and donating mediators, composite materials, conjugates and conductive frameworks remains a top priority. In the past couple of decades, researchers from around the world have made incredible strides in incorporating PSI into biohybrid solar cells in

more efficient, practical and cost-effective ways. However, there are still major advancements and breakthroughs to be made. There is an important journey ahead before PSI-based solar energy conversion devices find their place in the marketplace.

REFERENCES

(1) Spinka, W. Attributes of Renewable Energy : From Nanopossibilities to Solar. **2010**, *IV*, 1–35.

(2) Fritts, C. E. On a New Form of Selenium Cell, and Some Electrical Discoveries Made by Its Use. *Am. J. Sci.* **1883**, *s3-26* (156), 465–472. https://doi.org/10.2475/ajs.s3-26.156.465.

(3) Janosik, S. M. The Silicon Solar Cells Turns 50. *NASPA J.* **2005**, *42* (4), 1. https://doi.org/10.1017/CBO9781107415324.004.

(4) Gronwald, M. Large Oil Shocks and the US Economy : Infrequent Incidents with Large Effects Author (s): Marc Gronwald Stable URL : Http://Www.Jstor.Org/Stable/41323148 . **2014**, *29* (1), 151–171.

(5) Järvi, S.; Gollan, P. J.; Aro, E. Understanding the Roles of the Thylakoid Lumen in Photosynthesis Regulation. **2013**, *4* (October), 1–14. https://doi.org/10.3389/fpls.2013.00434.

(6) Su, J.; Vayssieres, L. A Place in the Sun for Artificial Photosynthesis? *ACS Energy Lett.* **2016**, *1* (1), 121–135. https://doi.org/10.1021/acsenergylett.6b00059.

(7) Dismukes, G. C.; Klimov, V. V.; Baranov, S. V.; Kozlov, Y. N.; DasGupta, J.; Tyryshkin, A. The Origin of Atmospheric Oxygen on Earth: The Innovation of Oxygenic Photosynthesis. *Proc. Natl. Acad. Sci. U. S. A.* **2001**, *98* (5), 2170–2175. https://doi.org/10.1073/pnas.061514798.

(8) Musazade, E.; Voloshin, R.; Brady, N.; Mondal, J.; Atashova, S.; Zharmukhamedov, S. K.; Huseynova, I.; Ramakrishna, S.; Najafpour, M. M.; Shen, J. R.; Bruce, B. D.; Allakhverdiev, S. I. Biohybrid Solar Cells: Fundamentals, Progress, and Challenges. *J. Photochem. Photobiol. C Photochem. Rev.* **2018**, *35*, 134–156.

https://doi.org/10.1016/j.jphotochemrev.2018.04.001.

(9) Ciesielski, P. N.; Hijazi, F. M.; Scott, A. M.; Faulkner, C. J.; Beard, L.; Emmett, K.; Rosenthal, S. J.; Cliffel, D.; Kane Jennings, G. Photosystem I – Based Biohybrid Photoelectrochemical Cells. *Bioresour. Technol.* **2010**, *101* (9), 3047–3053. https://doi.org/https://doi.org/10.1016/j.biortech.2009.12.045.

(10) Stieger, K. R.; Feifel, S. C.; Lokstein, H.; Hejazi, M.; Zouni, A.; Lisdat, F. Biohybrid Architectures for Efficient Light-to-Current Conversion Based on Photosystem i within Scalable 3D Mesoporous Electrodes. *J. Mater. Chem. A* **2016**, *4* (43), 17009–17017. https://doi.org/10.1039/c6ta07141d.

(11) Szewczyk, S.; Giera, W.; Białek, R.; Burdziński, G.; Gibasiewicz, K. Acceleration of the Excitation Decay in Photosystem I Immobilized on Glass Surface. *Photosynth. Res.* **2018**, *136* (2), 171–181. https://doi.org/10.1007/s11120-017-0454-z.

(12) Teodor, A. H.; Bruce, B. D. Putting Photosystem I to Work: Truly Green Energy. *Trends Biotechnol.* **2020**, 1–14. https://doi.org/10.1016/j.tibtech.2020.04.004.

(13) Linn, A. I.; Mink, R.; Peteinatos, G. G.; Gerhards, R. In-Field Classification of Herbicide-Resistant Papaver Rhoeas and Stellaria Media Using an Imaging Sensor of the Maximum Quantum Efficiency of Photosystem II. *Weed Res.* **2019**, *59* (5), 357–366. https://doi.org/10.1111/wre.12374.

(14) Robinson, M. T.; Simons, C. E.; Cliffel, D. E.; Jennings, G. K. Photocatalytic Photosystem I/PEDOT Composite Films Prepared by Vapor-Phase Polymerization. *Nanoscale* **2017**, *9* (18), 6158–6166. https://doi.org/10.1039/c7nr01158j.

(15) Lípová, L.; Krchňák, P.; Komenda, J.; Ilík, P. Heat-Induced Disassembly and Degradation of Chlorophyll-Containing Protein Complexes in Vivo. *Biochim. Biophys. Acta* -

Bioenerg. **2010**, *1797* (1), 63–70. https://doi.org/10.1016/j.bbabio.2009.08.001.

(16) Dervishogullari, D.; Gizzie, E. A.; Jennings, G. K.; Cliffel, D. E. Polyviologen as Electron Transport Material in Photosystem I-Based Biophotovoltaic Cells. *Langmuir* **2018**, *34* (51), 15658–15664. https://doi.org/10.1021/acs.langmuir.8b02967.

(17) Friebe, V. M.; Frese, R. N. Photosynthetic Reaction Center-Based Biophotovoltaics. *Curr. Opin. Electrochem.* **2017**, *5* (1), 126–134. https://doi.org/https://doi.org/10.1016/j.coelec.2017.08.001.

(18) Nguyen, K.; Bruce, B. D. Growing Green Electricity: Progress and Strategies for Use of Photosystem i for Sustainable Photovoltaic Energy Conversion. *Biochim. Biophys. Acta - Bioenerg.* **2014**, *1837* (9), 1553–1566. https://doi.org/10.1016/j.bbabio.2013.12.013.

(19) Kiliszek, M.; Harputlu, E.; Szalkowski, M.; Kowalska, D.; Unlu, C. G.; Haniewicz, P.; Abram, M.; Wiwatowski, K.; Niedziółka-Jönsson, J.; MaćKowski, S.; Ocakoglu, K.; Kargul, J. Orientation of Photosystem i on Graphene through Cytochrome: C 553 Leads to Improvement in Photocurrent Generation. *J. Mater. Chem. A* **2018**, *6* (38), 18615–18626. https://doi.org/10.1039/c8ta02420k.

(20) Kaftan, D.; Brumfeld, V.; Nevo, R.; Scherz, A.; Reich, Z. From Chloroplasts to Photosystems: In Situ Scanning Force Microscopy on Intact Thylakoid Membranes. *EMBO J.* **2002**, *21* (22), 6146–6153. https://doi.org/10.1093/emboj/cdf624.

(21) Johnson, M. P.; Goral, T. K.; Duffy, C. D. P.; Brain, A. P. R.; Mullineaux, C. W.; Ruban, A. V. Photoprotective Energy Dissipation Involves the Reorganization of Photosystem II Light-Harvesting Complexes in the Grana Membranes of Spinach Chloroplasts. *Plant Cell* **2011**, *23* (4), 1468–1479. https://doi.org/10.1105/tpc.110.081646.

(22) Baba, K.; Itoh, S.; Hastings, G.; Hoshina, S. Photoinhibition of Photosystem I Electron

Transfer Activity in Isolated Photosystem I Preparations with Different Chlorophyll Contents. *Photosynth. Res.* **1996**, *47* (2), 121–130. https://doi.org/10.1007/BF00016175.

(23) Nelson, N.; Junge, W. Structure and Energy Transfer in Photosystems of Oxygenic Photosynthesis. *Annu. Rev. Biochem.* **2015**, *84* (1), 659–683. https://doi.org/10.1146/annurev-biochem-092914-041942.

(24) Shinkarev, V. P.; Vassiliev, I. R.; Golbeck, J. H. A Kinetic Assessment of the Sequence of Electron Transfer from FX to FA and Further to FB in Photosystem I: The Value of the Equilibrium Constant between FX and FA. *Biophys. J.* **2000**, *78* (1), 363–372. https://doi.org/https://doi.org/10.1016/S0006-3495(00)76599-4.

(25) Amunts, A.; Drory, O.; Nelson, N. The Structure of a Plant Photosystem I Supercomplex at 3.4 A Resolution. *Nature* **2007**, *447*, 58–63. https://doi.org/10.2210/PDB2O01/PDB.

(26) Cevik, E.; Carbas, B. B.; Senel, M.; Yildiz, H. B. Construction of Conducting Polymer/Cytochrome C/Thylakoid Membrane Based Photo-Bioelectrochemical Fuel Cells Generating High Photocurrent via Photosynthesis. *Biosens. Bioelectron.* **2018**, *113* (January), 25–31. https://doi.org/10.1016/j.bios.2018.04.055.

(27) LeBlanc, G.; Chen, G.; Gizzie, E. A.; Jennings, G. K.; Cliffel, D. E. Enhanced Photocurrents of Photosystem I Films on P-Doped Silicon. *Adv. Mater.* **2012**, *24* (44), 5959–5962. https://doi.org/10.1002/adma.201202794.

(28) Gunther, D.; LeBlanc, G.; Prasai, D.; Zhang, J. R.; Cliffel, D. E.; Bolotin, K. I.; Jennings, G. K. Photosystem I on Graphene as a Highly Transparent, Photoactive Electrode. *Langmuir* **2013**, *29* (13), 4177–4180. https://doi.org/10.1021/la305020c.

(29) Ciesielski, P. N.; Scott, A. M.; Faulkner, C. J.; Berron, B. J.; Cliffel, D. E.; Jennings, G. K. Functionalized Nanoporous Gold Leaf Electrode Films for the Immobilization of

Photosystem I. *ACS Nano* **2008**, *2* (12), 2465–2472. https://doi.org/10.1021/nn800389k.

(30) Ciobanu, M.; Kincaid, H. A.; Lo, V.; Dukes, A. D.; Kane Jennings, G.; Cliffel, D. E. Electrochemistry and Photoelectrochemistry of Photosystem I Adsorbed on Hydroxyl-Terminated Monolayers (the Paper for Energy Redox Potentials of P700 and Fb. *J. Electroanal. Chem.* **2007**, *599* (1), 72–78. https://doi.org/10.1016/j.jelechem.2006.09.019.

(31) Ivanov, A. G.; Velitchkova, M. Y.; Allakhverdiev, S. I.; Huner, N. P. A. Heat Stress-Induced Effects of Photosystem I: An Overview of Structural and Functional Responses. *Photosynth. Res.* **2017**, *133* (1–3), 17–30. https://doi.org/10.1007/s11120-017-0383-x.

(32) Ciesielski, P. N.; Faulkner, C. J.; Irwin, M. T.; Gregory, J. M.; Tolk, N. H.; Cliffel, D. E.; Jennings, G. K. Enhanced Photocurrent Production by Photosystem I Multilayer Assemblies. *Adv. Funct. Mater.* **2010**, *20* (23), 4048–4054. https://doi.org/10.1002/adfm.201001193.

(33) Mershin, A.; Matsumoto, K.; Kaiser, L.; Yu, D.; Vaughn, M.; Nazeeruddin, M. K.; Bruce, B. D.; Graetzel, M.; Zhang, S. Self-Assembled Photosystem-I Biophotovoltaics on Nanostructured TiO2 and ZnO. *Sci. Rep.* **2012**, *2*, 234.

(34) Wenzel, T.; Bombelli, P.; Howe, C. J.; Steiner, U. Generation from Photosynthetic Bio Fi Lms. *Nat. Commun.* No. 2018, 1–9. https://doi.org/10.1038/s41467-018-03320-x.

(35) Ciornii, D.; Riedel, M.; Stieger, K. R.; Feifel, S. C.; Hejazi, M.; Lokstein, H.; Zouni, A.; Lisdat, F. Bioelectronic Circuit on a 3D Electrode Architecture: Enzymatic Catalysis Interconnected with Photosystem I. *J. Am. Chem. Soc.* **2017**, *139* (46), 16478–16481. https://doi.org/10.1021/jacs.7b10161.

(36) Zhou, C.; Liu, Z.; Du, X.; Ringer, S. P. Electrodeposited PEDOT Films on ITO with a Flower-like Hierarchical Structure. *Synth. Met.* **2010**, *160* (15–16), 1636–1641.

https://doi.org/10.1016/j.synthmet.2010.05.033.

(37) Hamidi, H.; Hasan, K.; Emek, S. C.; Dilgin, Y.; Åkerlund, H. E.; Albertsson, P. Å.; Leech, D.; Gorton, L. Photocurrent Generation from Thylakoid Membranes on Osmium-Redox-Polymer-Modified Electrodes. *ChemSusChem* **2015**, *8* (6), 990–993. https://doi.org/10.1002/cssc.201403200.

(38) Gizzie, E. a.; Scott Niezgoda, J.; Robinson, M. T.; Harris, A. G.; Kane Jennings, G.; Rosenthal, S. J.; Cliffel, D. E. Photosystem I-Polyaniline/TiO $_2$ Solid-State Solar Cells: Simple Devices for Biohybrid Solar Energy Conversion. *Energy Environ. Sci.* **2015**, *8* (12), 3572–3576. https://doi.org/10.1039/C5EE03008K.

(39) Robinson, M. T.; Simons, C. E.; Cliffel, D. E.; Jennings, G. K. Photocatalytic Photosystem I/PEDOT Composite Films Prepared by Vapor-Phase Polymerization. *Nanoscale* **2017**, *9* (18), 6158–6166. https://doi.org/10.1039/c7nr01158j.

(40) Schröder, E.; Jönsson, T.; Poole, L. Hydroxyapatite Chromatography: Altering the Phosphate-Dependent Elution Profile of Protein as a Function of PH. *Anal. Biochem.* **2003**, *313* (1), 176–178. https://doi.org/10.1016/S0003-2697(02)00567-5.

(41) Yu, D.; Lan, J.; Khan, N. U.; Li, Q.; Xu, F.; Huang, G.; Xu, H.; Huang, F. The in Vitro Synergistic Denaturation Effect of Heat and Surfactant on Photosystem I Isolated from Arthrospira Platensis. *Photosynth. Res.* **2019**, *141* (2), 229–243. https://doi.org/10.1007/s11120-019-00623-y.

(42) Wang, X.; Huang, G.; Yu, D.; Ge, B.; Wang, J.; Xu, F.; Huang, F.; Xu, H.; Lu, J. R. Solubilization and Stabilization of Isolated Photosystem I Complex with Lipopeptide Detergents. *PLoS One* **2013**, *8* (9), 1–12. https://doi.org/10.1371/journal.pone.0076256.

(43) Cummings, L. J.; Snyder, M. A.; Brisack, K. Chapter 24 Protein Chromatography on

Hydroxyapatite Columns. *Methods Enzymol.* **2009**, *463* (C), 387–404. https://doi.org/10.1016/S0076-6879(09)63024-X.

(44) Gordiichuk, P. I.; Wetzelaer, G. J. A. H.; Rimmerman, D.; Gruszka, A.; De Vries, J. W.; Saller, M.; Gautier, D. A.; Catarci, S.; Pesce, D.; Richter, S.; Blom, P. W. M.; Herrmann, A. Solid-State Biophotovoltaic Cells Containing Photosystem I. *Adv. Mater.* **2014**, *26* (28), 4863–4869. https://doi.org/10.1002/adma.201401135.

(45) Faulkner, C. J.; Lees, S.; Ciesielski, P. N.; Cliffel, D. E.; Jennings, G. K. Rapid Assembly of Photosystem I Monolayers on Gold Electrodes. *Langmuir* **2008**, *24* (16), 8409–8412. https://doi.org/10.1021/la800670b.

(46) Papadopoulos, N.; Limniou, M.; Koklamanis, G.; Tsarouxas, A.; Roilidis, M.; Bigger, S. W. Spec UV-Vis: An Ultraviolet-Visible Spectrophotometer Simulation. *J. Chem. Educ.* **2001**, *78* (11), 1560. https://doi.org/10.1021/ed078p1560.

(47) Bard, A. J. *Electrochemical Methods : Fundamentals and Applications / Allen J. Bard, Larry R. Faulkner*; Wiley: New York, 1980.

(48) Sandford, C.; Edwards, M. A.; Klunder, K. J.; Hickey, D. P.; Li, M.; Barman, K.; Sigman, M. S.; White, H. S.; Minteer, S. D. A Synthetic Chemist's Guide to Electroanalytical Tools for Studying Reaction Mechanisms. *Chem. Sci.* **2019**, *10* (26), 6404–6422. https://doi.org/10.1039/c9sc01545k.

(49) Grassi, A. P.; Tremmel, A. J.; Koch, A. W.; El-Khozondar, H. J. On-Line Thickness Measurement for Two-Layer Systems on Polymer Electronic Devices. *Sensors (Switzerland)* **2013**, *13* (11), 15747–15757. https://doi.org/10.3390/s131115747.

(50) Kossivas, F.; Doumanidis, C.; Kyprianou, A. Thickness Measurement of Photoresist Thin Films Using Interferometry. *Interferom. - Res. Appl. Sci. Technol.* **2012**.

https://doi.org/10.5772/34983.

(51) Ashfold, M. N. R.; King, G. A.; Murdock, D.; Nix, M. G. D.; Oliver, T. A. A.; Sage, A. G. Πσ* Excited States in Molecular Photochemistry. *Phys. Chem. Chem. Phys.* **2010**, *12* (6), 1218–1238. https://doi.org/10.1039/b921706a.

(52) Sun, J.; Goldys, E. M. Linear Absorption and Molar Extinction Coefficients in Direct Semiconductor Quantum Dots. *J. Phys. Chem. C* **2008**, *112* (25), 9261–9266. https://doi.org/10.1021/jp800700m.

(53) Reeves, S. G.; Hall, D. O. [8] Higher Plant Chloroplasts and Grana: General Preparative Procedures (Excluding High Carbon Dioxide Fixation Ability Chloroplasts); San Pietro, A. B. T. M. in E., Ed.; Academic Press, 1980; Vol. 69, pp 85–94. https://doi.org/https://doi.org/10.1016/S0076-6879(80)69010-7.

(54) Goldstein, J. I.; Newbury, D. E.; Michael, J. R.; Ritchie, N. W. M.; Scott, J. H. J.; Joy, D. C. *Scanning Electron Microscopy and X-Ray Microanalysis*; Springer US, 2017.

(55) Wolfe, K. D.; Dervishogullari, D.; Stachurski, C. D.; Passantino, J. M.; Kane Jennings, G.; Cliffel, D. E. Photosystem I Multilayers within Porous Indium Tin Oxide Cathodes Enhance Mediated Electron Transfer. *ChemElectroChem* **2019**, 596–603. https://doi.org/10.1002/celc.201901628.

(56) Carmeli, I.; Frolov, L.; Carmeli, C.; Richter, S. Photovoltaic Activity of Photosystem I-Based Self-Assembled Monolayer. *J. Am. Chem. Soc.* **2007**, *129* (41), 12352–12353. https://doi.org/10.1021/ja073040c.

(57) Beam, J. C.; LeBlanc, G.; Gizzie, E. A.; Ivanov, B. L.; Needell, D. R.; Shearer, M. J.; Jennings, G. K.; Lukehart, C. M.; Cliffel, D. E. Construction of a Semiconductor-Biological Interface for Solar Energy Conversion: P-Doped Silicon/Photosystem I/Zinc

Oxide. *Langmuir* **2015**, *31* (36), 10002–10007. https://doi.org/10.1021/acs.langmuir.5b02334.

(58) Yuan, Y.; Shin, H.; Kang, C.; Kim, S. Wiring Microbial Biofilms to the Electrode by Osmium Redox Polymer for the Performance Enhancement of Microbial Fuel Cells. *Bioelectrochemistry* **2016**, *108*, 8–12. https://doi.org/https://doi.org/10.1016/j.bioelechem.2015.11.001.

(59) Nikandrov, V. V.; Borisova, Y. V.; Bocharov, E. A.; Usachev, M. A.; Nizova, G. V.; Nadtochenko, V. A.; Lukashev, E. P.; Trubitsin, B. V.; Tikhonov, A. N.; Kurashov, V. N.; Mamedov, M. D.; Semenov, A. Y. Photochemical Properties of Photosystem 1 Immobilized in a Mesoporous Semiconductor Matrix. *High Energy Chem.* **2012**, *46* (3), 200–205. https://doi.org/10.1134/S0018143912030095.

(60) Factor, A.; Heinsohn, G. E. Polyviologens - a Novel Class of Cationic Polyelectrolyte Redox Polymers. *J. Polym. Sci. Polym. Lett. Ed.* **1971**, *9*, 289–295.

(61) Liu, Futian ; Yu, Xianda ; Li, S. Preparation of Polyalkylviologen-Polyanion Complexes and Their Applications to the Debromination of Diphenyl Bromomethane under Heterophase Condition. *J. Polym. Sci. Part A Polym. Chem.* **1994**, *32*, 1043–1048.

(62) Sassoon, R. E.; Gershuni, S.; Rabani, J. Charge Separation in Photolnitlated Electron-Transfer Systems with Polyviologen Polyelectrolytes as Quenchers. *J. Phys. Chem.* **1985**, *89*, 1937–1945.

(63) Young Jo, M.; Eun Ha, Y.; Hyun Kim, J. Polyviologen Derivatives as an Interfacial Layer in Polymer Solar Cells. *Sol. Energy Mater. Sol. Cells* **2012**, *107*, 1–8. https://doi.org/10.1016/j.solmat.2012.08.003.

(64) Tagliazucchi, M.; Tice, D. B.; Sweeney, C. M.; Morris-Cohen, A. J.; Weiss, E. A. Ligand-

Controlled Rates of Photoinduced Electron Transfer in Hybrid CdSe. *ACS Nano* **2011**, *5* (12), 9907–9917.

(65) Tagliazucchi, M.; Amin, V. A.; Schneebeli, S. T.; Stoddart, J. F.; Weiss, E. A. High-Contrast Photopatterning of Photoluminescence within Quantum Dot Films through Degradation of a Charge-Transfer Quencher. *Adv. Mater.* **2012**, *24*, 3617–3621. https://doi.org/10.1002/adma.201201356.

(66) Kim, Y.; Lee, J. H.; Ha, H.; Im, S. W.; Nam, K. T. Material Science Lesson from the Biological Photosystem. *Nano Converg.* **2016**, *3* (1). https://doi.org/10.1186/s40580-016-0079-5.

(67) Yehezkeli, O.; Tel-vered, R.; Michaeli, D.; Nechushtai, R. Photosystem I (PSI)/ Photosystem II (PSII) -Based Photo-Bioelectrochemical Cells Revealing Directional Generation of Photocurrents. **2013**, No. 17, 2970–2978. https://doi.org/10.1002/smll.201300051.

(68) Dervishogullari, D.; Gizzie, E. A.; Jennings, G. K.; Cliffel, D. E. Polyviologen as Electron Transport Material in Photosystem I-Based Biophotovoltaic Cells. *Langmuir* **2018**. https://doi.org/10.1021/acs.langmuir.8b02967.

(69) Robinson, M. T.; Gizzie, E. A.; Mwambutsa, F.; Cliffel, D. E.; Jennings, G. K. Mediated Approaches to Photosystem I-Based Biophotovoltaics. *Curr. Opin. Electrochem.* **2017**, *5* (1), 211–217. https://doi.org/https://doi.org/10.1016/j.coelec.2017.09.015.

(70) Aissaoui, N.; Bergaoui, L.; Landoulsi, J.; Lambert, J.-F.; Boujday, S. Silane Layers on Silicon Surfaces: Mechanism of Interaction, Stability, and Influence on Protein Adsorption. *Langmuir* **2012**, *28* (1), 656–665. https://doi.org/10.1021/la2036778.

(71) Modestino, M. A.; Hashemi, S. M. H.; Haussener, S. Mass Transport Aspects of

Electrochemical Solar-Hydrogen Generation. *Energy Environ. Sci.* **2016**, *9* (5), 1533–1551. https://doi.org/10.1039/c5ee03698d.

(72) Myland, J. C.; Oldham, K. B. Cottrell's Equation Revisited: An Intuitive, but Unreliable, Novel Approach to the Tracking of Electrochemical Diffusion. *Electrochem. commun.* **2004**, *6* (4), 344–350. https://doi.org/10.1016/j.elecom.2004.01.013.

(73) Stachurski, C.; Click, S.; Wolfe, K.; Dervishogullari, D.; Rosenthal, S.; Jennings, G. K.; Cliffel, D. Optical and Electrochemical Tuning of Hydrothermally Synthesized Nitrogen-Doped Carbon Dots. *Nanoscale Adv.* **2020**, 3375–3383. https://doi.org/10.1039/D0NA00264J.

(74) Luo, H.; Dimitrov, S.; Daboczi, M.; Kim, J. S.; Guo, Q.; Fang, Y.; Stoeckel, M. A.; Samorì, P.; Fenwick, O.; Jorge Sobrido, A. B.; Wang, X.; Titirici, M. M. Nitrogen-Doped Carbon Dots/TiO2 Nanoparticle Composites for Photoelectrochemical Water Oxidation. *ACS Appl. Nano Mater.* **2020**, *3* (4), 3371–3381. https://doi.org/10.1021/acsanm.9b02412.

(75) Peng, H.; Li, Y.; Jiang, C.; Luo, C.; Qi, R.; Huang, R.; Duan, C. G.; Travas-Sejdic, J. Tuning the Properties of Luminescent Nitrogen-Doped Carbon Dots by Reaction Precursors. *Carbon N. Y.* **2016**, *100*, 386–394. https://doi.org/10.1016/j.carbon.2016.01.029.

(76) Friebe, V. M.; Millo, D.; Swainsbury, D. J. K.; Jones, M. R.; Frese, R. N. Cytochrome c Provides an Electron-Funneling Antenna for Efficient Photocurrent Generation in a Reaction Center Biophotocathode. *ACS Appl. Mater. Interfaces* **2017**, *9* (28), 23379–23388. https://doi.org/10.1021/acsami.7b03278.

(77) Nguyen, K.; Bruce, B. D. Growing Green Electricity: Progress and Strategies for Use of Photosystem I for Sustainable Photovoltaic Energy Conversion. *Biochim. Biophys. Acta* -

Bioenerg. **2014**, *1837* (9), 1553–1566. https://doi.org/https://doi.org/10.1016/j.bbabio.2013.12.013.

(78) Habermüller, K.; Mosbach, M.; Schuhmann, W. Electron-Transfer Mechanisms in Amperometric Biosensors. *Fresenius. J. Anal. Chem.* **2000**, *366* (6), 560–568. https://doi.org/10.1007/s002160051551.

(79) Zhao, F.; Ruff, A.; Rögner, M.; Schuhmann, W.; Conzuelo, F. Extended Operational Lifetime of a Photosystem-Based Bioelectrode. *J. Am. Chem. Soc.* **2019**, *141* (13), 5102–5106. https://doi.org/10.1021/jacs.8b13869.

(80) Wenzel, T.; Härtter, D.; Bombelli, P.; Howe, C. J.; Steiner, U. Porous Translucent Electrodes Enhance Current Generation from Photosynthetic Biofilms. *Nat. Commun.* **2018**, *9* (1), 1299. https://doi.org/10.1038/s41467-018-03320-x.

(81) Ciornii, D.; Kölsch, A.; Zouni, A.; Lisdat, F. A Precursor-Approach in Constructing 3D ITO Electrodes for the Improved Performance of Photosystem I-Cyt c Photobioelectrodes . *Nanoscale* **2019**, 15862–15870. https://doi.org/10.1039/c9nr04344f.

(82) Hippler, M.; Drepper, F.; Haehnel, W.; Rochaix, J. D. The N-Terminal Domain of PsaF: Precise Recognition Site for Binding and Fast Electron Transfer from Cytochrome C6 and Plastocyanin to Photosystem I of Chlamydomonas Reinhardtii. *Proc. Natl. Acad. Sci. U. S. A.* **1998**, *95* (13), 7339–7344. https://doi.org/10.1073/pnas.95.13.7339.

(83) Buesen, D.; Hoefer, T.; Zhang, H.; Plumeré, N. A Kinetic Model for Redox-Active Film Based Biophotoelectrodes. *Faraday Discuss.* **2019**, *215* (0), 39–53. https://doi.org/10.1039/C8FD00168E.

(84) Robinson, M. T.; Cliffel, D. E.; Jennings, G. K. An Electrochemical Reaction-Diffusion Model of the Photocatalytic Effect of Photosystem I Multilayer Films. *J. Phys. Chem. B*

2018, *122* (1), 117–125. https://doi.org/10.1021/acs.jpcb.7b10374.

(85) Terasaki, N.; Yamamoto, N.; Hiraga, T.; Sato, I.; Inoue, Y.; Yamada, S. Fabrication of Novel Photosystem I–Gold Nanoparticle Hybrids and Their Photocurrent Enhancement. *Thin Solid Films* **2006**, *499* (1), 153–156. https://doi.org/https://doi.org/10.1016/j.tsf.2005.07.050.

(86) Ciornii, D.; Riedel, M.; Stieger, K. R.; Feifel, S. C.; Hejazi, M.; Lokstein, H.; Zouni, A.; Lisdat, F. Bioelectronic Circuit on a 3D Electrode Architecture: Enzymatic Catalysis Interconnected with Photosystem I. *J. Am. Chem. Soc.* **2017**, *139* (46), 16478–16481. https://doi.org/10.1021/jacs.7b10161.

(87) Chen, G.; Leblanc, G.; Jennings, G.; Cliffel, D. Effect of Redox Mediator on the Photo-Induced Current of a Photosystem I Modified Electrode. *J. Electrochem. Soc.* **2013**, *160*, H315–H320. https://doi.org/10.1149/2.054306jes.

(88) Washko, P. W.; Welch, R. W.; Dhariwal, K. R.; Wang, Y.; Levine, M. Ascorbic Acid and Dehydroascorbic Acid Analyses in Biological Samples. *Anal. Biochem.* **1992**, *204* (1), 1–14. https://doi.org/https://doi.org/10.1016/0003-2697(92)90131-P.

(89) Trubitsin, B. V; Mamedov, M. D.; Semenov, A. Y.; Tikhonov, A. N. Interaction of Ascorbate with Photosystem I. *Photosynth. Res.* **2014**, *122* (2), 215–231. https://doi.org/10.1007/s11120-014-0023-7.

(90) Moir, J.; Soheilnia, N.; O'Brien, P.; Jelle, A.; Grozea, C. M.; Faulkner, D.; Helander, M. G.; Ozin, G. A. Enhanced Hematite Water Electrolysis Using a 3D Antimony-Doped Tin Oxide Electrode. *ACS Nano* **2013**, *7* (5), 4261–4274. https://doi.org/10.1021/nn400744d.

(91) Müller, V.; Rathousky, J.; Fattakhova-Rohlfing, D. Covalent Immobilization of Redox Protein within the Mesopores of Transparent Conducting Electrodes. *Electrochim. Acta*

2014, *116*, 1–8. https://doi.org/https://doi.org/10.1016/j.electacta.2013.10.136.

(92) Wenzel, T.; Härtter, D.; Bombelli, P.; Howe, C. J.; Steiner, U. Porous Translucent Electrodes Enhance Current Generation from Photosynthetic Biofilms. *Nat. Commun.* **2018**, *9* (1), 1299. https://doi.org/10.1038/s41467-018-03320-x.

(93) González, G. B.; Cohen, J. B.; Hwang, J. H.; Mason, T. O.; Hodges, J. P.; Jorgensen, J. D. Neutron Diffraction Study on the Defect Structure of Indium-Tin-Oxide. *J. Appl. Phys.* **2001**, *89* (5), 2550–2555. https://doi.org/10.1063/1.1341209.

(94) Thirumoorthi, M.; Thomas Joseph Prakash, J. Structure, Optical and Electrical Properties of Indium Tin Oxide Ultra Thin Films Prepared by Jet Nebulizer Spray Pyrolysis Technique. *J. Asian Ceram. Soc.* **2016**, *4* (1), 124–132. https://doi.org/10.1016/j.jascer.2016.01.001.

(95) Voiry, D.; Chhowalla, M.; Gogotsi, Y.; Kotov, N. A.; Li, Y.; Penner, R. M.; Schaak, R. E.; Weiss, P. S. Best Practices for Reporting Electrocatalytic Performance of Nanomaterials. *ACS Nano* **2018**, *12* (10), 9635–9638. https://doi.org/10.1021/acsnano.8b07700.

(96) Laisk, A.; Oja, V.; Eichelmann, H.; Dall'Osto, L. Action Spectra of Photosystems II and I and Quantum Yield of Photosynthesis in Leaves in State 1. *Biochim. Biophys. Acta - Bioenerg.* **2014**, *1837* (2), 315–325. https://doi.org/https://doi.org/10.1016/j.bbabio.2013.12.001.

(97) Evans, B. R.; O'Neill, H. M.; Hutchens, S. A.; Bruce, B. D.; Greenbaum, E. Enhanced Photocatalytic Hydrogen Evolution by Covalent Attachment of Plastocyanin to Photosystem I. *Nano Lett.* **2004**, *4* (10), 1815–1819. https://doi.org/10.1021/nl0493388.

(98) Wang, W.; Wang, Z.; Zhu, Q.; Han, G.; Ding, C.; Chen, J.; Shen, J. R.; Li, C. Direct

Electron Transfer from Photosystem II to Hematite in a Hybrid Photoelectrochemical Cell. *Chem. Commun.* **2015**, *51* (95), 16952–16955. https://doi.org/10.1039/c5cc06900a.

(99) Kothe, T.; Plumeré, N.; Badura, A.; Nowaczyk, M. M.; Guschin, D. A.; Rögner, M.; Schuhmann, W. Combination of a Photosystem 1-Based Photocathode and a Photosystem 2-Based Photoanode to a z-Scheme Mimic for Biophotovoltaic Applications. *Angew. Chemie - Int. Ed.* **2013**, *52* (52), 14233–14236. https://doi.org/10.1002/anie.201303671.

(100) Badura, A.; Guschin, D.; Kothe, T.; Kopczak, M. J.; Schuhmann, W.; Rögner, M. Photocurrent Generation by Photosystem 1 Integrated in Crosslinked Redox Hydrogels. *Energy Environ. Sci.* **2011**, *4* (7), 2435–2440. https://doi.org/10.1039/c1ee01126j.

(101) Gao, L.; Mao, X.; Zhu, H.; Xiao, W.; Gan, F.; Wang, D. Electropolymerization of PEDOT on CNTs Conductive Network Assembled at Water/Oil Interface. *Electrochim. Acta* **2014**, *136*, 97–104. https://doi.org/10.1016/j.electacta.2014.05.053.

(102) Zhou, C.; Liu, Z.; Yan, Y.; Du, X.; Mai, Y. W.; Ringer, S. Electro-Synthesis of Novel Nanostructured PEDOT Films and Their Application as Catalyst Support. *Nanoscale Res. Lett.* **2011**, *6*, 1–6. https://doi.org/10.1186/1556-276X-6-364.

(103) Poverenov, E.; Li, M.; Bitler, A.; Bendikov, M. Major Effect of Electropolymerization Solvent on Morphology and Electrochromic Properties of PEDOT Films. *Chem. Mater.* **2010**, *22* (13), 4019–4025. https://doi.org/10.1021/cm100561d.

(104) Koizumi, Y.; Shida, N.; Ohira, M.; Nishiyama, H.; Tomita, I.; Inagi, S. Electropolymerization on Wireless Electrodes towards Conducting Polymer Microfibre Networks. *Nat. Commun.* **2016**, *7*, 1–6. https://doi.org/10.1038/ncomms10404.

(105) Seki, Y.; Takahashi, M.; Takashiri, M. Effects of Different Electrolytes and Film Thicknesses on Structural and Thermoelectric Properties of Electropolymerized Poly(3,4-

Ethylenedioxythiophene) Films. *RSC Adv.* **2019**, *9* (28), 15957–15965. https://doi.org/10.1039/c9ra02310k.

(106) Joshi, D. R.; Adhikari, N. An Overview on Common Organic Solvents and Their Toxicity. *J. Pharm. Res. Int.* **2019**, *28* (3), 1–18. https://doi.org/10.9734/jpri/2019/v28i330203.

(107) Willhite, C. C. Developmental Toxicology of Acetonitrile in the Syrian Golden Hamster. *Teratology* **1983**, *27* (3), 313–325. https://doi.org/10.1002/tera.1420270305.

(108) Sun, H.; Zhang, L.; Dong, L.; Zhu, X.; Ming, S.; Zhang, Y.; Xing, H.; Duan, X.; Xu, J. Aqueous Electrosynthesis of an Electrochromic Material Based Water-Soluble EDOT-MeNH2 Hydrochloride. *Synth. Met.* **2016**, *211*, 147–154. https://doi.org/10.1016/j.synthmet.2015.11.019.

(109) Hu, X.; Wang, G.; Wong, T. K. S. Effect of Aqueous and Organic Solvent Ratio on the Electropolymerization of Bithiophene in the Mixed Solutions. *Synth. Met.* **1999**, *106* (3), 145–150. https://doi.org/10.1016/S0379-6779(99)00118-6.

(110) Schoetz, T.; Ponce de Leon, C.; Bund, A.; Ueda, M. Electro-Polymerisation and Characterisation of PEDOT in Lewis Basic, Neutral and Acidic EMImCl-AlCl3 Ionic Liquid. *Electrochim. Acta* **2018**, *263*, 176–183. https://doi.org/10.1016/j.electacta.2018.01.033.

(111) Horii, T.; Li, Y.; Mori, Y.; Okuzaki, H. Correlation between the Hierarchical Structure and Electrical Conductivity of PEDOT/PSS. *Polym. J.* **2015**, *47* (10), 695–699. https://doi.org/10.1038/pj.2015.48.

(112) Chou, T. R.; Chen, S. H.; Chiang, Y. Te; Chang, T. T.; Lin, C. W.; Chao, C. Y. Highly Conductive PEDOT:PSS Film by Doping p-Toluenesulfonic Acid and Post-Treatment with Dimethyl Sulfoxide for ITO-Free Polymer Dispersed Liquid Crystal Device. *Org.*

Electron. **2017**, *48*, 223–229. https://doi.org/10.1016/j.orgel.2017.05.052.

(113) Rudd, S.; Franco-Gonzalez, J. F.; Kumar Singh, S.; Ullah Khan, Z.; Crispin, X.; Andreasen, J. W.; Zozoulenko, I.; Evans, D. Charge Transport and Structure in Semimetallic Polymers. *J. Polym. Sci. Part B Polym. Phys.* **2018**, *56* (1), 97–104. https://doi.org/10.1002/polb.24530.